Förster Resonance Energy Transfer Mediated White-Light-Emitting Rhodamine Fluorophore Derivatives-Gamma Phase Gallium Oxide Nanostructures

by

Wan Hang Melanie Chiu

A thesis
presented to the University of Waterloo
in fulfillment of the
thesis requirement for the degree of
Master of Science
in
Chemistry

Waterloo, Ontario, Canada, 2012

Author's Declaration

I hereby declare that I am the sole author of this thesis. This is a true copy of the thesis, including any required final revisions, as accepted by my examiners.

I understand that my thesis may be made electronically available to the public.

Abstract

The global lighting source energy consumption accounts for about 22% of the total electricity generated. New high-efficiency solid-state light sources are needed to reduce the ever increasing demand for energy. Single-phased emitter-based composed of transparent conducting oxides (TCOs) nanocrystals and fluorescent dyes can potentially revolutionize the typical composition of phosphors, the processing technology founded on the binding of dye acceptors on the surface of nanocrystals, and the configurations of the light-emitting diodes (LEDs) and electroluminescence devices.

The hybrid white-light-emitting nanomaterial is based on the expanded spectral range of the donor-acceptor pair (DAP) emission originated from the γ-Ga_2O_3 nanocrystals *via* Förster resonance energy transfer (FRET) to the surface-anchored fluorescent dyes. The emission of the nanocrystals and the sensitized emission of the chromophore act in sync as an internal relaxation upon the excitation of the γ–Ga_2O_3 nanocrystals. It extends the lifetime of the secondary fluorescent dye chromophore and the internal relaxation within this hybrid complex act as a sign for a quasi single chromophore. The model system of white-light-emitting nanostructure system developed based on this technology is the γ–Ga_2O_3 nanocrystals-Rhodamine B lactone (RBL) hybrid complex. The sufficient energy transfer efficiency of 31.51% within this system allowed for the generation of white-light emission with the CIE coordinates of (0.3328, 0.3380) at 5483 K.

The relative electronic energy differences of the individual components within the hybrid systems based on theoretical computation suggested that the luminance of the nanocomposite comprised of RBL is dominantly mediated by FRET. The production of white-light-emitting diode (WLED) based on this technology have been demonstrated by solution deposition of the hybrid nanomaterials to the commercially available ultraviolet (UV) LED due to the versatility and chemical compatibility of the developed phosphors.

Acknowledgements

Praises and thanks to the God, the Almighty, for His showers of blessings and for sending the following wonderful people in my life; I consider myself one of the luckiest person in the world to have met everyone of you.

It is with immense gratitude that I acknowledge the support of my supervisor Professor Pavle Radovanovic for the opportunity to pursue this research project. Thank you for your guidance, patience, and pushing me to the limits on the projects. His constructive comments and insightful views have helped me progress in this project.

I would also like to thank the members of my advisory committee, Professor William Power and Professor Eric Prouzet for their contributions, support, and taking the time to be on my committee. I cannot fully express the gratitude for the assistance of Professor Jean Duhamel and his group members, especially Michael Fowler, for their valuable insight into time-resolved photoluminescence decay measurements and analyses.

I am indebted to many people who provided many advices and support in my academic career ever since I was an Undergraduate in the Chemistry Department. I wish to express my gratitude to Professor Sonny Lee who have inspired and first interested me in conducting research in the field of Chemistry as my Undergraduate research supervisor. He was a fabulous advisor: knowledgeable, perceptive and mindful of important aspects in research. His passion in science inspired me in pursuing graduate studies and searching for a career in the field of chemistry.

A special word of thanks to Lay Ling Tan who spared a lot of time out of her busy duties to give me great advises and a welcome diversity of perspective. I can't thank Dr. Dipesh Prema, Chan Lau, Siawash Ahmar and Wei Zhang for their exceptional friendship enough; I miss the time when we used to go out, drink and watch movies.

I could not have completed this research without the support of faculty, technicians and administrative staff, friends and fellow graduate students in the Chemistry Department. I thank Dr. Jake Fisher and Dr. Howard Siu for their care and help during my teaching assistance duties. I am very grateful for Ms. Catherine Van Esch for her continuous assistance in all administrative work. Ms. Jan Venne and Dr. Jalil Assoud are thanked for their assistance and expertise in NMR and solid-state chemistry respectively. To my students from CHEM 140L and 310L, thank you for letting me know that the effort I

put in for students is acknowledged and making the teaching assistance experience more enjoyable during and outside of the labs.

I am obliged to many of my colleagues who supported me during the early stage of my M. Sc. To Dr. Ian Hosein, thank you for being an encouraging listener. I thank Ting Wang for the lively discussions and constructive feedback and Manu Hegde for his assistance in the DAP modeling. I am grateful to Shokouh Farvid, Tahereh Saber and Vadim Chirmanov for their encouragement. Plenty of people kept me sane and happy in Waterloo, especially fellow chemists on the second and third floor of the Chemistry building.

To all my friends and family members who kept asking the question "When are you leaving Waterloo?" or the comment of "You're still here?", I can finally answer, "I am done". I apologize for missing many important events in the past years as I have been stuck in Waterloo. Thank you for being understanding and being there whenever I needed you guys. Special thanks to a few of my friends who were always there for me during the course of this study: Edward Chan, Vivien Wong, Matthew Wong, Lincoln Choi and Donald Siu. I express thanks to Luke and Leia the Cats for their close supervision of the writing of this thesis.

This thesis is dedicated to my beloved grandfather, who passed away during the preparation of this thesis, at the age of 88. I wish he could be present for my graduation, but I know he will be there in spirit. My words will fail to express my heartfelt thanks to my parents, Philip and Evangeline Chiu, and my siblings, Clement and Madeline Chiu, for their unconditional love and unceasing encouragement. I cannot repay the debt of gratitude I owe them for their emotional and financial support throughout my graduate studies. Finally, I would like to thank my boyfriend, Benny Chu, for his patience, love and support. For the past five years, you always been there for me, through happiness and, mostly, through sorrow, stress and frustration.

Wan Hang Melanie Chiu

Table of Contents

List of Figures

List of Tables

List of Abbreviations

A565	ATTO 565
A590	ATT0 590
Ac	Acetate
Acac	Acetylacetonate
AVS	Absolute Vacuum Scale
B3LYP	Becke, three-parameter, Lee-Yang-Parr
CB	Conduction Band
CCT	Colour Correlated Temperature
CFL	Compact Fluorescent Lamp
CIE	Commission Internationale de L'Eclairage
CIELUV	Commission Internationale de L'Eclairage 1976 (L^*, u^*, v^*)
CRI	Colour Rendering Index
CMF	Colour-Matching Function
D-A	Donor-Acceptor
DAP	Donor-Acceptor Pair
DFT	Density Functional Theory
FRET	Förster Resonance Energy Transfer
G09	Gaussian 09
HOMO	Highest Occupied Molecular Oribital
IRF	Instrument Response Function
ITO	Indium Tin Oxide
LED	Light-emitting Diode
lm	Lumen
LUMO	Lowest Unoccupied Molecular Orbital
NMR	Nuclear Magnetic Resonance
OA	Oleylamine
PCM	Polarizable Continuum Model
PEDOT:PSS	Poly(ethylenedioxythiophene:Polystyrene Sulphonate
PL	Photoluminescence

Poly-TPD	Poly(*N*,*N*'-bis(4-butylphenyl)-*N*,*N*'-bis(phenyl)benzidine)
QBS	Quinine Bisulfate
QD	Quantum Dot
Rh-B	Rhodamine B
RBL	Rhodamine B Lactone
Spiro-TPD	*N*,*N*'-bis(3-methylphenyl)-*N*,*N*'-diphenyl-9,9-spirobifluorene-2,7-diamine
TBPi	1,3,5-tris(*N*-phenylbenzimidizol-2-yl)benzene
TCO	Transparent Conducting Oxide
TCSPC	Time Correlated Single Photon Count
TD-DFT	Time Dependent - Density Functional Theory
TOPO	Tri-*n*-octylphosphine oxide
UV	Ultraviolet
UV-Vis	Ultraviolet-Visible
UV-Vis-NIR	Ultraviolet-Visible-Near Infrared
VB	Valence Band
WLED	White-light-emitting Diode
XRD	X-ray Diffraction
YAG	Yttrium Aluminum Garnet, $Y_3Al_5O_{12}$

Chapter 1

The Solid-State Lighting Revolution

1.1 Transition to Solid-State Lighting

1.1.1 Demand for Efficient Light Source

Lighting constitutes for more than 20 percent of the worldwide electricity consumption and is accountable for approximately 1900 megatonnes CO_2 global emission.[1] Conventional incandescent bulbs, which have been the main illumination source in homes and offices, are capable of converting only 1% to 5% of the electricity into usable light.[2] Compact fluorescent lamps (CFLs) held great potential for general lighting, however, they contain mercury that can be harmful to human health and the environment in the case of bulb breakage. Additionally, CFLs has a limited conversion efficacy that is unlikely to exceed 100 lumens per Watt (lm/W) and its generation of low quality chromaticity.[3] Many of these current lighting technologies are highly inefficient, hence the demand for rapid and widespread adoption of more efficient lighting have attracted extensive attention for decades (Figure 1.1).

Lighting systems are often characterized by their efficiency and lifetime. However, efficiency has not been the primary concern of most individual consumers or of the society as a whole. There were also low levels of attention about the global environmental issues impacted by generation of electricity. None of these conditions have been resolved; as a result, increasing the efficiency in converting electricity into usable light with acceptable colour balance has become an important issue.

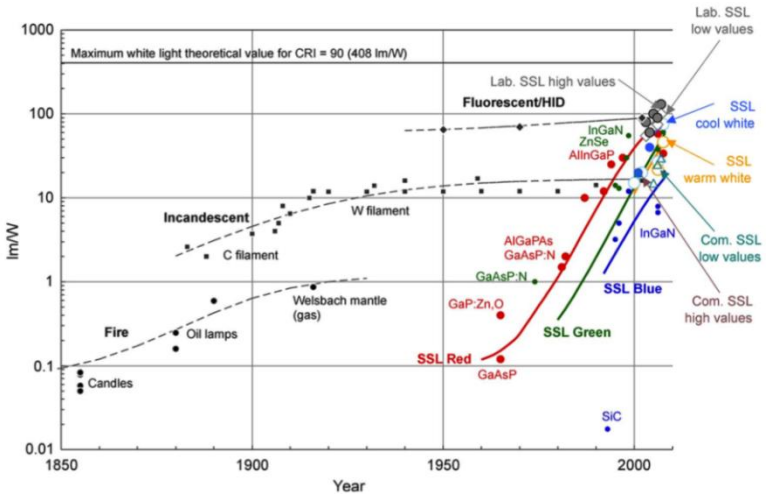

Figure 1.1. Efficacies of selected illumination sources developed from 1850 to 2006.[3,4]

Light-emitting diode (LED) shows great potential as a source of efficient, low-cost, extended lifetime and colour-balanced white-light.[5] In comparison with traditional illumination sources, LEDs consume 90% less energy and have a useful lifetime of up to 50,000 hours.[5] LEDs introduce the possibility of customable lighting fixture and has colour rendering index (CRI) up to 100, which permits the capability to render natural colours as perceived by the human eye.[6]

There are two factors that limit the production of high illumination LEDs. Green emission can be generated as the concentration of In in InGaN increase, however this is compromised by the decrease of quantum well efficiency.[6-9] Additionally, at high current density, the InGaN-based LEDs' efficiency decreases significantly. There are many proposed reasons for this behaviour: Auger recombination,[10] parasitic current due to defects,[11] electron overflow to the p-type semiconductor,[12] localized states carrier overflow,[13] and potential-barrier-induced piezoelectric polarization.[14] Due to these constraints, the fabrication of cost-effective LEDs is challenging as a consequences of the rigorous selection of the light-emitting phosphors.

1.1.2 Approaches in Developing Phosphors for White-Light-Emitting Diodes

Based on the physical principles, it is estimated that the luminous efficiency of white-light-emitting diodes (WLEDs) can reach 200 lm/W within a decade.[15] The general approach in improving the current light sources are either reducing the nonradiative electron-hole pair recombination in the p-n junction or designing new structures that increase the overall quantum efficiency.

WLEDs can be created by four main strategies: 1) Combining red, green and blue outputs in a single LED[16]; 2) Using an ultraviolet (UV) LED to stimulate red, green and blue phosphors, dealing with multiple phosphors, which may result in inhomogeneity[17]; 3) Coating UV or blue LEDs with doped phosphors[18,19]; 4) Depositing multiple layers of light-emitting organic molecules, which are less stable and involve expensive heavy metals such as platinum and iridium, on electroluminescence devices.[20,21]

In the case of using a combination of red, green and blue LEDs, the instability of colour temperature can occur as different colour LEDs degrade or due to the fluctuation in driving current. Different colour LEDs require variation in driving current, which complicates the production process. Additionally, the production of high power green LEDs remains a challenge.

Current commercially available WLEDs use blue (450-470 nm) GaN LEDs coated with $Y_3Al_5O_{12}$:Ce (YAG:Ce). The low energy emission of Ce^{3+} originates from the strong crystal field splitting

on the 5d level of the Ce^{3+}.[22] At low dopant concentrations, the temperature quenching problem is insignificant.[22] The emission and excitation spectra of YAG:Ce is tunable as the YAG:Ce lattice can accommodate different ions.[23] This design, however, suffers many weaknesses such as low CRI and poor stability of colour temperature due to the lack of a red component.[24] Most of the materials which act as dopants are rare earth elements which are becoming increasingly scarce and expensive.

Commercially available blue-LEDs comprised of indium gallium nitride (InGaN) contain quantum wells that facilitate electron-hole recombination.[7] Based on the amount of In, this can result in blue to green emission as the concentration of In increases. Due to the imperfect control of composition or the distribution of materials during the mass production of LEDs, each LED must be tested, resulting in the increase of manufactured cost. To fabricate white-light-emitting diode (WLED), one or several types of phosphor are deposited onto the LED. The inconsistency in the composition of various phosphors and the deposition process also require additional testing for their spectral output.[8]

1.1.3 Characterization of Light-Emitting-Diodes

Many strategies have been devised to characterize the ability of a light source to render colours. The most common methodology is the colour chromaticity space introduced by the Commission Internationale de L'Eclairage (CIE).[25] This is a two-dimensional space that describes the relative spectral power distribution that is used to represent the composition of any colour in terms of the three primaries (blue, green and red) as illustrated in Figure 1.2.

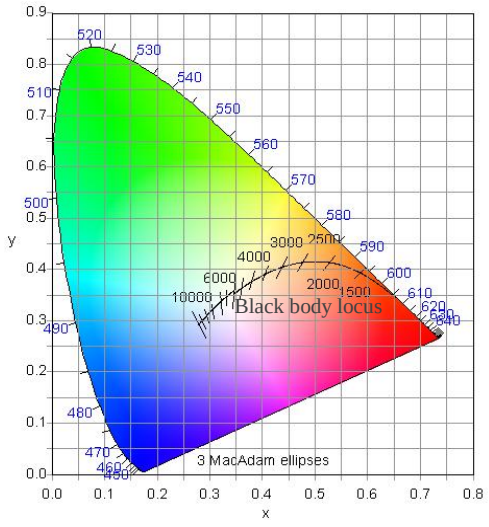

Figure 1.2. CIE 1931 2-degree CIE chromaticity diagram.[25]

The amount of each primary colour in the simulated patch, which was constructed by mixing the three primary colours, and the compensating illumination on the reference patch were processed to obtain the colour-matching functions, CMF (Figure 1.3).[26] The CMF dictates the tristimulus values that are necessary to compare to a hypothetical equal-energy spectrum, which has equal energy at all wavelengths, resulting in illuminant E that would be seen as white. The tristimulus values are given by

$$X = \int_0^\infty I(\lambda)T(\lambda)\bar{x}(\lambda)d\lambda \tag{1}$$

$$Y = \int_0^\infty I(\lambda)T(\lambda)\bar{y}(\lambda)d\lambda \tag{2}$$

$$Z = \int_0^\infty I(\lambda)T(\lambda)\bar{z}(\lambda)d\lambda \tag{3}$$

In the case of uniform illumination, *I(λ)* is equated to unity. The calculated tristimulus value can be represented graphically on the CIE Chromaticity Diagram, where the x,y-coordinates are calculated as

$$x = \frac{X}{X+Y+Z} \; and \; y = \frac{Y}{X+Y+Z} \tag{4}$$

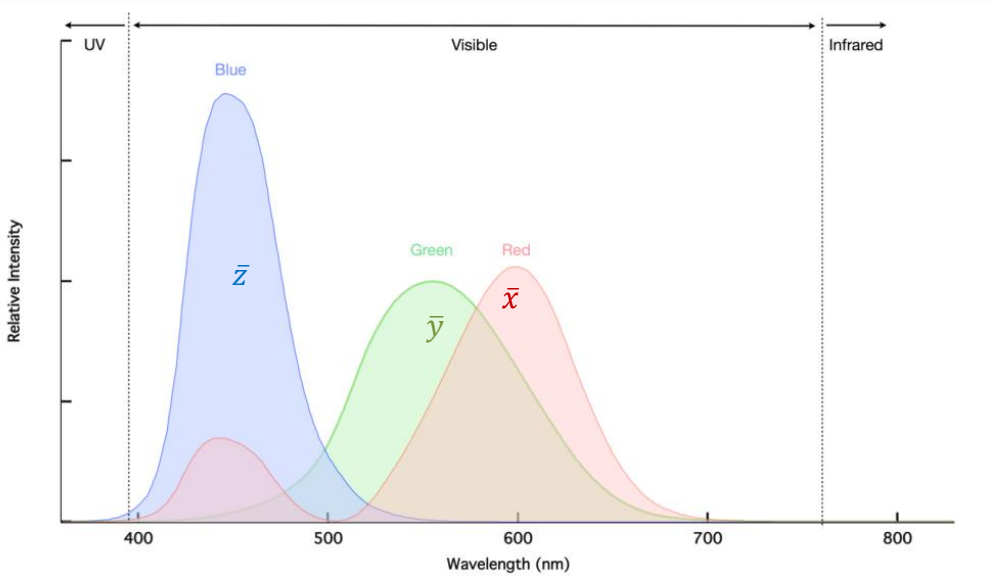

Figure 1.3. CIE 1931 2-degree field-of-view CMF.[25]

Correlated colour temperature (CCT) is the absolute temperature at which a blackbody radiator must be used to have a chromaticity equivalent to that of the light source.[27] Low colour temperature implies yellow-red illumination, while high colour temperature light source appears to be more blue. For general lighting purpose, the illuminations are designed to be in the proximity of the blackbody locus on the CIE chromaticity diagram (Figure 1.2). The concept of CCT should not be used if the chromaticity of the test source differs more than $\Delta C = \left[(u'_t - u'_P)^2 + \frac{4}{9}(v'_t - v'_P)^2\right]^{1/2} = 5 \times 10^{-2}$ from the Planckian radiator, where u'_t, v'_t address to the test source and u'_P, v'_P refer to the Planckian radiator.[25]

CRI is a unitless index range from 0 to 100 that is used to quantify the degree to which the observed colours of objects illuminated by the test source conform to those of the same objects illuminated by a reference source under the same environment.[27] A CRI rating of 100 suggests that all colour samples illuminated by the test source would appear to have the same colour as those illuminated by a reference light source.

Depending on the CCT of the test source, the reference illuminants of equal CCT are selected from a collection of blackbody radiators and phases of daylight. The chromaticity of the test source is required to transform to match that of the reference stimuli by means of a Von Kries adaptation.[28] Subsequently, the tristimulus values of various test colour samples (eight moderate chroma and six high chroma values) chosen from the Munsell Book of Colours can be determined for both the transformed test illuminant and the reference source. The difference between the transformed test source and the reference illuminant, denoted as ΔE_i, can be determined using the Commission Internationale de L'Eclairage 1976 (L^*, u^*, v^*) (CIELUV) colour space.[28] The two final steps are the transformation of the colour differences into colour-rendering indices (R_i) and the calculation of the general colour rendering index (R_a) given by

$$R_i = 100 - 4.6\Delta E_i \; and \; R_a = \frac{1}{8}\sum_{i=1}^{8} R_i \qquad (5)$$

Luminous efficacy is the figure of merit for illumination sources based on the ratio of the total luminous flux (lumens) to the power (Watt). For a monochromatic green light source, the lumen is defined as 1/683 W at a frequency of 540×10^{12} Hz. Theoretically, the maximum attainable value at a wavelength of 555 nm is 683 lm/W.[28] Depending on the application of the light source, the balance between luminous efficacy and CRI may be altered. A high CRI value requires proper spectral dispersion over the visible region, as a result, the luminous efficacy decrease significantly from 683 lm/W.[28]

1.2 Development in Inorganic-Organic Hybrid Phosphors for White-Light Emission

Generation of white-light-emitting phosphors involves simultaneous emission of the three primary colours or two complementary colours. The combination of the different colour phosphors require proper control for the energy/charge transfer processes that funnel excitons from the highest energy emitters (blue/green) to the lowest ones (orange/red). There are several approaches in designing white luminescent materials, as illustrated in Figure 1.4.

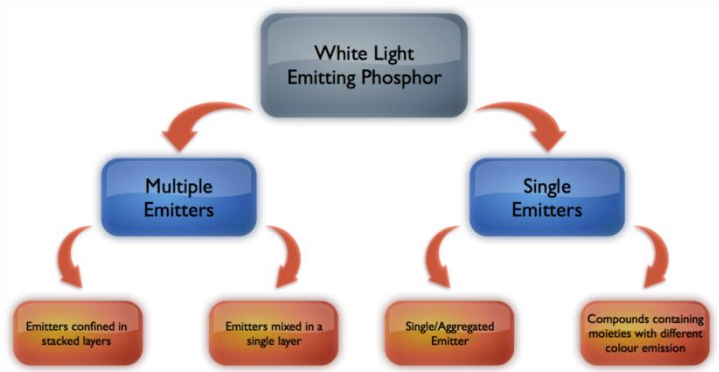

Figure 1.4. Approaches in designing organic / organometallic / nanostructure emitters.

Emitters confined in stacked layers enable good quality white-light emission and high efficiency, however, a major drawback is the cost of fabrication of such complex device and the voltage dependency. An example of this approach was two stacked layers composed of blue iridium(III)[bis(4,6-difluorophenyl)-pyridinato-*N*,$C^{2'}$]picolinate complex and orange complex of iridium with the ligand (9,9-diethyl-7-pyridinylfluoren-2-yl)-diphenylamine incorporated into 1,3-bis(9-carbazolyl)benzene and 4,4'-*N*,*N*'-di-carbzolebiphenyl.[29]

Multiple emitters mixed in a single layer can be achieved *via* evaporation techniques or solution processing which lower the cost for mass fabrication, yet result in low efficiency, low brightness phosphors and differential aging/changes in morphology that alters the stability of the white-light emission. A representative design is based on Förster Resonance Energy Transfer (FRET) between two conjugated polymers: blue-emitting poly(9,9-dioctylfluorene) and orange-red-emitting poly[2-methoxy-5-(2'-ethyl-hexyloxy)-1,4-phenylenevinylene].[30]

Single emitters can be expected to undergo circumventing phase separation and differential aging for multiple emitters; conversely, the syntheses of these materials are very complex and the efficiencies are generally lower than multilayer phosphors. Block copolymers composed of blue-emitting

polyfluorene and small segments of conjugated 1,8-naphthalimide as an orange-emitting component are one example of a single emitting phosphor that also acts as hole transporting moieties.[31]

1.3 Motivations and Scope of the Project

1.3.1 Surface Passivation of Organic Molecules on Nanocrystals

Nanostructures exhibit a wide range of relevant chemical and physical properties, which are of immense scientific and technology importance.[32] The ability to impart and control different functionally important properties by the meticulous engineering of the structure and composition of the nanomaterials is therefore critical. Despite of their attractive properties, some of these nanomaterials do not possess suitable surface properties for specific applications such as bio-imaging, sensors and photocatalysis.[33,34] As a result, surface modifications by the conjugation of suitable organic molecules to the surface became a general approach.[35]

Preparative possibilities that have been developed include grafting of a previously functionalized ligand on the nanocrystal surface, exchanging partial or all of the existing ligands on the nanocrystal surface, or grafting of a ligand on a nanocrystal with subsequent chemical reactions for further modifications. The strong interactions between the conjugated ligands and nanocrystals are often through the functional group(s) of the adsorbates, such as thiols and disulfides,[39-42] amine or ammonium ions,[43] carboxylic acids,[44-48] and phosphines.[49]

Surface modifications allow for protection of nanocrystals and introduce functionalities, such as: i) passivation of organic molecules can stabilize nanocrystals against agglomeration;[36] ii) allowance of compatibility in another phase;[37] iii) modification of nanofillers in organic polymers that prevent homogeneity between the two phases to improve mechanical properties of the composite;[38] iv) self-organization of nanocrystals,[35] and the passivation of surface traps for photoluminescence.[46]

Hybrid organic-inorganic colloidal nanoparticles can be designed to achieve specific properties that are absent in their pristine organic and inorganic components. The efficient coupling between the inorganic and organic moieties expedites the improvement of their optoelectronic properties as a single entity. Direct coupling between the organic and inorganic counterparts allows more efficient charge/energy transfer and correspondence between their energy levels.

Development of LEDs using metallic nanocrystals and organic molecules has been investigated. An example is the combination of size-tunable orange-red light-emitting quantum dots (QDs), CdSe nanocrystals, and blue-emitting poly(9,9'dihexylfluorene-2,7-divinylene-*m*-phenylene-vinylene-*stat*-*p*-phenylenevinylene) which led to the emission of white-light.[50] These nanostructures often use organic molecules as the donor in the energy transfer process, which result in short photoluminescence (PL) lifetime decay in the nanosecond range for the hybrid structure. In addition, segregation of the polymer coated nanocrystals and decay of properties over time have been observed for these systems. Despite the extensive research on QD-based LEDs, the possibility of expanding the research into transparent conducting oxide (TCO) nanocrystals has not yet been explored.

1.3.2 Transparent Conducting Oxide Nanocrystals

TCOs are a type of wide bandgap semiconductor and have many technologically-relevant properties – transparency, emission in the visible range, chemical inertness, hardness and conductivity. By manipulating the polymorphism and structural properties of these materials, their functional properties can be controlled.[51-53] Many of the TCO properties are defined by their structural defects.[54-56] There has been a significant breakthrough in tuning the properties of TCOs and controlling their electronic structures at the nanoscale as a result of the recent development in increasing the surface-to-volume ratio of the TCOs.

Gallium oxide (Ga_2O_3), having one of the largest bandgaps among TCOs ($E_g \approx 4.9$ eV)[57], will be the focus of this project. Owing to its thermal stability, monoclinic β-Ga_2O_3 has been the main focus out of the five different crystal structures (α, β, γ, δ and ε). It has been demonstrated that upon bandgap excitation, their photoluminescence result in UV and blue emissions. The origin of UV is the recombination of self-trapped exciton[58,59], while the long-lifetime blue emission is attributed to the recombination of an electron trapped on a donor and a hole on an acceptor.[60] The donor is an oxygen vacancy (V_O^x) and the acceptor could be either a gallium ion vacancy or a pair of charged vacancies ((V_O, V_{Ga})'). The high energy component has a half-life of approximately 30 ns, which is suggested to be the emission of β-Ga_2O_3, and the low energy component remains as phosphorescence. Although the preparation method was shown to be influential on the emission intensity of β-Ga_2O_3, a systematic manipulation of the luminescence energy has not been developed; conversely, size-tunable photoluminescence of colloidal metastable γ-Ga_2O_3 nanocrystals have been established (Figure 1.5).[54]

The photoluminescence of γ-Ga_2O_3 nanocrystals are governed by the donor-acceptor pair (DAP) recombination between the charge defect sites controlled by the binding energy of the localized donors and acceptors as well as the attractive Coulombic interactions between them.[61] Understanding these interactions allow for controllable tuning of the γ-Ga_2O_3 nanocrystals optical properties, making these nanocrystals an ideal component for the hybrid white-light-emitting nanostructures.

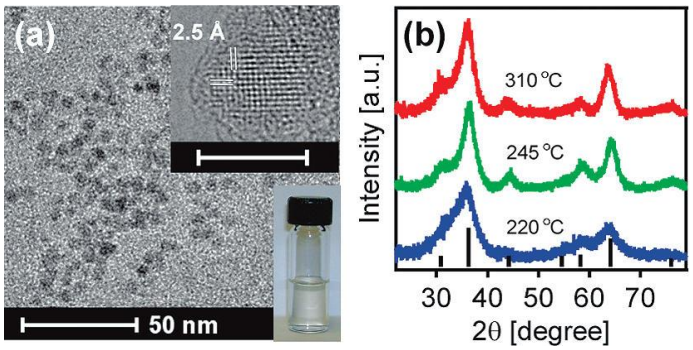

Figure 1.5. (a) TEM image of 6.0 ± 1.1 nm Ga_2O_3 nanocrystals. Insets: (Top) High resolution TEM image of a single nanocrystal with lattice spacings match (311) d-spacings of cubic Ga_2O_3. (Bottom) Photograph of colloidal Ga_2O_3. **(b)** X-ray diffraction (XRD) patterns of Ga_2O_3 synthesized at different temperatures.[54]

1.3.3 Introduction to TCO-Fluorophore Derivatives Nanostructures

Molecules or semiconductors generally have a narrow emission in the visible range, which makes the design of white-light emitters very challenging and increases the cost of fabrication. An original route to a white-light-emitting phosphor from a single entity based on blue-emitting TCO nanocrystals with a single type of dye chromophore bound to the surface of the nanocrystal was developed in this project.

These white-light-emitting systems can operate with high efficiency, reproducibly and at a low cost of production by the electronic structure design. The nanomaterial can be processed into devices from liquid form (i.e. colloidal form in solution) or in solid form (i.e. powder). The hybrid TCO-dye chromophore nanomaterial acts as a single illumination entity rather than a mixture, providing a homogeneous and uniform white-light emission. Different colour illumination can be achieved based on tuning the two components by changing the size of the nanocrystals, utilizing different dye chromophores, or altering the ratio between the two components. Various configuration and devices can employ the versatility and chemical compatibility of this material.

1.3.4 Förster Resonance Energy Transfer Mechanism

Understanding the interactions between the TCO nanocrystals and the secondary fluorescent dye chromophore allow for a wide range of tuning for the chromaticity of the hybrid nanomaterial's emission. The capability of controlling such interaction is an ideal feature for the hybrid white-light-emitting nanostructures based on the energy transfer from the nanocrystal donor to the fluorescent dye accepting species.

FRET is a distance-dependent Coulombic perturbation between the electronic excited states of a donor phosphor nanocrystal (γ-Ga_2O_3) on the acceptor molecule (fluorophore derivatives), which takes place electrodynamically through space, and is approximated as an electric, long-ranged dipole-dipole interaction. The excitation is transferred from donor to acceptor without emission of a photon.[62]

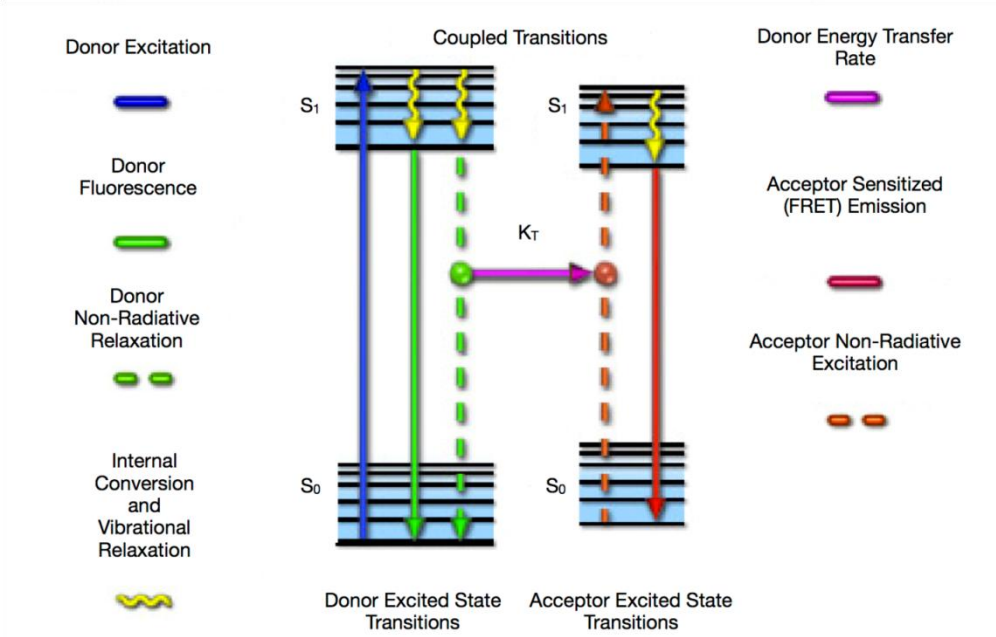

Figure 1.6. Förster resonance energy transfer Jablonski diagram.[62]

The theory implies several conditions that are required to be considered. The energy transfer normally takes place when the distance of donor and acceptor is 0.5 – 10 nm apart. Furthermore, the transition dipole moments of the donor and acceptor should not be oriented perpendicular to each other. It is required to have a spectral overlap between the emission spectrum of the donor and the absorption spectrum of the acceptor.

Chapter 2

Experimental Section: Preparation of the Hybrid Nanostructures

2.1 Materials

All commercial reagents and solvents were used as received without further purification. Gallium acetylacetonate, ($Ga(acac)_3$, 99.99%) was purchased from Strem Chemicals. Oleylamine (OA, 70%), tri-*n*-octylphosphine oxide (TOPO, 90%), Zinc acetate ($Zn(OAc)_2$, 99.99%), calcium hydroxide ($Ca(OH)_2$, ≥ 95%), [9-(2-carboxyphenyl)-6-diethylamino-3-xanthenylidene]-diethylammonium chloride, also known as Rhodamine B (Rh-B, 90%), 6-(2,5(6)-dicarboxyphenyl)-1,11-diethyl-2,3,4,8,9,10-hexahydro-1*H*-pyrano [3,2-*g*:5,6-*g*'] diquinolin-11-ium perchlorate (ATTO 565, ≥ 75%) and 6-(2,5(6)-dicarboxyphenyl)-1,11-diethyl-2,2,4,8,10,10-hexamethyl-2,10-dihydro-1*H*-pyrano [3,2-*g*:5,6-*g*'] diquinolin-11-ium perchlorate (ATTO 590, ≥ 90%) were purchased from Sigma-Aldrich Co. Lithium hydroxide (LiOH, ≥98%) was purchased from Fisher Scientific. Sodium hydroxide (NaOH, 97%) was purchased from Caledon Labs.

2.2 Syntheses and Sample Preparation

2.2.1 Synthesis of ɣ-Ga_2O_3 Nanocrystals

ɣ-Ga_2O_3 nanocrystals were synthesized according to published methods.[54] In a typical synthesis, colloidal ɣ-Ga_2O_3 nanocrystals were prepared by addition of 0.5 g of $Ga(acac)_3$ into 7.0 g of OA and the mixture was heated to 80°C for the purpose of dissolving $Ga(acac)_3$. The solution was then degassed and heated to 200-310°C at an average rate of 3°C per minute. The reaction mixture was refluxed at the desired temperature under anaerobic conditions for 1 hour. The nanocrystals were purified by iterations of ethanol washing and centrifugation at 3000 rpm. Subsequent surface modification with TOPO was done and the resulting nanocrystals were dispersed in hexane. The average size of these nanocrystals can be modulated by growth temperature from 3.3 ± 0.5 nm at 200°C to 6.0 ± 1.1 nm at 310°C.

2.2.2 Synthesis of ZnO Nanocrystals

ZnO nanocrystals that are rich in surface defects were prepared using a modified sol-gel method at room temperature. A solution of 0.549 g of $Zn(OAc)_2$ in 50 mL of absolute ethanol was refluxed to obtain a clear solution. The solution was then degassed and cooled to room temperature. Different molar

concentrations of different hydroxide salts in absolute ethanol solution were prepared by ultrasonic mixing. The hydrolysis process was initiated by the dropwise addition of the prepared basic solution into $Zn(OAc)_2$ solution at room temperature. The control of different particle sizes was achieved by addition of different molar concentrations of hydroxide solution. The size of the ZnO nanocrystals can be tuned to 2.53 nm, 3.72 nm, 5.31 nm, 6.84 nm and 12.16 nm using 30 mg of $Ca(OH)_2$, 3 mg of LiOH, 20 mg of LiOH, 10 mg of NaOH and 20 mg of NaOH, respectively. The solution was allowed to stir for 2 hours. The resulting ZnO nanocrystals were precipitated with ethyl acetate and centrifuged at 3000 rpm for 5 minutes. The obtained white powder was washed 3 times with ethyl acetate followed by centrifugation. The purified nanocrystals were dispersed in absolute ethanol.

2.2.3 Synthesis of 3',6'-bis(diethylamino)spiro[2-benzofuran-3,9'-xanthene]-1-one

3',6'-bis(diethylamino)spiro[2-benzofuran-3,9'-xanthene]-1-one, also known as Rhodamine B-lactone (RBL), was prepared following reported procedure.[63] Rh-B (3.1 mmol) was dissolved in 1 M aqueous NaOH solution (100 mL) and stirred for 2 hours. Subsequently, it was partitioned with ethyl acetate (75 mL). The organic layer was isolated and the aqueous layer was extracted twice with ethyl acetate. The combined organic layers were washed once with 1 M NaOH, followed by brine. The organic solution was dried with Na_2SO_4, filtered, dried under reduced pressure to yield RBL as a pink product (92%).

Spectral data similar to those reported (^{1}H, NMR, 300 MHz, acetone-d_6): δ(ppm) = 1.15 (t, $12H_1$, J = 7.0 Hz), 3.41 (q, $8H_2$, J = 7.0 Hz), 6.43 (dd, $2H_4$, J = 2.6, 8.7 Hz), 6.46 (d, $2H_3$, J = 2.3 Hz), 6.54 (d, $2H_5$, J = 8.7 Hz), 7.23 (br d, $1H_9$, J = 7.5 Hz), 7.68 (ddd, $1H_7$, J = 1.0, 7.4, 7.4 Hz), 7.76 (ddd, $1H_8$, J = 1.2, 7.4, 7.4 Hz), 7.96 (br d, $1H_6$, J = 7.4 Hz). See Appendix for NMR spectra.

2.2.4 Binding Luminescent Dye Chromophores to ɣ-Ga_2O_3 Nanocrystals

Given its broad, high stoke shift emission of the γ-Ga_2O_3 nanocrystals with the absorption of different secondary chromophores with different properties that emits in the orange-red region of the visible spectrum; this is the basis and the necessary component for the Förster resonance energy transfer mediated white-light-emitting phosphor. Meticulous design and understanding of the optical properties and electronic structures of the three chromophores led to the design of binding selected luminescent dye chromophores (RBL, A565 or A590) molecules to ɣ-Ga_2O_3 nanocrystal surfaces. The carboxylic group of the dye chromophores allows for effective binding to the Ga sites on the surface of the nanocrystals. This

process relies on the transport of dye chromophores dissolved in polar solvents to nanocrystals suspended in non-polar solvents, where the two solvents were not miscible and formed a bilayer solution. The solution was remained undisturbed for 8 hours. The non-polar layer was extracted followed by sonication for 30 minutes to ensure binding of the molecules on the surface of the nanocrystals.

2.3 Measurements and Data Analyses

2.3.1 Nuclear Magnetic Resonance Spectroscopy

^{1}H nuclear magnetic resonance (NMR) spectra were recorded on a Bruker AXS Avance spectrometer at 300 MHz and were referenced to the residual protiosolvent signal.

2.3.2 Absorption and Photoluminescence Spectroscopy

UV-Visible (UV-Vis) absorption measurements were performed on a Varian Cary 5000 ultraviolet-visible-near infrared (UV-Vis-NIR) spectrophotometer at room temperature and using quartz cells of 1 cm × 1 cm.

PL spectra were recorded with a Varian Cary Eclipse fluorescence spectrometer with bandwidth of 1 nm for both excitation and emission. Emission spectra were obtained between 200 nm and 700 nm. For the delayed PL measurements, the samples were excited in the maximum of the excitation band with a pulsed Xenon flash lamp and the emission intensity at each point of the spectra was recorded 0.1 ms after the excitation for 0.04 ms. All spectra were obtained with right angle geometry, at room temperature and using quartz cell of 1 cm × 1 cm.

2.3.3 Relative Quantum Yield Measurements

Relative quantum yields of the nanocrystals were calculated based on the following expression:

$$\Phi = \Phi_R \frac{I}{I_R} \frac{A_R}{A} \frac{n^2}{n_R^2} \qquad (6)$$

where Φ is the quantum yield, *I* is the area under the emission peak (wavelength scale), *A* is the absorbance at the excitation wavelength, and *n* is the refractive index of the sample solution. The subscript *R* denotes the analogous quantities of the reference substance. Quinine bisulfate (QBS) was used as the reference substance. The QBS solution was prepared in 1 N H_2SO_4 as previously reported.[64] Under these conditions, the quantum yield of QBS was determined to be 0.55.

2.3.4 Time-Resolved Fluorescence Spectroscopy

Fluorescence decays were acquired with an IBH Ltd. time-resolved fluorometer equipped with a IBH 563 nm NanoLED. All solutions in 1 cm × 1 cm quartz cuvettes were excited at 565 nm and the fluorescence from the samples was monitored at the maximum of the emission band to obtain the fluorescence decays with the right angle geometry. Time correlated single photon count (TCSPC) decays were acquired over 1024 channels with a 1 MHz repetition rate using times per channel of 0.059 ns/ch. The peak maximum was 20,000 counts for the instrument response function (IRF) and decay curves to ensure a high signal-to-noise ratio. A Ludox solution was used to obtain the IRF. The fluorescence decays fitting was accomplished by convoluting the function of interest to the IRF and optimizing the parameters of the function by the comparison of the convolution product with the experimental decays.

The fluorescence decays of the fluorophore derivatives and hybrid nanostructures were fitted independently with a sum of exponentials according to the following expression:

$$i(t) = \sum_{i=1}^{n} a_i \exp(-t/\tau_i) \qquad (7)$$

The fluorescence decays of the fluorophore dyes were fitted with a mono-exponential equation (n = 1) and the hybrid nanostructures were fitted with multi-exponential equation (n = 2,3 or 4).

2.3.5 Analysis of the Fluorescence Decay for γ-Ga_2O_3 Based on DAP model

Understanding the PL decay dynamics allow for quantitative analyses of the radiative recombination and the ability to control the optical properties of γ-Ga_2O_3 nanocrystal. The DAP model was extended to account for the finite volume within nanocrystals, which allows for different distribution of donor and acceptor sites within nanocrystals. Based on n-type behavior of Ga_2O_3, an assumption was made that the donor sites are in excess with one acceptor per nanocrystal. Furthermore, it was assumed that a single exciton was created in a nanocrystal, resulting in at most one DAP recombination per nanocrystal at one time. This assumption nullified the possibility of donor-donor interactions within a nanocrystal. In addition, the averaging of donor-acceptor (D-A) interactions is over all the nanocrystals in the solution, assuming that all interactions involving defects at different nanocrystals do not significantly impact the DAP recombination within individual nanocrystals.[65]

The recombination rate, *W*(r), for a DAP with the separation distance r is stated as

$$W(r) = W_{max}\ \exp\left(-\frac{2r}{R_d}\right) \tag{8}$$

where R_d is the Bohr radius of the donor and W_{max} is a constant that is found to be in good accordance with experimental data with a value of 10^7 s^{-1}. In the three-dimensional model, where a single acceptor was placed in the center of a sphere of a radius R_c and randomly located donor sites, the intensity of the emitted light at a given point in time, t, upon excitation can be expressed as

$$\langle Q(t)\rangle = \exp\left[4\pi n \int_0^{R_c} \{\exp[-W(r)t] - 1\} r^2 \mathrm{d}r\right] \tag{9}$$

where n is the density of donor per unit volume. The average decay rate is specified by

$$I(\mathrm{t}) = 3W_{max}\, N_D J_2\, \exp\left[3N_D\left(e^{-\tau e^{-2\rho}} - 1 - 2\rho\tau J_3\right)\right] \tag{10}$$

the variables r/R_c, $W_{max}\, t$ and R_c/R_d were reduced to x, τ and ρ respectively. $N_d = 4\pi R_c^3 n/3$ is the number of donors per nanocrystal and the auxiliary functions, J_2 and J_3, are defined as

$$J_i = \int_0^1 x^i e^{-2\rho x} e^{-\tau e^{-2\rho x}} dx \tag{11}$$

In the two-dimensional scenario, the average probability of an electron located on a donor site is given by

$$\langle Q(t)\rangle = \exp\left[4\pi R_c^2 n \int_0^{\pi/2} \{\exp[-W(2R_c cos\varphi)t] - 1\} \sin(2\varphi) d\varphi\right] \tag{12}$$

where n is the density of donors per unit area. Reducing the variables $cos\varphi = r/2R_c$, $W_{max}\, t$ and R_c/R_d to x, τ and ρ respectively, the PL decay rate can be expressed as

$$I(\mathrm{t}) = 2W_{max}\, N_D J_1\, \exp\left[N_D\left(e^{-\tau e^{-4\rho}} - 1 - 4\rho\tau J_2\right)\right] \tag{13}$$

the number of donors per nanocrystals is denoted as $N_d = 4\pi R_c^2 n$ and the auxiliary functions, J_1 and J_2, are formulated by

$$J_i = \int_0^1 x^i e^{-4\rho x} e^{-\tau e^{-4\rho x}} dx \tag{14}$$

2.3.6 Steady-State Analysis on Förster Resonance Energy Transfer

As a required criterion of Förster resonance energy transfer to occur, there must be an efficient amount of spectral overlap between the emission spectrum of the donor and the absorption spectrum of the acceptor. The spectral overlap integral can be shown as

$$J = \int F_d(\lambda)\varepsilon_A(\lambda)\lambda^4 d\lambda \tag{15}$$

where $\varepsilon_A(\bar{\nu})$ is the molar absorption coefficient of the acceptor (in units of cm^{-1} mol^{-1}), $F_D(\bar{\nu})$ is the fluorescence intensity of the measured fluorescence spectrum of the donor, and λ is wavelength. The rate constant of energy transfer can be represented by

$$k_t = \left(\frac{1}{\tau_D}\right)\left(\frac{R_0}{r_{DA}}\right)^6 \tag{16}$$

k_t is the rate constant for the transferring energy from an excited donor to an acceptor at a distance of r_{DA}. R_0 represents the distance r_{DA} where the rate of energy transfer is equal to the probability per unit time at which the excited donor would decay from excited state in absence of the acceptor. $1/\tau_D$ is the rate of deactivation from the excited state that includes all other pathways excluding the energy transfer to the acceptor. The value of R_0 for a pair of donor and acceptor is

$$R_0^6 = \frac{9000(ln10)\kappa^2 Q_D}{N_A 128\pi^5 n^4}\left[\int_0^\infty \varepsilon_A(\bar{\nu})F_D(\bar{\nu})\bar{\nu}^{-4}d\bar{\nu} \Big/ \int_0^\infty F_D(\bar{\nu})d\bar{\nu}\right] \tag{17}$$

where, $\bar{\nu}$ is wavenumber in cm^{-1} units, Q_D is the quantum yield of the donor, N_A is Avogadro's number, n is the index of refraction pertaining to the transfer, and κ is the angular function resulting from the inner product between the near unit vector of the electric field of the donor and the unit vector of the absorption dipole of the acceptor.[62]

The orientation factor, $\kappa^2 = (\cos\theta_{DA} - 3\cos\theta_D \cos\theta_A)^2$, where θ_{DA} is the angle between the transition dipole moments of the donor and acceptor, θ_D and θ_A are the angles between the donor and acceptor transition moments. Many fluorescent dyes have more than a single transition dipole, which can be excited at the same wavelengths, and since different transition dipoles of a fluorophore are usually not parallel to each other, this lead to an averaging of κ^2, where 2/3 is a good approximation.[62,64-69]

The energy transfer efficiency is expressed as

$$E = 1 - \frac{I_{DA}}{I_D} \quad (18)$$

In this formula, I_{DA} and I_D are the integrated intensity of the donor photoluminescence in the presence and absence of the acceptor, respectively. Employing the FRET model, the distance of the donor and acceptor, r_{DA}, can be estimated based on the efficiency of the quenching mechanism based on the following equation:

$$r_{DA}(\text{Å}) = R_0 \times \left(\frac{1-E}{E}\right)^{1/6} \quad (19)$$

2.3.7 Computational Methods

Density functional calculations were performed using the Gaussian 09 (G09) software package.[70] Becke, three-parameter, Lee-Yang-Parr (B3LYP) [71-73] functional was employed in combination with split valence double-zeta, doubly polarized 6-31G(d,p) [75,76] basis sets. Stationary points (minima) were verified by frequency calculations. Solvation effects were investigated via the polarizable continuum model (PCM) using the integral equation formalism,[78] which is the default self-consistent reaction field method in G09. Initial geometry optimizations were conducted on restricted singlet state, and all converged wave functions were tested for stability.[79,80] Unstable wave functions were reoptimized to stable unrestricted wave functions followed by further geometry optimization and wave function stability analyses. Default convergence criteria and parameters were used throughout. For time-dependent density functional theory (TD-DFT) calculations,[81] the 200 lowest energy singlet transitions, fully spanning the 200 – 700 nm spectral range. Electronic spectra were simulated with transitions represented by Gaussian functions with full-width at half-maximum values of 3000 cm^{-1} (GaussSum 2.2).[82] Qualitative assignments for the electronic transitions were obtained by visual inspection of orbital surfaces (GaussView).[83]

Chapter 3

Optical Properties of Fluorophore-Gallium Oxide Nanostructures

3.1 Tunable Luminescence of γ-Ga_2O_3 Nanocrystals

The basis of the γ-Ga_2O_3 nanomaterial is a strong broad-band long-lifetime emission of colloidal metastable γ-Ga_2O_3 nanocrystals size-tunable in blue-green region of the visible spectrum (Figure 3.1). The absorption spectra of the series of γ-Ga_2O_3 show negligible effect of quantum confinement because of the large effective mass of electrons ($m_e \approx 0.34\ m_0$) and tight exciton binding in the nanocrystal. The large Stokes shifts indicate a localized nature of recombining electrons and holes.

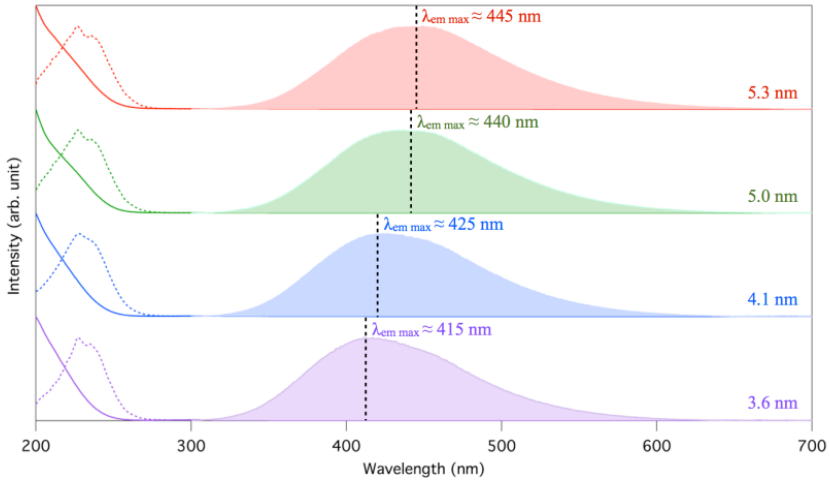

Figure 3.1. Absorption (solid lines), PL excitation (dashed lines), and PL emission (shaded region) spectra for a series of γ-Ga_2O_3 nanocrystals. The average nanocrystal sizes are shown in the figure.

Based on the dependency of the energy of the PL band maximum (DAP emission energy) on the nanocrystals size (Figure A.1), the average sizes of the nanocrystals used in this study were approximated. The quantum yields of these nanocrystals were determined to be 8%, 12%, 21% and 14% for 3.6 nm, 4.1 nm, 5.0 nm and 5.3 nm respectively.

The dominant blue emission has a long lifetime and can be distinguished by delayed PL measurements. The half-lives for 3.6, 4.1, 5.0 and 5.3 nm nanocrystals were determined to be 4.23 μs, 4.33 μs, 4.64 μs, and 5.07 μs, respectively. The decay dynamics is not driven by the transition probability of the recombination centers, hence the PL decay cannot be fitted by mono- or multi-exponential functions, but a modified DAP model (Figure 3.2).

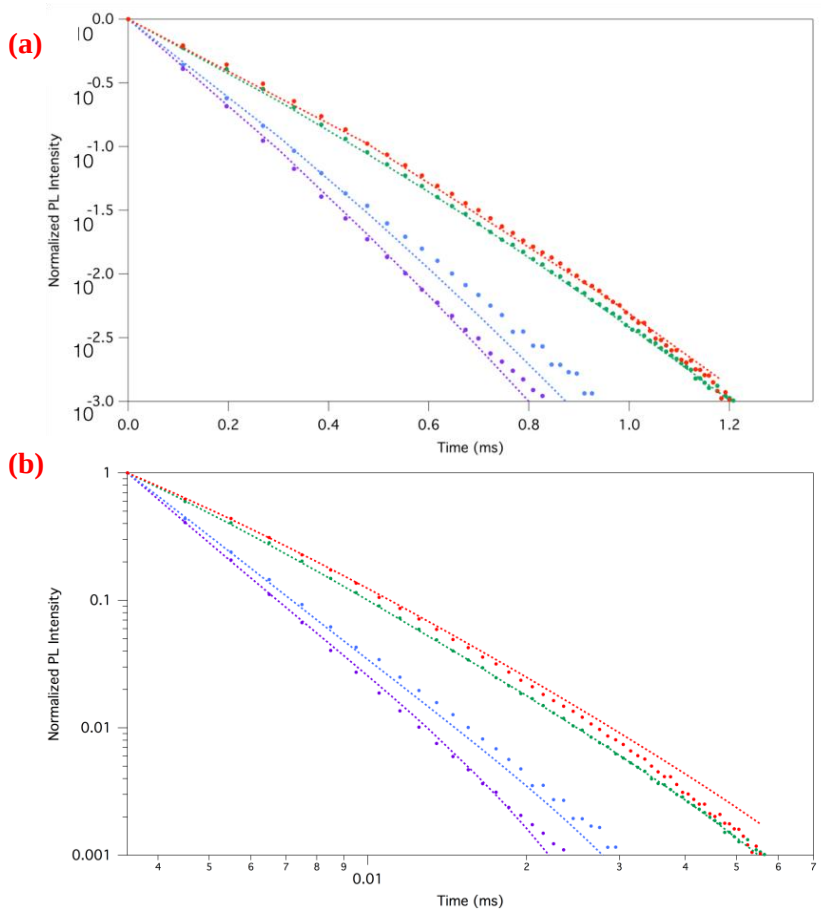

Figure 3.2. (a) The 2-dimensional model fit (solid lines) to the PL decay rate data (markers) normalized to unity at the initial time of measurement for different values of R_d: (purple, R_c = 1.8 nm) 1.5 nm, (blue, R_c = 2.05 nm) 1.6 nm, (green, 2.5 nm) 1.8 nm, (red, 2.65 nm) 1.8 nm. **(b)** The 3-dimensional model fit (solid lines) to the PL decay rate data (markers) normalized to unity at the initial time of measurement for sizes of nanocrystals: (purple, R_c = 1.8 nm), (blue, R_c = 2.05 nm), (green, 2.5 nm), (red, 2.65 nm).

The optimal fitting with the experimental data for nanocrystals of different sizes (R_c = 1.8, 2.05, 2.5, 2.65 nm are illustrated in Figure 3.2. The model is based on the random distribution in the nanocrystals and the surface segregation of the defects. The results of the modeling demonstrate that defects sites are mostly located in the vicinity of the nanocrystal surfaces and the density of the defects increases as the nanocrystal size decreases. Additionally, as the nanocrystal size decreases, the donor Bohr radius increases. This phenomenon indicates the inverse relationship between the nanocrystal size and the donor binding energy.

3.2 Fluorescent Dyes: Rhodamine Derivatives and Their Isomers

Attributable to the flexibility of the certain fluorescent dyes molecular structures, their solutions may contain a mixture of isomers. The equilibrium between the isomers depends on temperature and other environmental factors, leading to different electronic structures and optical properties based on the ratio of the isomers.

The fluorescent dyes of interest in this project were derivatives of Rhodamine: [9-(2-carboxyphenyl)-6-diethylamino-3-xanthenylidene]-diethylammonium chloride, also known as Rhodamine B (Rh-B, Figure 3.3 (a) inset); 6-(2,5(6)-dicarboxyphenyl)-1,11-diethyl-2,3,4,8,9,10-hexahydro-1*H*-pyrano [3,2-*g*:5,6-*g*'] diquinolin-11-ium perchlorate, called ATTO 565 (A565, Figure 3.5 (a) inset); and 6-(2,5(6)-dicarboxyphenyl)-1,11-diethyl-2,2,4,8,10,10-hexamethyl-2,10-dihydro-1*H*-pyrano [3,2-*g*:5,6-*g*'] diquinolin-11-ium perchlorate, identified as ATTO 590 (A590, Figure 3.5 (b) inset).

3.2.1 Rhodamine B: Tunable Optical Properties Based on Isomerization

For multicolour applications, different Rhodamine derivatives have been developed and extensively studied in terms of their electronic structures under various environmental conditions, providing a wide range of spectral properties. As a common condensation route used to synthesize xanthenes dyes, a carbonyl group in the 2' position can be introduced,[84] and the subsequent amide bond allows for further modifications.[84] It has been noted that secondary carboxyl or amides of Rhodamines rapidly cyclize to form nonfluorescent lactones or lactams.[63]

The Rhodamine dyes contain a free *o*-carboxyl group that can exist in several forms. The deprotonation is enhanced by dilution or addition of a small amount of base; the absorption maximum of deprotonated zwitterionic form blue shifts to a higher energy. In non-polar solvents such as hexane, the zwitterionic form is unstable and forms an intramolecular lactone, RBL (Figure 3.3 (b) inset), in a reversible fashion. In comparison with the quantum yield of Rh-B in water (31%), the RBL displays an almost insignificant quantum yield of less than 1% with a fluorescent emission centered at *ca.* 380 nm; this is followed by a long red tail that continues to *ca.* 600 nm (Figure 3.3). This is due to the interruption of the dye's π-electron system, which the RBL molecular form is considered to be non-fluorescent.

To complement the steady-state analysis, Rh-B in water and the γ-Ga_2O_3-RBL nanostructure in hexane were subjected to fluorescence lifetime analyses. Figure 3.4 shows the normalized time-resolved PL decays of the two samples, where Rh-B in water was fitted to a mono-exponential function, and the γ-

Ga_2O_3-RBL assemblies in hexane was fitted to a bi-exponential function. The corresponding average lifetime (τ_{avg}) and individual lifetime components ($\tau_{1,2}$) along with their fractional amplitudes are presented in Table 3.1. The dynamic of the excited-state for the RBL is significantly different than the protonated form of Rh-B in water, indicating that the binding affinity and the electronic structure of the molecules undergo considerable changes.

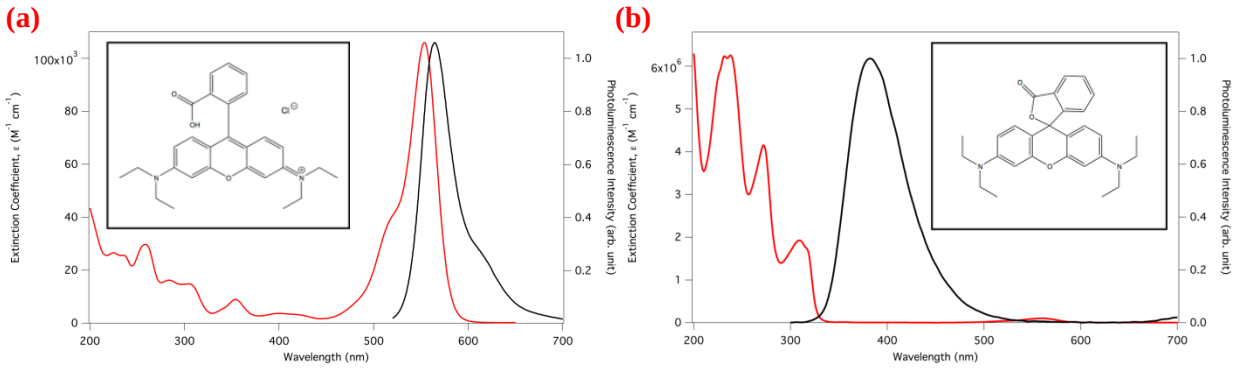

Figure 3.3. (a) Absorption (red) and emission (black) spectra of Rh-B in H_2O; the molecular structure of Rh-B is shown in the inset. **(b)** Absorption (red) and emission (black) spectra of RBL in hexane. The emission spectrum is multiplied by a factor of 30. The molecular structure of RBL is shown in the inset.

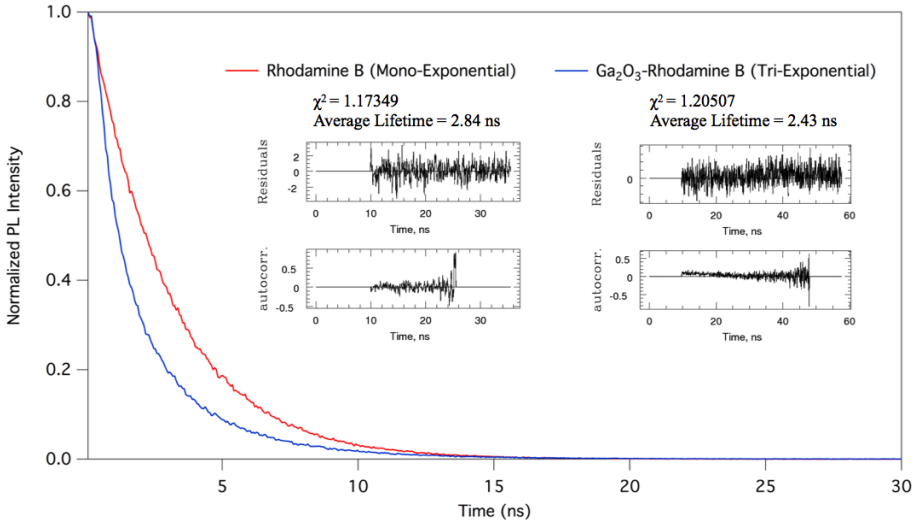

Figure 3.4. Normalized time-resolved PL decays of Rh-B in H_2O (red) and RBL bound to the surface of γ-Ga_2O_3 nanocrystals in hexane (blue) with λ_{ex} = 565 nm and λ_{em} = 580 nm.

Table 3.1. Lifetimes of Rh-B and RBL fitted with mono- and tri-exponential respectively.

	Lifetime (ns)[a]			
	τ_{avg}	τ_1	τ_2	τ_3
Rh-B in H_2O	2.84	2.84 (93.37%)	0.00 (0.00%)	0.00 (0.00%)
γ-Ga_2O_3-RBL in hexane	2.43	3.78 (10.14%)	1.72 (29.52%)	0.47 (60.34%)

[a] Amplitude weighted as described and fitted with either mono- or multi-exponential function. The lifetime component(s) are given along with their fractional intensity.

3.2.2 ATTO Dyes: Environmental Factors-Independent, Optically Active Rhodamine Derivatives

ATTO dyes are derivatives of coumarin, Rhodamine, carbopyronin and oxazine and possess high rigidity molecular structures that form equilibria with various isomers. To avoid the cyclization pathway, an addition of carboxyl groups at the 5' or 6' position of the phenyl ring can increase the rigidity of the molecular structure of A565 and A590. Consequently, both static and dynamic optical properties of these Rhodamine derivatives become nearly independent of the solvents and temperature. The optical features of the high fluorescent yield (90%), high thermal and photostability A565 and A590 dyes in water are illustrated in Figure 3.5.

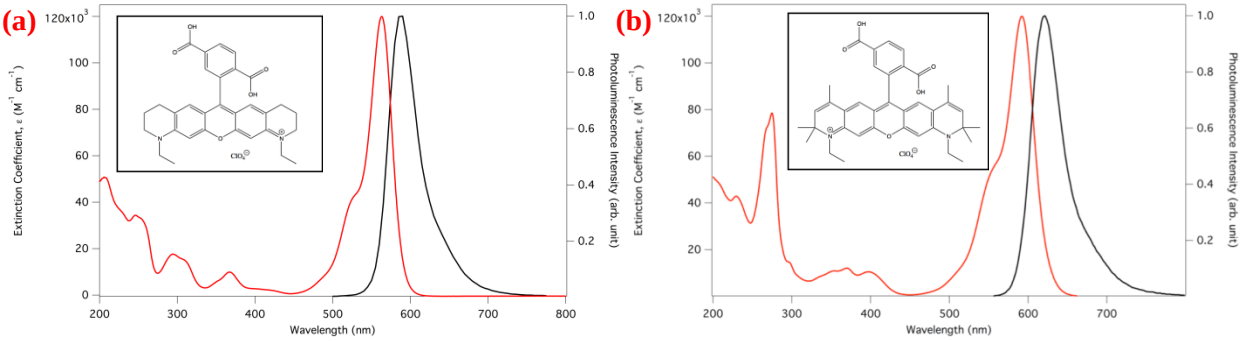

Figure 3.5. (a) Absorption (red) and emission (black) spectra of A565 in H_2O; the molecular structure of A565 is shown in the inset. **(b)** Absorption (red) and emission (black) spectra of A590 in H_2O; the molecular structure of A590 is shown in the inset.

A565 and A590 were used as proof-of-concept to demonstrate the feasibility, effectiveness, and the generality of FRET activated emission of the fluorescent dyes. Due to the insensitivity of A565 and A590 to environmental factors, there is insignificant difference of the absorption and emission spectra of the

two fluorescent dyes (Figure 3.6). When exposed to high energy excitation (*ca.* 250 nm), the orange/red emission is observable due to direct excitation with quantum yield of *ca.* 30%.

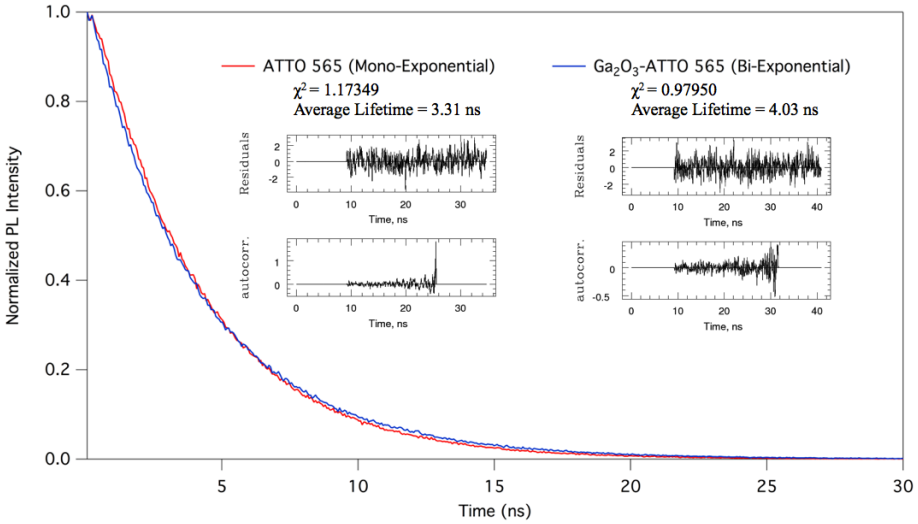

Figure 3.6. Normalized time-resolved PL decays of A565 in H_2O (red) and A565 bound to the surface of γ-Ga_2O_3 nanocrystals (blue) with λ_{ex} = 565 nm and λ_{em} = 590 nm.

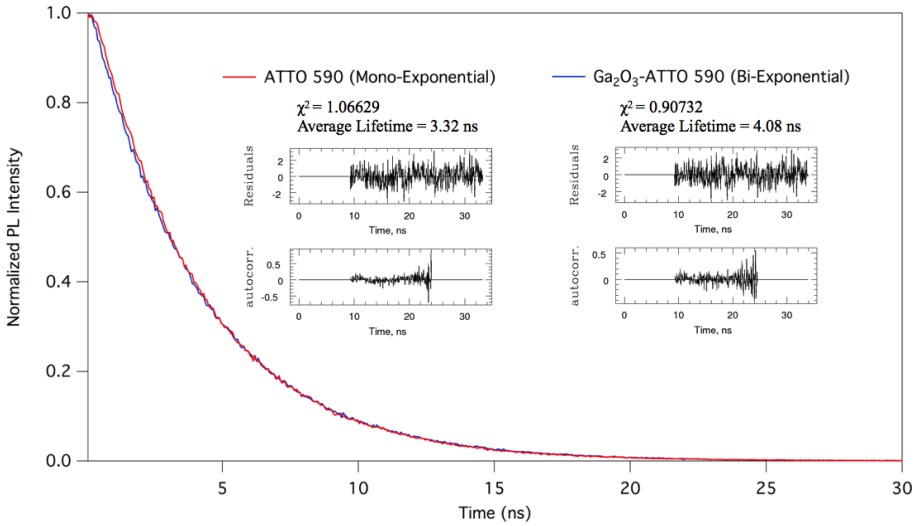

Figure 3.7. Normalized time-resolved PL decays of A590 in H_2O (red) and A590 bound to the surface of γ-Ga_2O_3 nanocrystals (blue) with λ_{ex} = 565 nm and λ_{em} = 620 nm.

Fluorescence lifetime analyses conducted on the free ATTO dyes and those bound on the surface of the γ-Ga_2O_3 nanocrystals demonstrate negligible differences (Figure 3.6 and Figure 3.7) as a confirmation

that the optical properties and the electronic structures of the ATTO dyes are not influenced by environmental factors. The average lifetime and the various lifetime components of the excited states of A565 and A590 are summarized in Table 3.2.

Table 3.2. Lifetimes of A565 and A590, which were fitted with mono- and bi-exponential for the sample in H_2O and hexane respectively.

	Lifetime (ns)[a]		
	τ_{avg}	τ_1	τ_2
A565 in H_2O	3.39	3.95 (85.59%)	0.00 (0.00%)
γ-Ga_2O_3-A565 in hexane	4.03	4.60 (71.20%)	2.63 (28.80%)
A590 in H_2O	3.32	3.97 (83.48%)	0.00 (0.00%)
γ-Ga_2O_3-A590 in hexane	3.44	4.27 (56.80%)	3.568 (28.50%)

[a] Amplitude weighted as described and fitted with either mono- or multi-exponential function. The lifetime component(s) are given along with their fractional intensity.

3.3 γ-Ga_2O_3-Fluorophores Nanostructures

3.3.1 Steady-State Photoluminescence Analyses

The white-light-emitting phosphor is based on the broad emission and tunability of the γ-Ga_2O_3 nanocrystals and manipulation of the interactions between the nanocrystals and the secondary chromophore that are passivated on the surface of the nanocrystals. The genesis of this innovation is based on the sufficiently broad donor-acceptor pair recombination emission of the γ-Ga_2O_3 nanocrystals. The emission of the nanocrystals is centered in the blue-green spectral region that requires only the addition of the relatively narrow emission of a secondary chromophore, whether it is in the molecular form or solid state form. This will allow the electronic coupling, either by electron or energy transfer from the donor to the accepting species. This approach allows for a path of a single white-light-emitting phosphor.

Individuate strategies in tailoring the performances of the white-light-emitting materials is demonstrated by modulating the emission properties of hybrid nanocomposite materials, *via* tuning the properties of the donor (size of the nanocrystals and the defect concentration) and the interaction processes between the dye chromophore and nanocrystal phosphor. Figure 3.8 shows the normalized

absorption and emission spectra of the Rhodamine derivatives (RBL, A565, A590) and four γ-Ga_2O_3 (R_c = 1.8, 2.05, 2.5, 2.65 nm) utilized in this study. This methodology provides new opportunities in the investigation of fluorescence with radiative decay engineering, which involves the modification of the emission of nanocrystal phosphors or dye chromophores by increasing or decreasing their radiative decay rates.

The wide Lorentzian-shaped DAP emission result in a moderate spectral overlap with the fluorescent dyes' Gaussian-shaped absorption profiles: The spectral overlap integrals for RBL with γ-Ga_2O_3 with R_c = 1.8, 2.05, 2.5, 2.65 nm are 5.81, 7.04, 8.43 and 9.33 × 10^{14} M^{-1} cm^3. A565, with similar emission profile as RBL, yields spectral overlap integrals of 5.46, 6.74, 8.19 and 9.16 with the series of γ-Ga_2O_3 nanocrystals. In comparison with RBL and A565, a significantly red-shifted emission profile of A590 resulted in lower overlap integrals: 5.26, 6.25, 7.39, and 8.37 × 10^{14} M^{-1} cm^3.

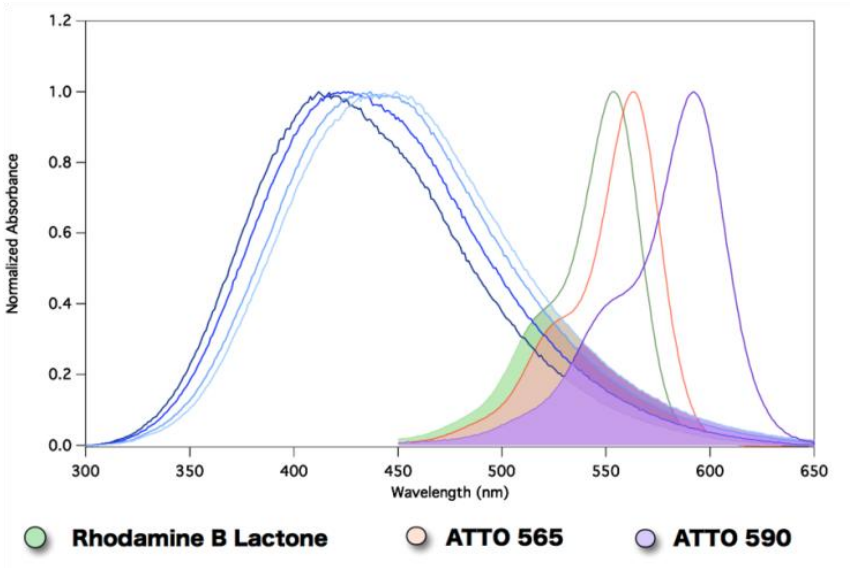

Figure 3.8. Spectral overlap of selected absorption and emission spectra of the four different sizes of γ-Ga_2O_3 (3.6, 4.1, 5.0 and 5.3 nm) and various Rhodamine derivatives (RBL, A565 and A590).

The γ-Ga_2O_3 nanocrystals were assembled with increasing ratios of RBL molecules (Figure 3.9) and subjected to detailed steady-state and lifetime decay spectroscopic analyses. All samples display a similar strong quenching response to the increased presence of the RBL molecules. The quenching data were then subjected to analyses based on a Förster framework that describes the γ-Ga_2O_3 nanocrystals donor resonance energy transfer with *n* acceptors placed around the nanocrystal surface.

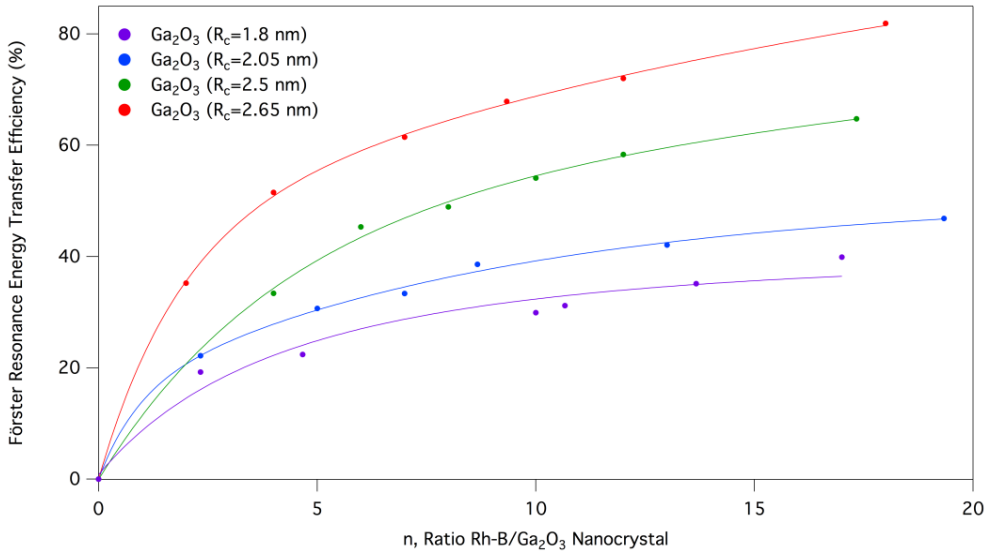

Figure 3.9. Plot of FRET efficiency as a function of the ratio RBL molecules/Ga_2O_3 for different sizes of nanocrystals. The Brillouin function fits are shown as a guide to the eye.

By increasing the amount of the dye-acceptor on the surface of the nanocrystals, the probability of transferring energy from the nanocrystal phosphor-donor to dye-acceptor is higher than emitting energy in the form of DAP recombination-based blue emission of γ-Ga_2O_3. As the ratio of the dye-acceptor to nanocrystal phosphor-donor increase, the packing of acceptor on the surface of the donor nanocrystals increase, the emission of the nanocrystals will be quenched and enhances the emission of the dye-acceptor as the probability of FRET increase.

The quenching and the enhancement in the PL emission of γ-Ga_2O_3 and fluorescent dyes were originated from the interactions between the two components of the hybrid nanostructures. As the Rhodamine derivatives remain non-fluorescent under non-polar solvent conditions, the enhancement in the PL emission of the fluorescent dyes were due to the energy transfer mechanism instead of direct excitation of the π-conjugated aromatic ring system of the dyes.

As the size of γ-Ga_2O_3 nanocrystals increase, the spectral overlap integral between the nanocrystals emission spectra and fluorescent dyes absorption spectra was enhanced. This resulted in the amplified quenching of the blue DAP recombination emission of γ-Ga_2O_3 nanocrystals, where the quenched energy was electrodynamically transferred to the fluorescent dyes acceptors (Figure 3.10).

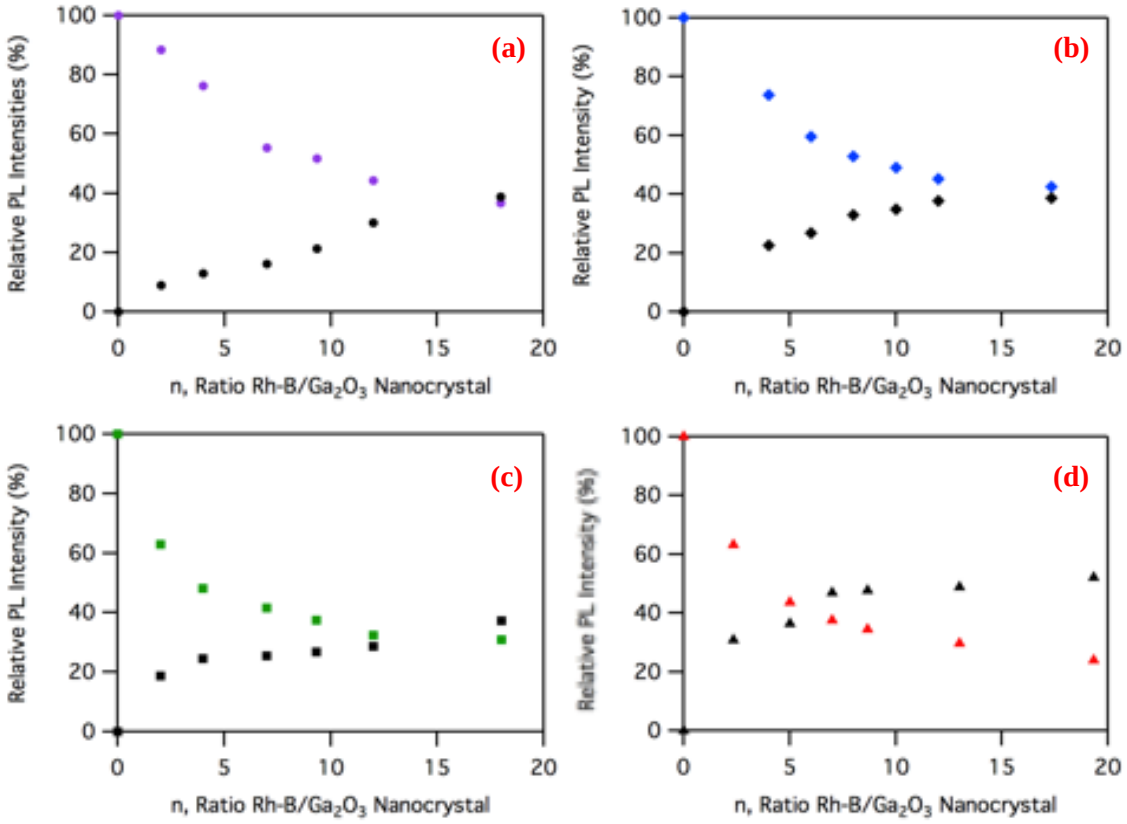

Figure 3.10. Relative PL intensities of the RBL (black) and nanocrystals with size of **(a)** R_c = 1.8 nm (purple); **(b)** R_c = 2.05 nm (blue); **(c)** R_c = 2.5 nm (green); **(d)** R_c = 2.65 nm (red) as a function of the ratio between RBL molecules and γ-Ga_2O_3. Double exponential function fits are shown as a guide to the eye for the dyes and nanocrystals respectively.

As a verification of the FRET principle with γ-Ga_2O_3 nanocrystal as a donor and fluorescent dyes as acceptors, studies were conducted on environmental factors independent of Rhodamine derivatives: A565 and A590. Figure 3.11 shows representative data collected from the γ-Ga_2O_3 nanocrystals with sizes of R_c = 1.8 nm (a) and R_c = 2.65 nm (b) when assembled with increasing concentration of A565.

Figure 3.12 plots the corresponding normalized γ-Ga_2O_3 nanocrystals PL loss and the enhanced PL of A565 for this data set as a function of the A565 bound on the surface of the nanocrystals. For an equivalent acceptor valence, γ-Ga_2O_3 nanocrystal with R_c = 2.65 nm revealed a significantly higher FRET efficiency than the nanocrystals with R_c = 1.8 nm due to greater spectral overlap integral.

Given the results of the various combinations of fluorescent dyes with different sizes of γ-Ga_2O_3 nanocrystals, the interactions of various sizes of nanocrystals with a fluorescent dye with a more red-shifted emission were probed. This allows for the verification of whether the quenching could be extended to samples where the spectral overlap is significantly smaller.

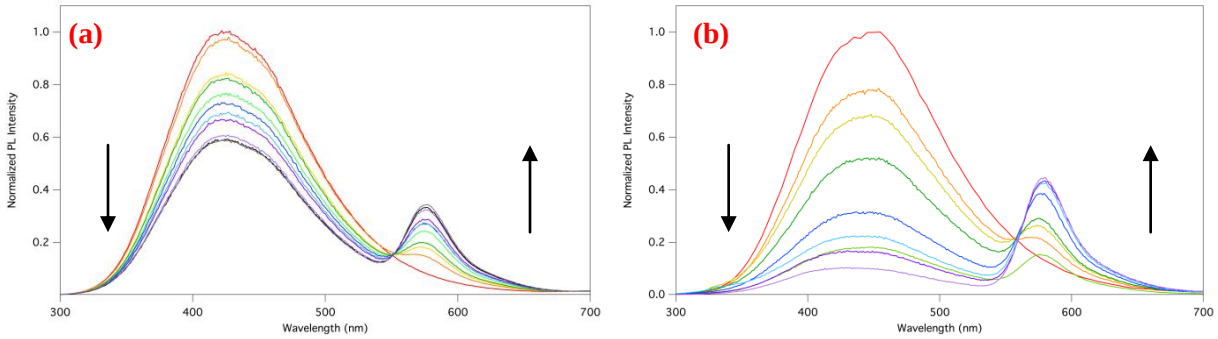

Figure 3.11. Steady-state PL spectra for various concentration of A565 with different sizes of γ-Ga_2O_3: **(a)** R_c = 1.8 nm and **(b)** R_c = 2.65 nm.

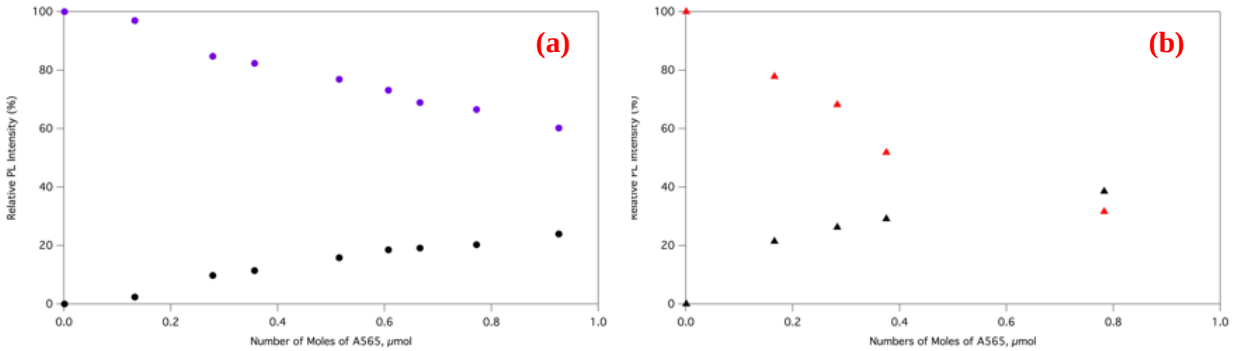

Figure 3.12. Relative PL intensities of the A565 (black) and nanocrystals with size of **(a)** R_c = 1.8 nm (purple); **(b)** R_c = 2.65 nm (red) as a function of the number of moles of A565 on the surface of the nanocrystals. Double exponential function fits are shown as a guide to the eye for the dyes and nanocrystals respectively.

The assembly of γ-Ga_2O_3 nanocrystal with R_c = 1.8 nm with A590 molecules demonstrates the feasibility of energy transfer from γ-Ga_2O_3 nanocrystal to fluorescent dyes with modest spectral overlap with increasing ratio of A590 (Figure 3.13). Similar to the data described for RBL and A565, the PL emission of γ-Ga_2O_3 nanocrystals were also strongly quenched in the presence of increased A590, with 2% quenching observed with *ca.* 0.1 μmol of A590, which increased to 35% at *ca.* 1 μmol of A590

molecules. Although the spectral overlap of γ-Ga_2O_3 (R_c = 1.8 nm) with A590 is 90.53% compared to that with RBL, this is compensated for by the extremely high QY of this fluorescent dye.

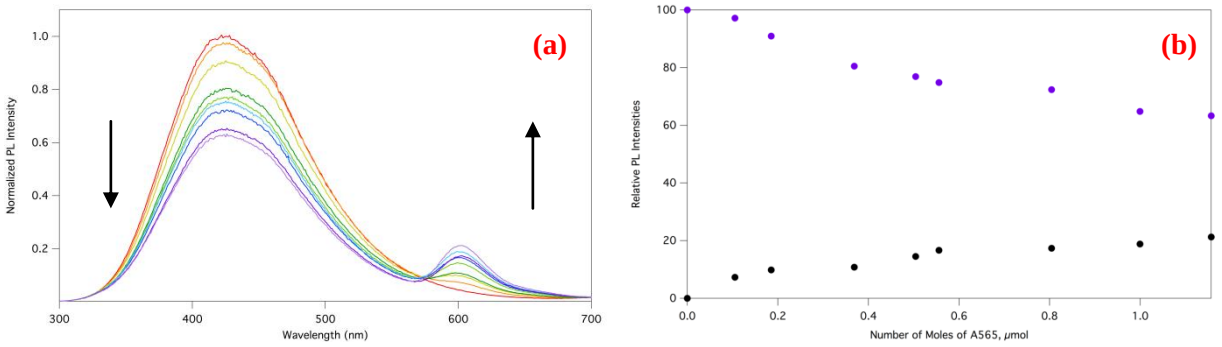

Figure 3.13. (a) Steady-state PL spectra for various concentration of A590 with γ-Ga_2O_3 of size R_c = 1.8 nm **(b)** Relative PL intensities of the data set in Figure 3.13 (a) with black and purple representing A590 and = 1.8 nm respectively. Double exponential function fits are shown as a guide to the eye for the dyes and nanocrystals respectively.

Analysis of the FRET between Rhodamine derivatives (RBL, A565, A590) and four sizes of γ-Ga_2O_3 (R_c = 1.8, 2.05, 2.5, 2.65 nm) were conducted based on the representative steady PL in Figure 3.14, 3.15 and 3.16. The samples were selected based on the two aspects of the γ-Ga_2O_3-RBL sample that yielded white-light-emission: absorbance of the γ-Ga_2O_3 at the band edge and the number of fluorescent dye molecules in the sample.

The FRET efficiencies of the hybrid nanostructures studied were utilized as a mechanism to probe the uniformity of the underlying assembly process by analyzing for significant deviations in the expected quenching kinetics. These would arise from heterogeneous incorporation of fluorescent dyes on the surface of γ-Ga_2O_3 nanocrystals, especially at low number of acceptors on the surface of the nanocrystals. Deviations of less than 5% were observed, however, suggesting that this was not a significant issue for the formation of FRET mediated white-light-emitting hybrid nanostructures consisting of γ-Ga_2O_3 and fluorescent dyes (RBL, A565, A590).

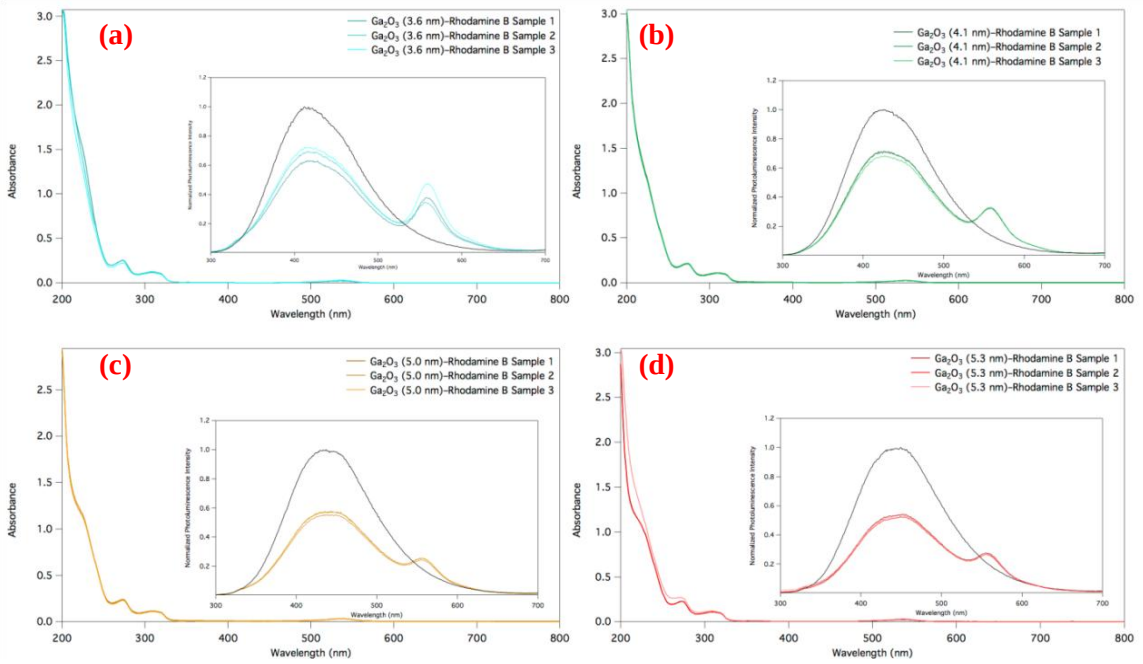

Figure 3.14. Representative absorption and steady-state PL spectra for RBL with various sizes of γ-Ga_2O_3 **(a)** R_c = 1.8 nm; **(b)** R_c = 2.05 nm; **(c)** R_c = 2.5 nm; **(d)** R_c = 2.65 nm.

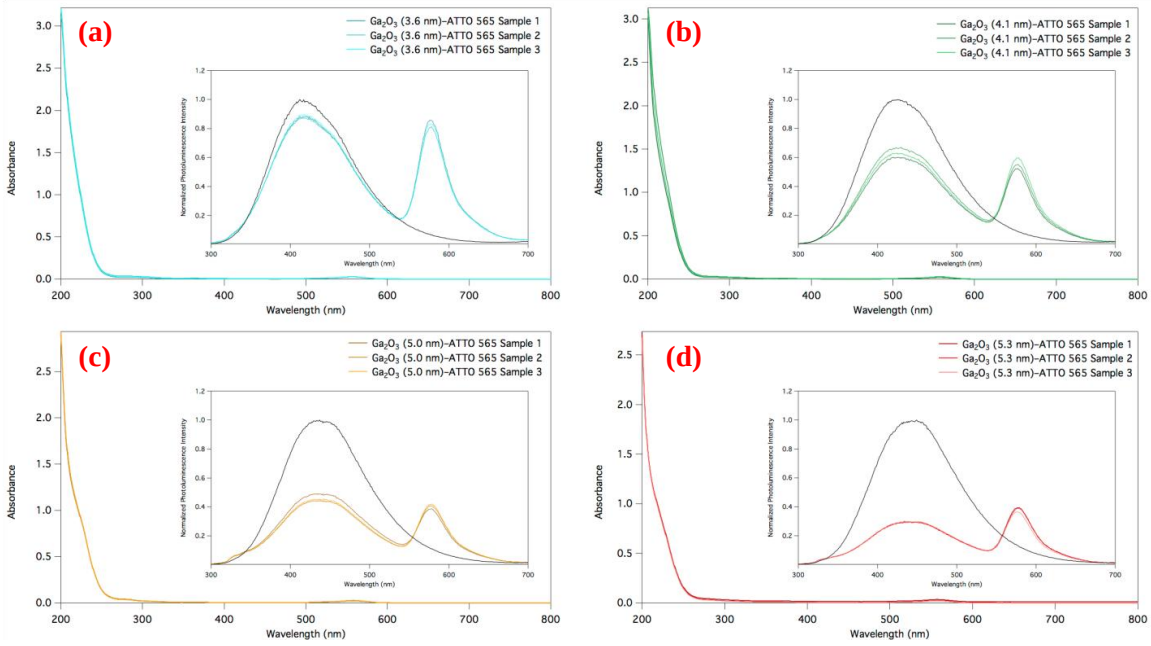

Figure 3.15. Representative absorption and steady-state PL spectra for A565 with various sizes of γ-Ga_2O_3 **(a)** R_c = 1.8 nm; **(b)** R_c = 2.05 nm; **(c)** R_c = 2.5 nm; **(d)** R_c = 2.65 nm.

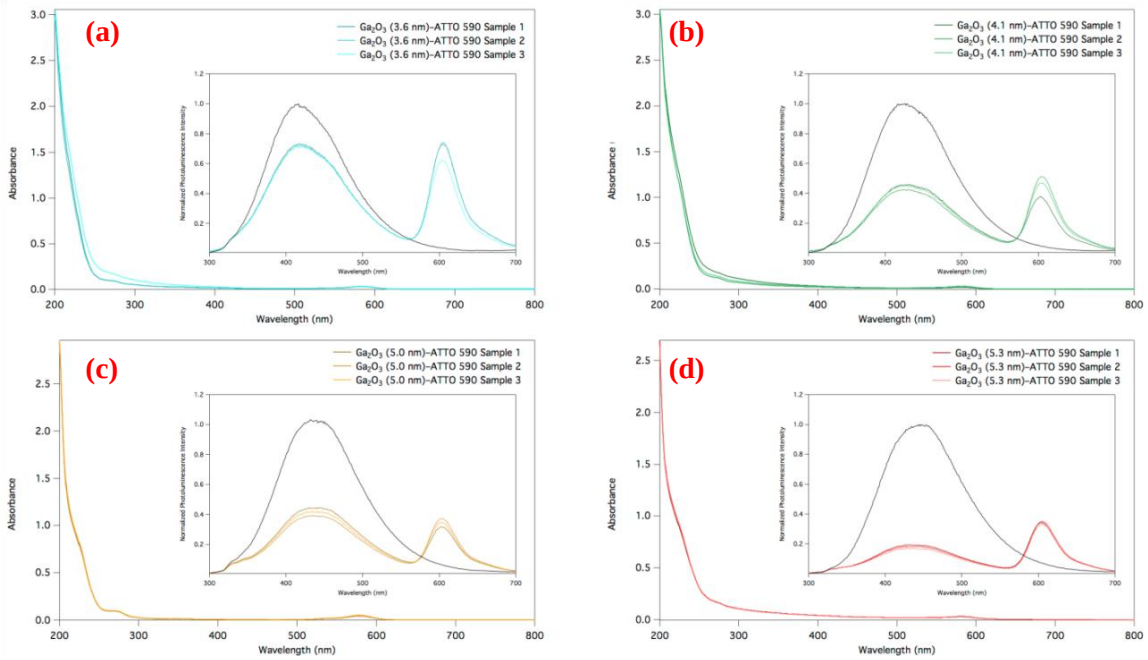

Figure 3.16. Representative absorption and steady-state PL spectra for A590 with various sizes of γ-Ga_2O_3 **(a)** R_c = 1.8 nm; **(b)** R_c = 2.05 nm; **(c)** R_c = 2.5 nm; **(d)** R_c = 2.65 nm.

The most efficient putative FRET was observed for the R_c = 2.65 nm nanocrystals with a FRET efficiency approaching 82% at a valence ≥ 50 RBL/γ-Ga_2O_3 nanocrystal. The nanocrystals with most probable sizes of R_c = 1.8, 2.05 and 2.65 nm approach efficiencies of 40%, 44%, and 65% respectively, at the same valence.

The aforementioned trend reflects that the lowest FRET efficiency (or nanocrystal PL loss) corresponds to the smallest γ-Ga_2O_3 nanocrystal size (415 nm emission) and progressively increases as the DAP emission maxima red shift and the donor-acceptor spectral overlap increases. To demonstrate the generality of the concept of the increasing of FRET efficiencies as the spectral overlap integrals increase, the study was conducted on various Rhodamine fluorescent dye derivatives and represented as Figure 3.17.

Within each individual Rhodamine derivative system, as the overlap integral increases, the FRET efficiencies were observed to be increasing (Figure 3.17). However, when the comparison was done across the different fluorescent dyes, the positively correlated trend between the FRET efficiencies and overlap integral was not apparent. The discrepancy may be attributed to i) the relative orientation of the transition dipole moments between the donor γ-Ga_2O_3 nanocrystals and the acceptor fluorescent dyes; ii)

environmental factor-based optical properties; iii) competing processes (e.g. dark state, nanocrystal-nanocrystal interactions, charge transfer).

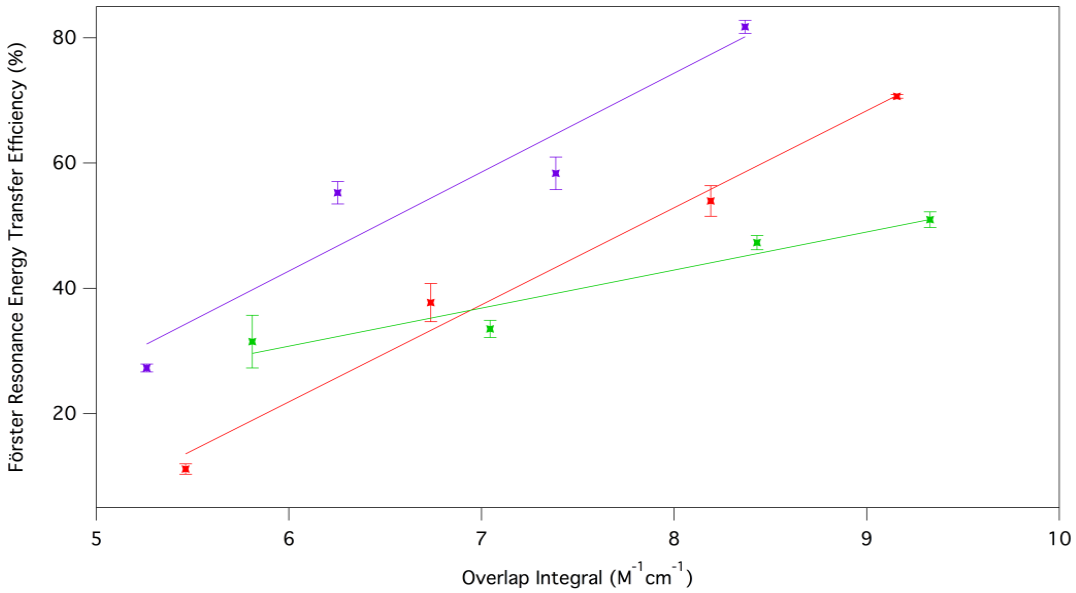

Figure 3.17. FRET efficiency as a function of spectral overlap integral for RBL (blue), A565 (red) and A590 (purple). The linear function fits are shown as a guide to the eye.

Corresponding FRET-related photophysical properties of the γ-Ga_2O_3 nanocrystals and fluorescent dyes derived from steady-state PL spectra were summarized in Table 3.3, 3.4 and 3.5. As the calculations of the FRET parameters are highly dependent on the optical properties of the donors and the acceptors, the critical distance and the distance between the donor-acceptor were observed to follow the trend of the quantum yield of the γ-Ga_2O_3 nanocrystals.

Further investigation of the FRET efficiency data with equations 17 and 19 yielded the experimental γ-Ga_2O_3 nanocrystal donor to fluorescent dye acceptor center-to-center separation distances (r_{DA}) and critical distance, R_0, listed in Table 3.3, 3.4 and 3.5 for RBL, A565 and A590 as acceptors respectively. These donor-acceptor separations ranged from 1.45 nm to 1.92 nm for different sizes of nanocrystal-based systems. As the size of the nanocrystals increase, the donor-acceptor distance increase, with the exception of nanocrystals with R_c = 2.65 nm, which has a lower quantum yield relative to the other γ-Ga_2O_3 nanocrystals.

Table 3.3. Selected photophysical properties of γ-Ga_2O_3-RBL nanostructures.

Most Probable R_c for Ga_2O_3 Particles (nm)	Calculated r_{D-A} (nm)	Calculated R_0 (nm)	FRET Efficiency (%)	Overlap Integral × 10^{14} (M^{-1} cm^3 nm^4)
1.80	1.57 ± 0.11	1.38	31.51 ± 0.04	5.81
2.05	1.72 ± 0.03	1.53	33.54 ± 0.01	7.04
2.50	1.76 ± 0.02	1.73	47.30 ± 0.01	8.43
2.65	1.63 ± 0.02	1.64	50.98 ± 0.01	9.33

Table 3.4. Selected photophysical properties of γ-Ga_2O_3-A565 nanostructures.

Most Probable R_c for Ga_2O_3 Particles (nm)	Calculated r_{D-A} (nm)	Calculated R_0 (nm)	FRET Efficiency (%)	Overlap Integral × 10^{14} (M^{-1} cm^3 nm^4)
1.80	1.66 ± 0.11	1.36	11.17 ± 0.01	5.46
2.05	1.67 ± 0.03	1.52	37.75 ± 0.03	6.74
2.50	1.92 ± 0.02	1.72	53.97 ± 0.02	8.19
2.65	1.42 ± 0.02	1.64	70.66 ± 0.00	9.16

Table 3.5. Selected photophysical properties of γ-Ga_2O_3-A590 nanostructures.

Most Probable R_c for Ga_2O_3 Particles (nm)	Calculated r_{D-A} (nm)	Calculated R_0 (nm)	FRET Efficiency (%)	Overlap Integral × 10^{14} (M^{-1} cm^3 nm^4)
1.80	1.45 ± 0.11	1.35	27.31 ± 0.64	5.26
2.05	1.59 ± 0.03	1.50	55.27 ± 1.78	6.25
2.50	1.60 ± 0.02	1.69	58.39 ± 2.60	7.39
2.65	1.26 ± 0.02	1.61	81.74 ± 1.04	8.37

Based on the FRET model, the rate of energy transfer for various γ-Ga_2O_3-fluorophore nanostructures can be approximated using equation 16, as reported in Table 3.6. The rate of energy transfer is highly dependent on many factors, such as the extent of spectral overlap, the relative orientation of the transition dipoles, the decay rate of the donor emission in absence of the acceptor, and, most importantly, the distance between the donor and acceptor molecules. The general trend for the energy transfer rate for each fluorophore hybrid systems is its positive correlation with the size of the nanocrystals. The deviation associated with γ-Ga_2O_3 nanocrystal size of 2.50 nm is believed to be caused by the increase in decay rate of its emission in the absence of the acceptor.

Table 3.6. Rate of FRET for various sizes of γ-Ga_2O_3 and different fluorescent dyes (RBL, A565, A590).

Most Probable R_c for Ga_2O_3 Particles (nm)	k_{ET} for RBL (ps^{-1})	k_{ET} for ATTO 565 (ps^{-1})	k_{ET} for ATTO 590 (ps^{-1})
1.80	18.93 ± 3.73	5.133 ± 0.44	15.33 ± 0.49
2.05	16.56 ± 1.02	19.96 ± 2.56	40.60 ± 3.00
2.50	16.79 ± 0.78	21.99 ± 2.12	26.34 ± 2.82
2.65	18.43 ± 0.93	43.63 ± 0.05	79.42 ± 5.59

3.3.2 Time-Resolved Photoluminescence Analyses

Analyses of the excited-state lifetime results corroborate the data collected in the steady-state measurements: significant γ-Ga_2O_3 donors quenching along with some acceptor sensitization, tracking the RBL assembly valence (Figure 3.18). All γ-Ga_2O_3-RBL assemblies undergo significant quenching and increase in decay rate in steady-state and time-resolved measurements respectively. As the concentration of RBL on the surface of the γ-Ga_2O_3 nanocrystals increase, the normalized PL intensity decrease in an increasing rate. This suggests that in developing an energy efficient system, the high quantity of valence acceptors may be detrimental as it quenches the long lifetime emission of the primary solid state phosphor.

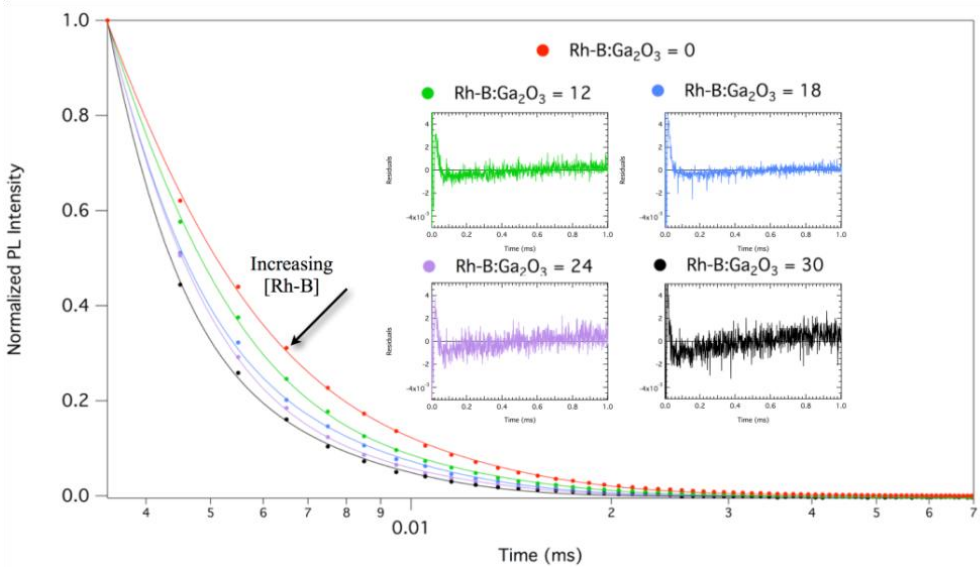

Figure 3.18. Excited-state lifetimes. Representative, normalized time-resolved PL decays of γ-Ga_2O_3 - RBL conjugates excited at 230 nm, monitoring the emission of the nanocrystal at 410 nm, with indicated increasing ratios of RBL per nanocrystal.

The γ-Ga_2O_3 decays for the γ-Ga_2O_3 – RBL hybrid nanostructures were fit to a bi-exponential function, and the corresponding average lifetimes (τ_{avg}) and individual lifetime components ($\tau_{1,2}$) along with their fractional amplitudes are presented in Table 3.7. The excited-state γ-Ga_2O_3 nanocrystals lifetime decreases significantly (*ca.* 43%) in the presence of RBL, diminishing from a τ_{avg} of 6.08 ms to 3.44 ms with an average valence of 12 RBL molecules. Lifetimes continue to decrease with an increasing ratio of RBL:Ga_2O_3 nanocrystals.

Table 3.7. Lifetime of γ-Ga_2O_3 of the γ-Ga_2O_3-RBL nanostructures at selected conjugate ratios

		Lifetime (ms)[a]	
RBL:Ga_2O_3 Ratio	**τ_{avg} (% quenching)**	**τ_1**	**τ_2**
0	6.08 (0)	8.53 (64.67%)	1.59 (35.326)
12	3.44 (43)	1.46 (50.58%)	5.46 (49.41%)
18	3.42 (44)	4.21 (77.71%)	1.05 (13.44%)
24	2.74 (55)	4.28 (59.72%)	1.13 (16.45%)
30	1.98 (67)	3.37 (47.61%)	0.827 (45.12%)

[a] Amplitude weighted as described and fitted with bi-exponential function. The lifetime component(s) are given along with their fractional intensity.

Sensitized lifetimes of fluorescent dyes (RBL, A565 and A590) when conjugated on the surface of the γ-Ga_2O_3 nanocrystals were also examined, as shown in Figure 3.19, 3.20 and 3.21. The lifetime values from fitting these decay profiles with a bi-exponential function are presented in Table 3.8. In comparison with the direct excitation of the fluorescent dyes, the FRET-based sensitized excitation of the dyes demonstrated lifetimes with an increase by two orders of magnitude.

The importance of the dramatic change in the sensitized emission of the fluorescent dyes demonstrates that the nanocrystals and the chromophores act in-sync as an internal relaxation upon the excitation of the γ-Ga_2O_3 nanocrystals. It extends the lifetime of the chomophore and this internal relaxation act as a sign for a quasi single chromophore. The in-sync emission between the nanocrystals and the secondary chromophore is the model methodology in the design of a white-light-emitting hybrid nanomaterial that is developed and reported in this thesis.

There are two factors that may account for this extraordinary energy transfer efficiency and enhancement in the excited-state lifetime of the organic dyes: amplification of the quenching via rapid internal energy or charge transfer and efficient energy transfer. Nanocrystals, which span a variety of sizes, can conjugate with fluorescent dyes and act as donors. The size tunability of the nanocrystals allows versatile conjugation with the fluorescent dyes that are highly responsive as acceptors. The sensitized

excitation increases the sensitivity of their responses, however, their interactions and dynamics may not be influential on the mechanism of these responses.

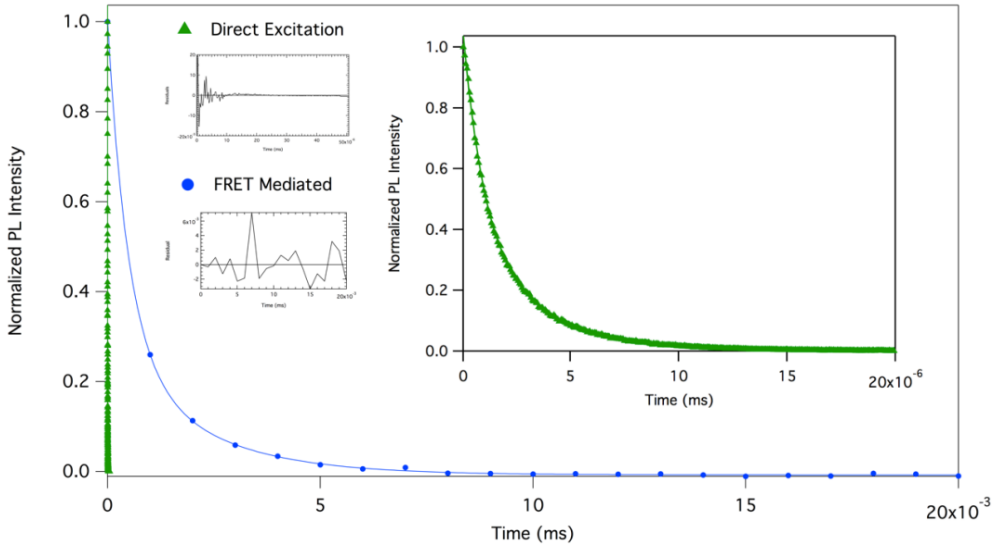

Figure 3.19. Excited-state lifetimes. Representative, normalized time-resolved PL decays of γ-Ga_2O_3 - RBL conjugates, monitoring the emission of RBL with direct (green) and sensitized (blue) excitation. Inset: Time-resolved decay of the direct excitation curve in the nanosecond timescale.

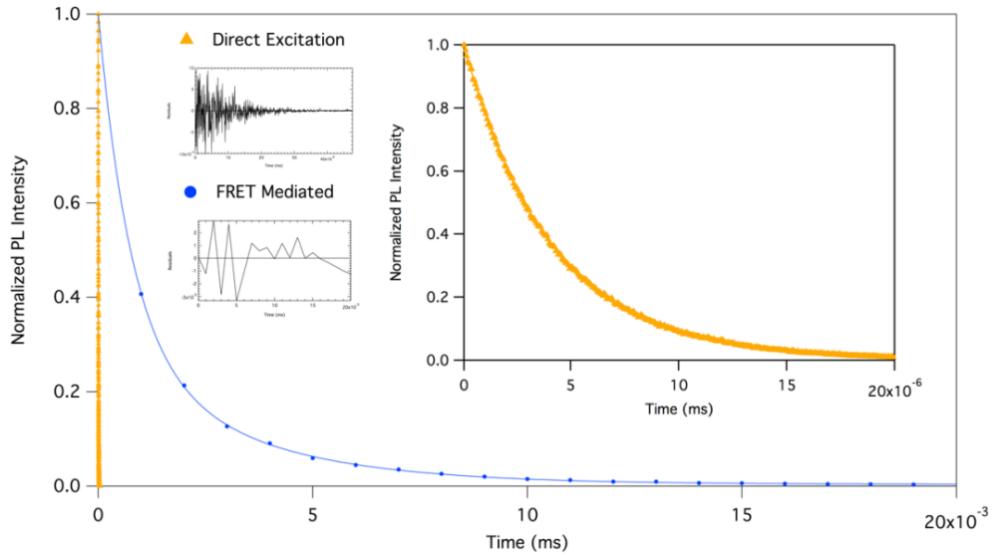

Figure 3.20. Excited-state lifetimes. Representative, normalized time-resolved PL decays of γ-Ga_2O_3 - A565 conjugates, monitoring the emission of A565 with direct (orange) and sensitized (blue) excitation. Inset: Time-resolved decay of the direct excitation curve in the nanosecond timescale.

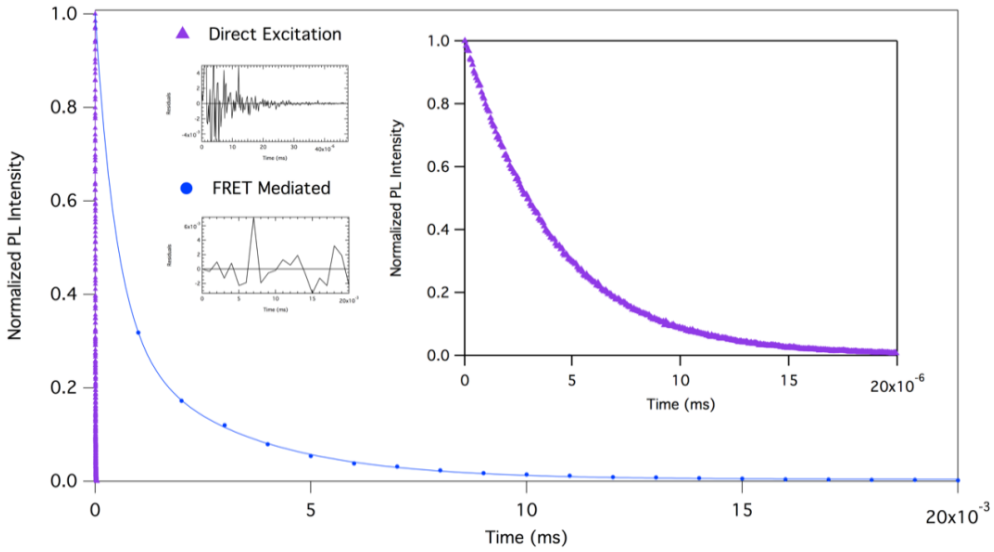

Figure 3.21. Excited-state lifetimes. Representative, normalized time-resolved PL decays of γ-Ga_2O_3 - A590 conjugates, monitoring the emission of A590 with direct (purple) and sensitized (blue) excitation. Inset: Time-resolved decay of the direct excitation curve in the nanosecond timescale.

Table 3.8. Lifetime of the fluorescent dyes on the hybrid nanostructures by direct excitation or sensitized (FRET-based) mediated excitation

Nanostructure of Interest		Lifetime[a]			
		τ_{avg}	τ_1	τ_2	τ_3
RBL	Direct Excitation	2.43 ns	3.78 ns (10.14%)	1.72 ns (29.52%)	0.47 ns (60.34%)
	FRET Mediated	1.45 µs	0.77 µs (69.69%)	3.05 µs (29.92%)	0.00 µs (0.00%)
A565	Direct Excitation	4.03 ns	4.60 ns (71.20%)	2.63 ns (28.80%)	0.00 ns (0.00%)
	FRET Mediated	0.94 µs	0.48 µs (71.82%)	2.03 µs (28.93%)	0.00 µs (0.00%)
A590	Direct Excitation	3.44 ns	4.27 ns (56.80%)	3.57 ns (28.50%)	0.00 ns (0.00%)
	FRET Mediated	1.25 µs	0.49 µs (66.87%)	2.83 µs (32.73%)	0.00 µs (0.00%)

[a] Amplitude weighted as described and fitted with bi-exponential or tri-exponential function. The lifetime component(s) are given along with their fractional intensity.

3.3.3 Theoretical Studies on the Fluorophore Derivatives-Ga_2O_3 Nanostructures

To support the explanation for the observed absorption, steady-state and time-resolved emission characteristics of the hybrid nanostructure, the electronic structure of the individual components have

been determined by calculations. The computational methodologies have been used to elucidate the electronic structure and the configuration of organic molecules in hybrid nanostructures. The electronic structure and absorption spectra may shed light on the interactions between the nanocrystals and the fluorescent dyes.

The results of the calculations of the organic fluorescent dyes' electronic structure and the structural configuration were directly correlated to the experimental spectroscopic data. The comparison served to rationally predict and design the properties of the complex hybrid nanomaterials for the targeted application: FRET-mediated white-light-emitting phosphors.

The nature of the excited states for the Rhodamine fluorophore derivatives giving rise to the UV-Vis spectrum is analyzed to rationalize the moiety of the organic molecules that are accountable for the emission in the visible region of the spectrum. To understand the effect of solvents on the molecular and electronic structures of the fluorescent dyes, the calculated absorption spectra and the molecular orbitals involved in the transition moments for Rh-B and RBL are illustrated in Figure 3.22 and 3.23 respectively. Results for transitions giving rise to the representative spectroscopic bands are reported in the corresponding figure.

The effect of Rh-B in different solvent environments has been investigated. As expected, for Rh-B in water, the spectrum is constituted by the π to π^* transitions of the conjugated rings in the high wavelength region. In particular, the transitions represented at the wavelengths of 551 and 488 nm show a dominant participation of the 3*H*-xanthene moiety in the virtual natural bonding orbital. Conversely, the less intense band comprised between 200 and 500 nm is more complicated and the excitation process is evidently accompanied by a certain relocation of the electron density from the 3*H*-xanthene and the phenyl ring moiety. The mixed character of transitions even at high energy can have important consequences over the complicated photophysical properties.

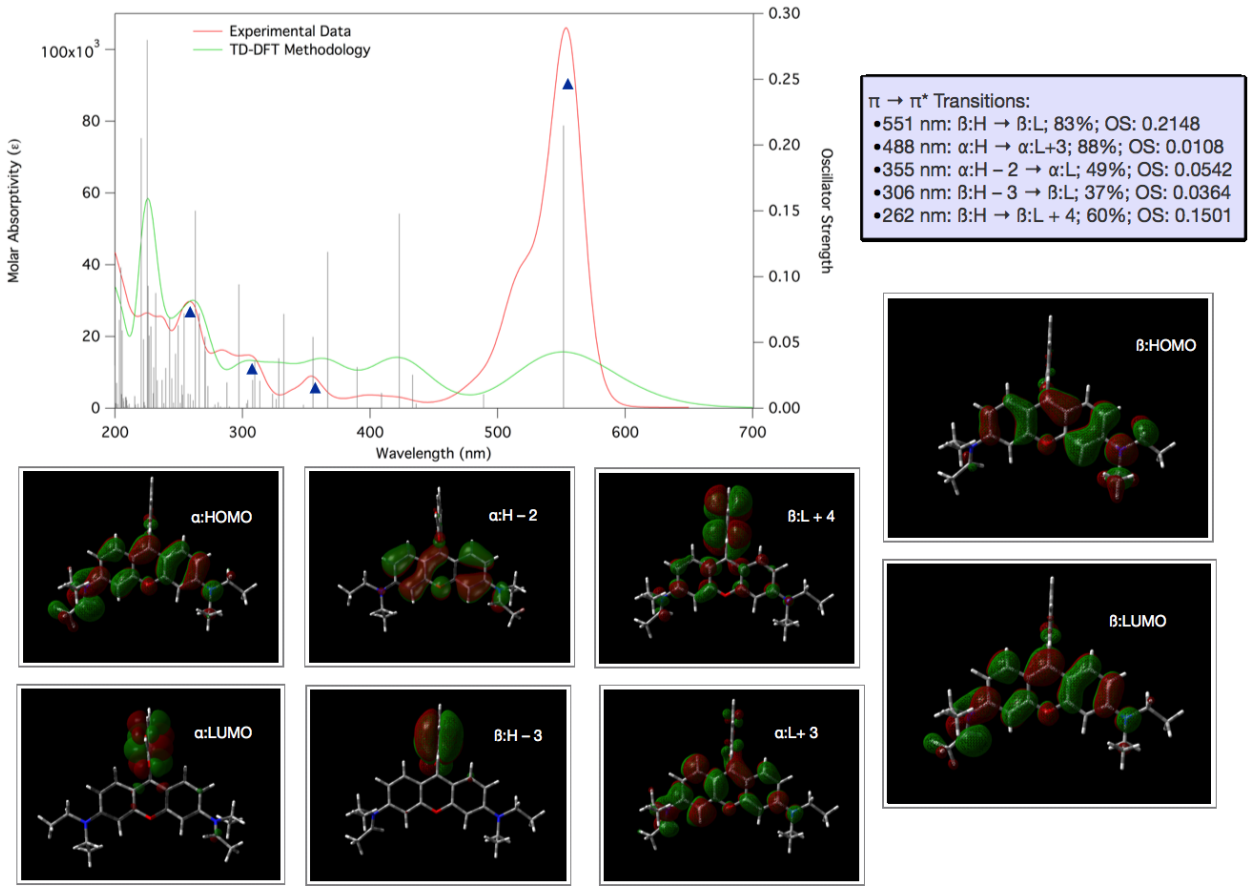

Figure 3.22. Absorption spectra and the involved MO of Rh-B in H_2O: red trace – experimental; green trace – computed by TD-DFT methodology; grey bars – computed oscillator strength.

The Rh-B molecules cyclize and result in the formation of RBL molecules due to its sensitivity to the surrounding chemical environment. To conduct the comparison with the experimental data, the absorption spectrum of the RBL in hexane was calculated based on the use of the PCM method to implicitly take into account the electrostatic effects of the environment. The electronic transitions are attributed by the mixed character of transitions, which is caused by the interruption of the π-electron system. The oscillator strength of the RBL molecules is observed to be significantly stronger for transitions in the higher energy region.

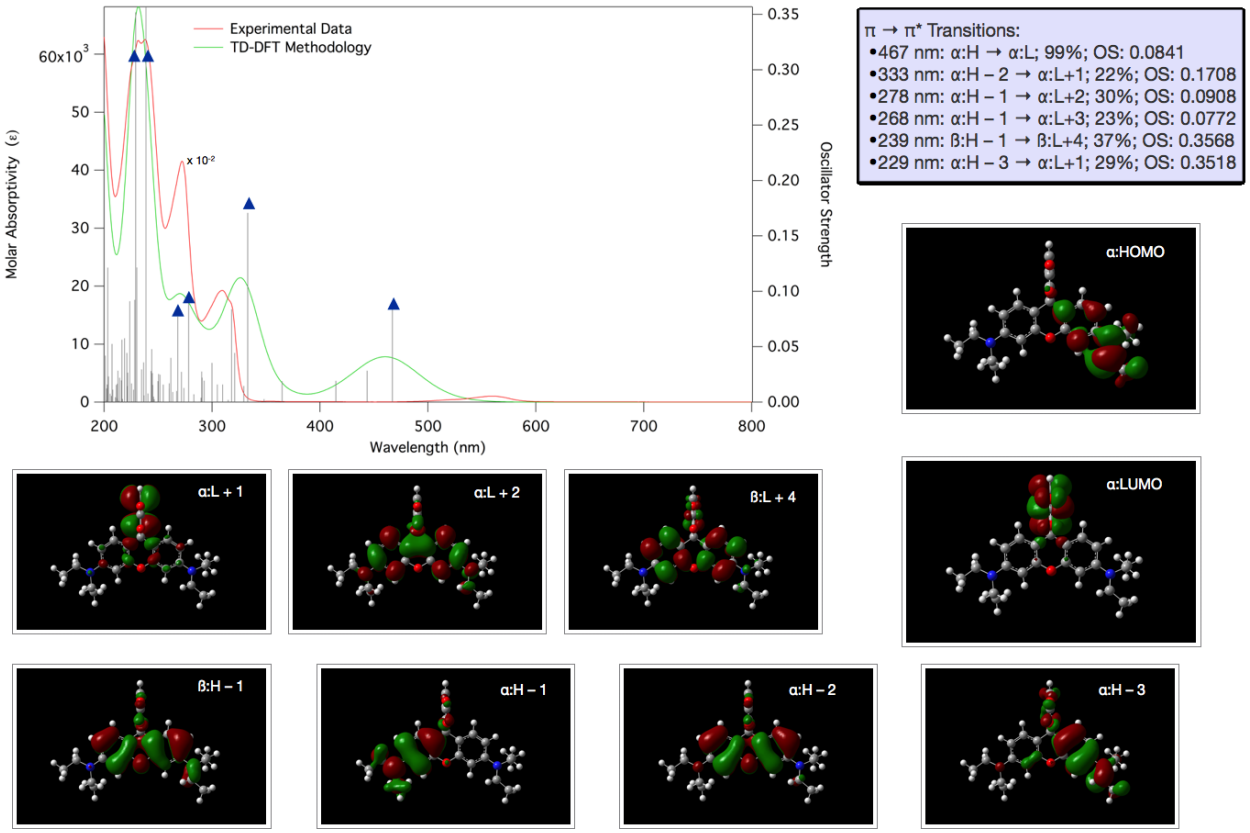

Figure 3.23. Absorption spectra and the involved MO of RBL in hexane: red trace – experimental; green trace – computed by TD-DFT methodology; grey bars – computed oscillator strength.

The molecular and electronic structures of the ATTO series fluorophore, A565 and A590, have been theoretically computed and illustrated as Figure 3.24 and 3.25 respectively. Due to its molecular structural rigidity, the optimized structures of the ATTO fluorescent dyes retained their dicarboxyphenyl form instead of benzofuran structure when dispersed in non-polar solvents.

Similar to the excited states of Rh-B molecules in water, the electronic transition band of A565 and A590 in the visible region is comprised of the π to π* transitions originated from 3*H*-xanthene conjugated rings. The calculated absorption spectrum of A565 is observed to possess a broad band in the visible region with considerably stronger oscillator strength. On the contrary, the excited states of A590 revealed a wider distribution of various transitions with mixed of transition characters with comparable oscillator strengths. This observation suggested that the solvatochromic effect on the absorption energies is expected to be insignificant in the ATTO series fluorescent dyes. Based on the understanding of these

electronic structures of the fluorescent dyes of interest, it allowed for further confirmation regarding the existence of the π-electron interruption only observed in RBL in non-polar solvents.

Discrepancies have been observed when comparing the calculated and experimental spectroscopic data, which may be attributed by the drawback of the use of basis set and other potential interactions between the fluorescent dye molecules that were not accounted for in the theoretical predictions of the absorption spectra. Despite the presence of these deviations, the calculated results may serve as qualitative supporting information in hypothesizing the interactions between the nanocrystals and the fluorescent dyes.

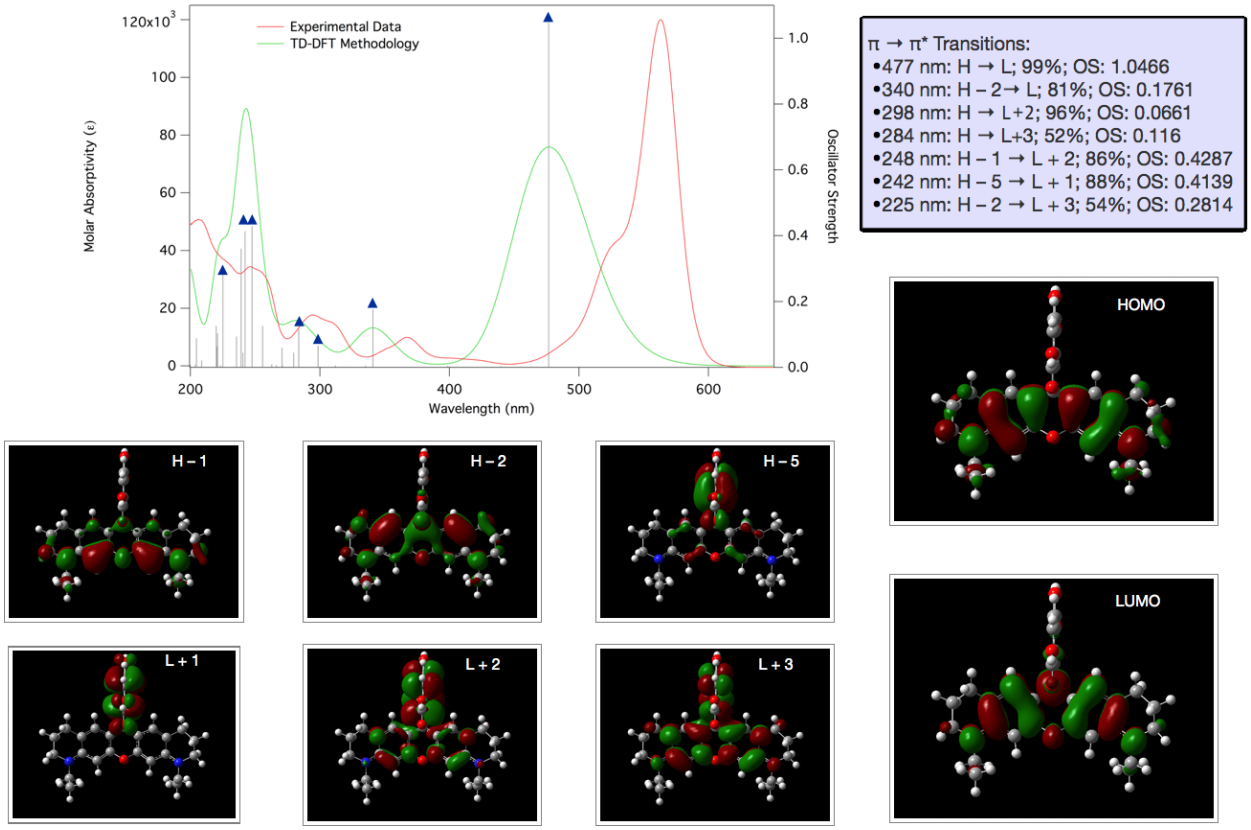

Figure 3.24. Absorption spectra and the involved MO of A565 in hexane: red trace – experimental; green trace – computed by TD-DFT methodology; grey bars – computed oscillator strength.

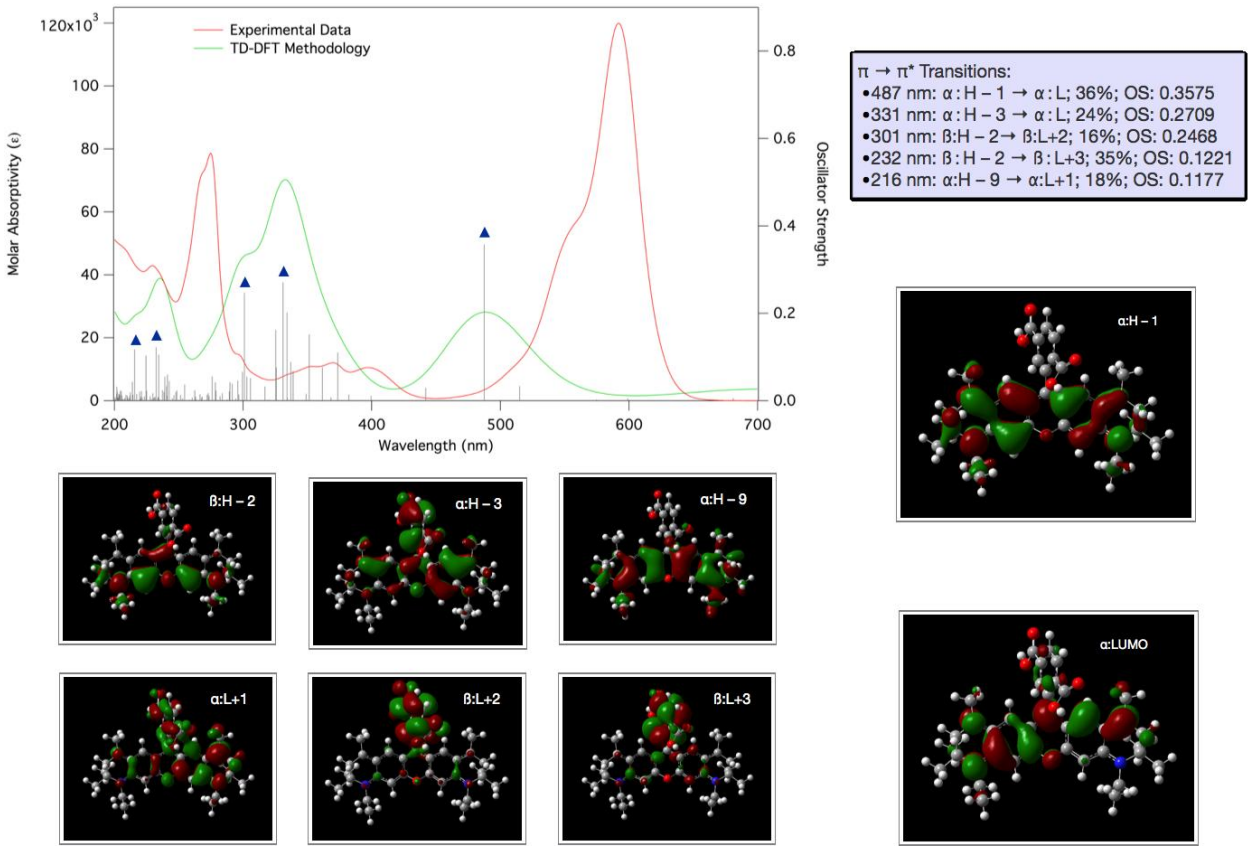

Figure 3.25. Absorption spectra and the involved MO of A590 in hexane: red trace – experimental; green trace – computed by TD-DFT methodology; grey bars – computed oscillator strength.

Investigations with the various Rhodamine fluorophore derivatives that functioned as either donors/acceptors in the electron/energy transfer systems led to the study of their interactions with Ga_2O_3 nanocrystals. As the basis of the hypothesis to the mechanistic behavior of the focused hybrid nanostructure system, Ga_2O_3-RBL, the relative electronic energy difference between Ga_2O_3 and the RBL fluorophore has been compared. The energetic values for the valence and conduction band, VB and CB respectively, of the Ga_2O_3 donor species were determined to be -2.95 eV and -7.85 eV (vs absolute vacuum scale, AVS) respectively.[85] The lowest unoccupied molecular orbital (LUMO) of the RBL fluorophore was determined to be -3.71 eV (vs AVS).

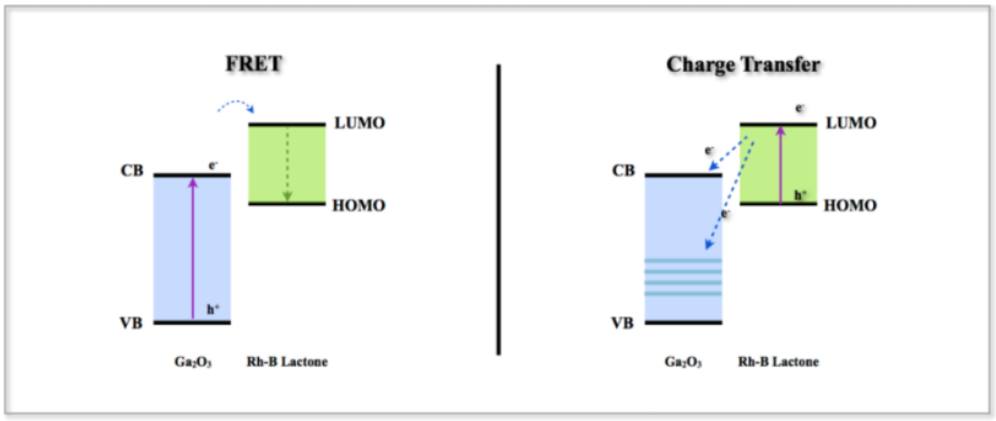

Figure 3.26. Diagram of the relative electronic energy difference between Ga_2O_3 as the donor and RBL fluorophore accepting species for Ga_2O_3-RBL hybrid nanostructures for the rationalization of charge/energy transfer

Two alternate transfer processes are predicted as being possible for quenching for the Ga_2O_3 nanocrystal PL in the conjugated Ga_2O_3/dye system by examining the overall fluorescent dye-Ga_2O_3 nanocrystal spectra in conjunction with the relative energy levels. The first transfer process considered is the FRET from the photoexcited Ga_2O_3 nanocrystal donor to the fluorescent dye molecule acceptors arrayed around its surface. The photoexcited Ga_2O_3 nanocrystal transferred the energy to the fluorescent dye acceptors *via* dipole-dipole Förster coupling, which resulted in the quenching of the nanocrystal PL and a sensitized acceptor emission. The second process is based on charge transfer, where the directly photoexcited fluorescent dye molecules, are able to transfer electrons to the Ga_2O_3 nanocrystal. Due to its short lifetime, the charge transfer of an electron from the fluorescent dye molecule to the Ga_2O_3 nanocrystal is not favorable, but cannot be unambiguously ruled out.

In the case of RBL, as the LUMO of the fluorescent dye is higher compared with the CB of the Ga_2O_3 nanocrystal (Figure 3.27), the photoexcited electrons can transfer from the LUMO of the RBL molecules to the CB of the nanocrystals, contrarily, the photoexcited holes migrate from the HOMO of the dye molecules to the VB of the nanocrystals under UV irradiation. Under such circumstances, the emission in the high wavelength region of the visible spectrum will not be observable, rendering this mechanism being highly improbable when compared with the experimental data. Alternatively, the probability of the occurrence for the FRET process, which is dependent on the dipole-dipole coupling of the two components, is higher based on the theoretical rationale proposed.

For Rh-B, A565 and A590, where their π-electron system remain uninterrupted, the low energy transition bands in the range of *ca.* 500 – 600 nm are observed in both theoretical modeling and experimental data. On the basis of the narrow energy gap of the transition of interest, the photoexcited electrons can transfer from the CB of the Ga_2O_3 nanocrystal and the photoexcited holes can be transported from the HOMO of the fluorescent dyes to the VB of the nanocrystal. This process restrained the occurrence of dark state in these hybrid nanostructures. Due to the extremely high extinction coefficient for the ATTO series fluorescent dyes, which gives rise to the large spectral overlap with the Ga_2O_3 nanocrystal, the FRET from the nanocrystal to the fluorescent dyes is probable.

The two processes that are suggested to be mediating the white-light-emission of the hybrid nanostructure, energy transfer and charge transfer, are highly distance dependent. FRET is governed by a $1/r^6$ dependence and is dictated by the donor fluorescence quantum yield and the donor-acceptor dipole-dipole interactions. The latter is determined by the spectral overlap between the luminescence and the absorption bands of the donor and the acceptor, respectively. Charge transfer that occurs *via* superexchange tends to decay exponentially with distance and is dependent on the Gibbs free energy, ΔG, for the charge transport from the donor to the acceptor. Depending on the distance between the donor and the acceptor, the charge transfer rate varies: with long separation distance (> 10nm), the charge transfer rate is slower in comparison with the FRET process. At a distance of less than 10 nm, the two processes proceed at a fast rate and would compete, however, the underlying mechanism for the two competing processes remain unclear.

The quenching by the Ga_2O_3 nanocrystals proximity effect, which the neighboring nanocrystals interact with one another, is not considered; this scenario would have manifested a linear quenching response that can be characterized by a Stern-Volmer function and would not result in the sensitized emission of the fluorescent dyes in the visible region of the hybrid nanostructure systems under UV radiation.

Given the nanocrystal donor-fluorescent dye acceptor distance separation in the hybrid nanostructure systems, the Dexter energy transfer mechanism is also not considered. This process occurs between two molecules bilaterally exchanging their electrons and typically happens within 1 nm. Unlike the FRET process, which has a transfer rate with a six-power distance dependency, the Dexter energy transfer rate exponentially decays as the donor-acceptor separation distance increases. Based on this

argument, the probability for a Dexter energy transfer to occur is moderately low as it requires the fluorescent dye to bind to the acceptor sites and will not yield an observable sensitized dye emission.

Investigating the relative energy levels of the two components in conjunction with the fluorescent dye binding sites on the surface of the Ga_2O_3 nanocrystals support the following hypotheses: i) Dexter energy transfer is not viable in these hybrid nanostructures; ii) competition between the charge transfer and the energy transfer processes for Rh-B, A565, and A590 fluorescent dyes is possibly occurring.

Chapter 4

4.1 Characterization of the Chromaticity of γ-Ga_2O_3 – Fluorescent Dyes Nanostructures

4.1.1 Tunable Chromaticity of γ-Ga_2O_3 – Fluorescent Dyes Nanostructures

Rationalized strategies in tailoring the performance of the white-light-emitting materials is demonstrated by modulating the emission properties of the hybrid nanocomposite materials, *via* tuning the host composition and the interaction process between the fluorescent dyes and the TCO nanocrystals. White-light is induced by the combination of three primary colours (blue, green and red) or two complementary colours (blue and orange or cyan and red). The functional basis of the white-light-emitting nanomaterial is a strong broad-band, long-lifetime emission of the colloidal metastable γ-Ga_2O_3 nanocrystals that are size-tunable from the violet to cyan region (405-465 nm) of the visible spectrum.

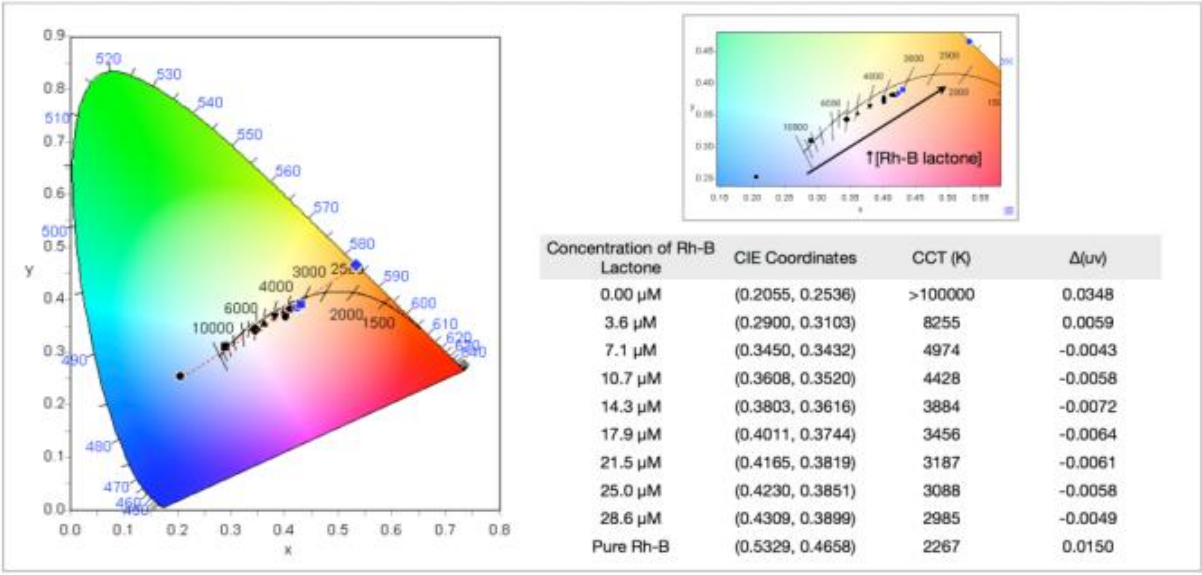

Concentration of Rh-B Lactone	CIE Coordinates	CCT (K)	Δ(uv)
0.00 μM	(0.2055, 0.2536)	>100000	0.0348
3.6 μM	(0.2900, 0.3103)	8255	0.0059
7.1 μM	(0.3450, 0.3432)	4974	-0.0043
10.7 μM	(0.3608, 0.3520)	4428	-0.0058
14.3 μM	(0.3803, 0.3616)	3884	-0.0072
17.9 μM	(0.4011, 0.3744)	3456	-0.0064
21.5 μM	(0.4165, 0.3819)	3187	-0.0061
25.0 μM	(0.4230, 0.3851)	3088	-0.0058
28.6 μM	(0.4309, 0.3899)	2985	-0.0049
Pure Rh-B	(0.5329, 0.4658)	2267	0.0150

Figure 4.1. The CIE chromaticity diagram of the γ–Ga_2O_3 – RBL nanostructure with the corresponding concentration of RBL arrayed around the surface of nanocrystals with R_c = 1.8 nm.

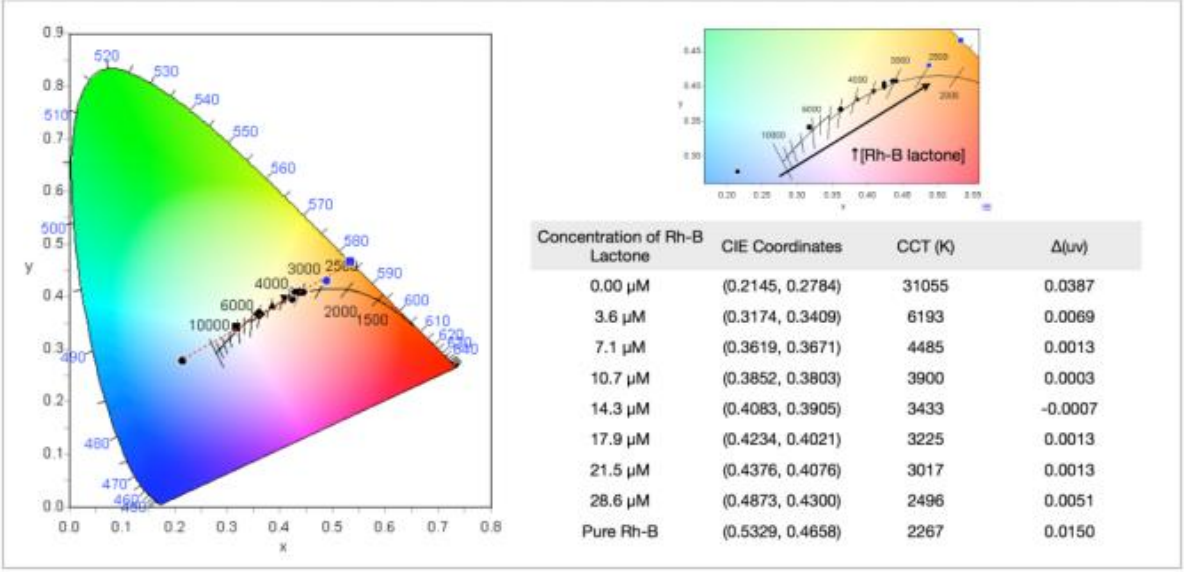

Concentration of Rh-B Lactone	CIE Coordinates	CCT (K)	Δ(uv)
0.00 μM	(0.2145, 0.2784)	31055	0.0387
3.6 μM	(0.3174, 0.3409)	6193	0.0069
7.1 μM	(0.3619, 0.3671)	4485	0.0013
10.7 μM	(0.3852, 0.3803)	3900	0.0003
14.3 μM	(0.4083, 0.3905)	3433	-0.0007
17.9 μM	(0.4234, 0.4021)	3225	0.0013
21.5 μM	(0.4376, 0.4076)	3017	0.0013
28.6 μM	(0.4873, 0.4300)	2496	0.0051
Pure Rh-B	(0.5329, 0.4658)	2267	0.0150

Figure 4.2. The CIE chromaticity diagram of the γ–Ga_2O_3 – RBL nanostructure with the corresponding concentration of RBL arrayed around the surface of nanocrystals with R_c = 2.05 nm.

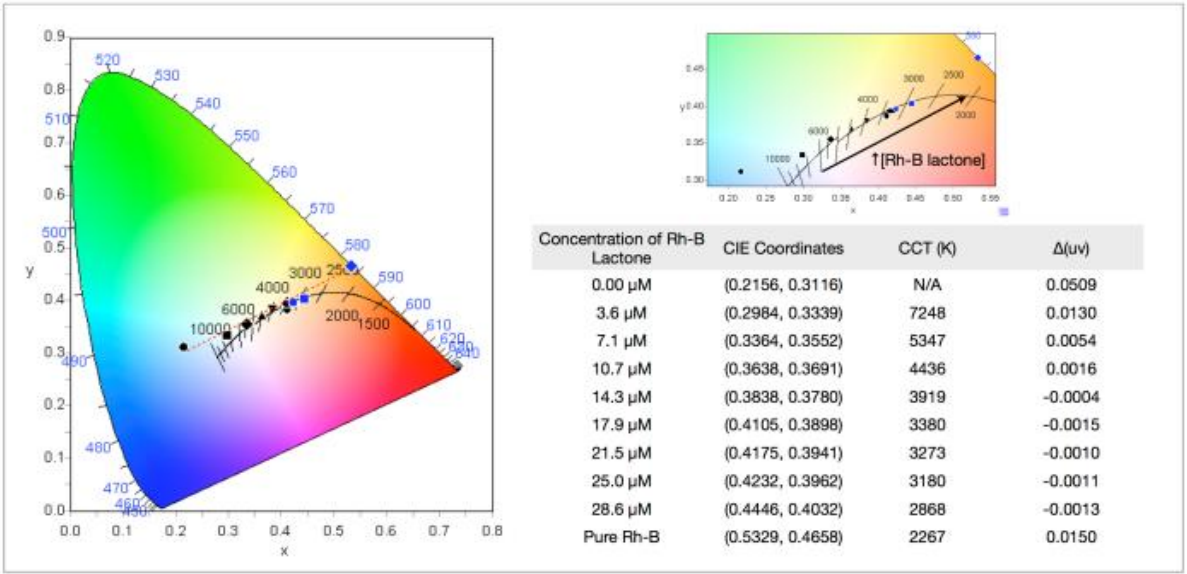

Concentration of Rh-B Lactone	CIE Coordinates	CCT (K)	Δ(uv)
0.00 μM	(0.2156, 0.3116)	N/A	0.0509
3.6 μM	(0.2984, 0.3339)	7248	0.0130
7.1 μM	(0.3364, 0.3552)	5347	0.0054
10.7 μM	(0.3638, 0.3691)	4436	0.0016
14.3 μM	(0.3838, 0.3780)	3919	-0.0004
17.9 μM	(0.4105, 0.3898)	3380	-0.0015
21.5 μM	(0.4175, 0.3941)	3273	-0.0010
25.0 μM	(0.4232, 0.3962)	3180	-0.0011
28.6 μM	(0.4446, 0.4032)	2868	-0.0013
Pure Rh-B	(0.5329, 0.4658)	2267	0.0150

Figure 4.3. The CIE chromaticity diagram of the γ–Ga_2O_3 – RBL nanostructure with the corresponding concentration of RBL arrayed around the surface of nanocrystals with R_c = 2.5 nm.

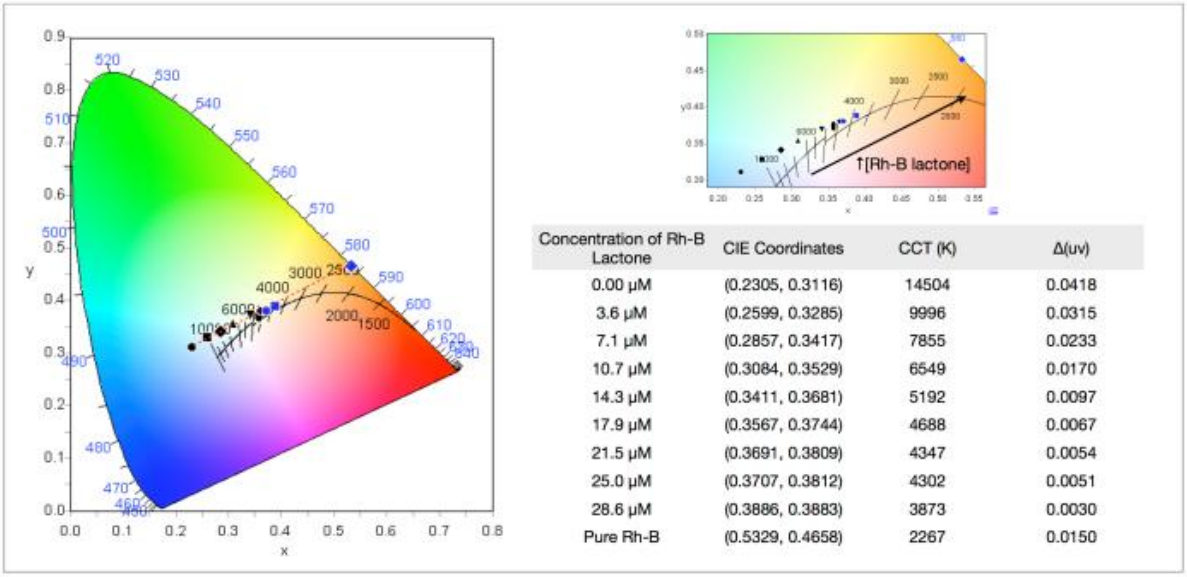

Concentration of Rh-B Lactone	CIE Coordinates	CCT (K)	Δ(uv)
0.00 μM	(0.2305, 0.3116)	14504	0.0418
3.6 μM	(0.2599, 0.3285)	9996	0.0315
7.1 μM	(0.2857, 0.3417)	7855	0.0233
10.7 μM	(0.3084, 0.3529)	6549	0.0170
14.3 μM	(0.3411, 0.3681)	5192	0.0097
17.9 μM	(0.3567, 0.3744)	4688	0.0067
21.5 μM	(0.3691, 0.3809)	4347	0.0054
25.0 μM	(0.3707, 0.3812)	4302	0.0051
28.6 μM	(0.3886, 0.3883)	3873	0.0030
Pure Rh-B	(0.5329, 0.4658)	2267	0.0150

Figure 4.4. The CIE chromaticity diagram of the γ–Ga_2O_3 – RBL nanostructure with the corresponding concentration of RBL arrayed around the surface of nanocrystals with R_c = 2.65 nm.

The tunability of the hybrid nanocomposite originates from the amount of the fluorescent dye-acceptor that is bound to the surface of the nanocrystal-donor and the electronic structure of the individual components. By increasing the acceptor to donor ratio, the probability of transferring energy is higher than emitting energy in the form of fluorescence. The white-light-emitting nanomaterial utilizes the TCO nanocrystals and the functional group mediated surface-bound fluorescent dyes as fundamental building blocks to achieve a single emitting layer that requires one excitation energy source.

As illustrated in Figure 4.1 – Figure 4.4 (γ–Ga_2O_3 – RBL), 4.5 and 4.6 (γ–Ga_2O_3 – A565) and 4.7 (γ–Ga_2O_3 – A590), the emission of the hybrid nanocomposites can be finely tuned by the electronic structure of the nanocrystal and/or the secondary fluorescent dye chromophore and varying the amount of fluorescent dyes bound to the surface of the nanocrystals. The characteristics of visible light (CIE coordinates and CCT) generated from these hybrid nanostructures are tabulated in the corresponding figures for different systems. The distance from the Planckian locus (Δ*uv*), in other words, the degree of departure from a black body, is also reported in the table.

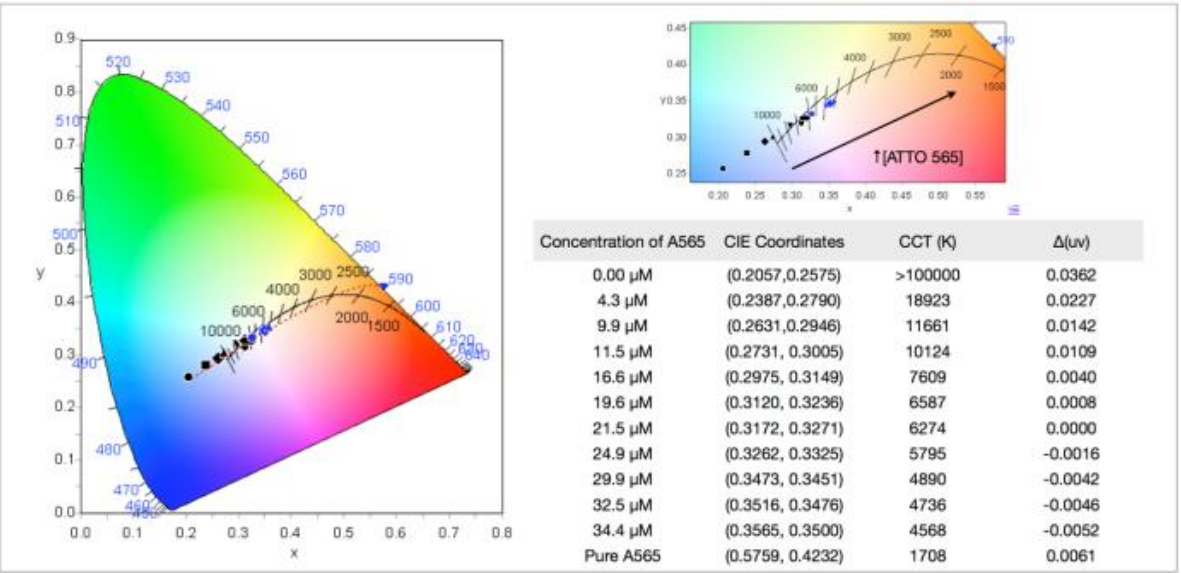

Concentration of A565	CIE Coordinates	CCT (K)	Δ(uv)
0.00 µM	(0.2057,0.2575)	>100000	0.0362
4.3 µM	(0.2387,0.2790)	18923	0.0227
9.9 µM	(0.2631,0.2946)	11661	0.0142
11.5 µM	(0.2731, 0.3005)	10124	0.0109
16.6 µM	(0.2975, 0.3149)	7609	0.0040
19.6 µM	(0.3120, 0.3236)	6587	0.0008
21.5 µM	(0.3172, 0.3271)	6274	0.0000
24.9 µM	(0.3262, 0.3325)	5795	-0.0016
29.9 µM	(0.3473, 0.3451)	4890	-0.0042
32.5 µM	(0.3516, 0.3476)	4736	-0.0046
34.4 µM	(0.3565, 0.3500)	4568	-0.0052
Pure A565	(0.5759, 0.4232)	1708	0.0061

Figure 4.5. The CIE chromaticity diagram of the γ–Ga_2O_3 – A565 nanostructure with the corresponding concentration of A565 arrayed around the surface of the nanocrystals with R_c = 2.65 nm.

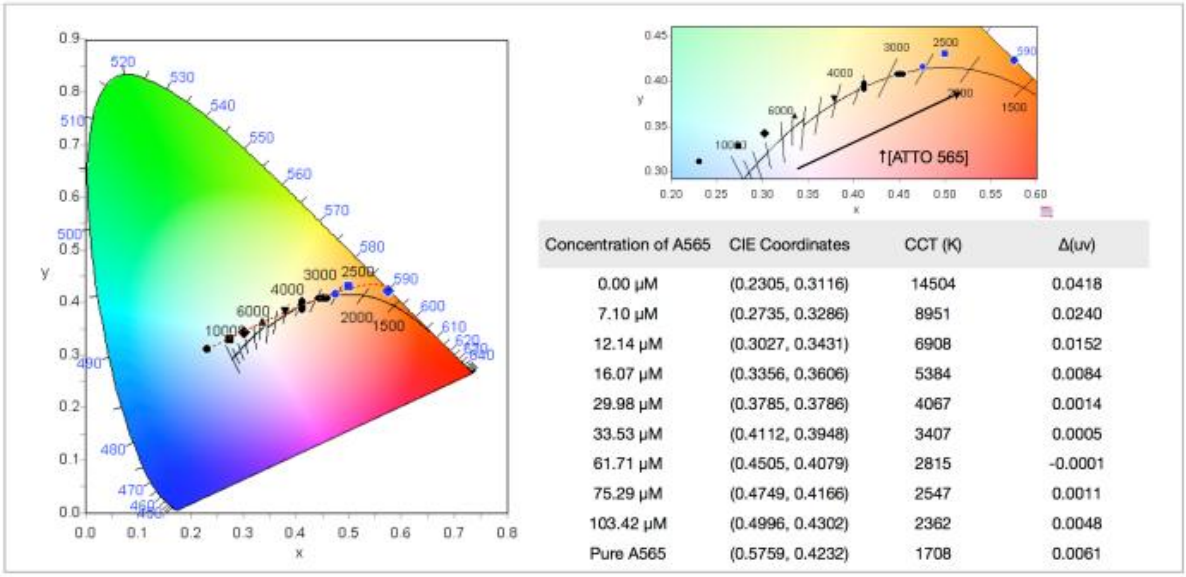

Concentration of A565	CIE Coordinates	CCT (K)	Δ(uv)
0.00 µM	(0.2305, 0.3116)	14504	0.0418
7.10 µM	(0.2735, 0.3286)	8951	0.0240
12.14 µM	(0.3027, 0.3431)	6908	0.0152
16.07 µM	(0.3356, 0.3606)	5384	0.0084
29.98 µM	(0.3785, 0.3786)	4067	0.0014
33.53 µM	(0.4112, 0.3948)	3407	0.0005
61.71 µM	(0.4505, 0.4079)	2815	-0.0001
75.29 µM	(0.4749, 0.4166)	2547	0.0011
103.42 µM	(0.4996, 0.4302)	2362	0.0048
Pure A565	(0.5759, 0.4232)	1708	0.0061

Figure 4.6. The CIE chromaticity diagram of the γ–Ga_2O_3 – A565 nanostructure with the corresponding concentration of A565 arrayed around the surface of the nanocrystals with R_c = 1.8 nm.

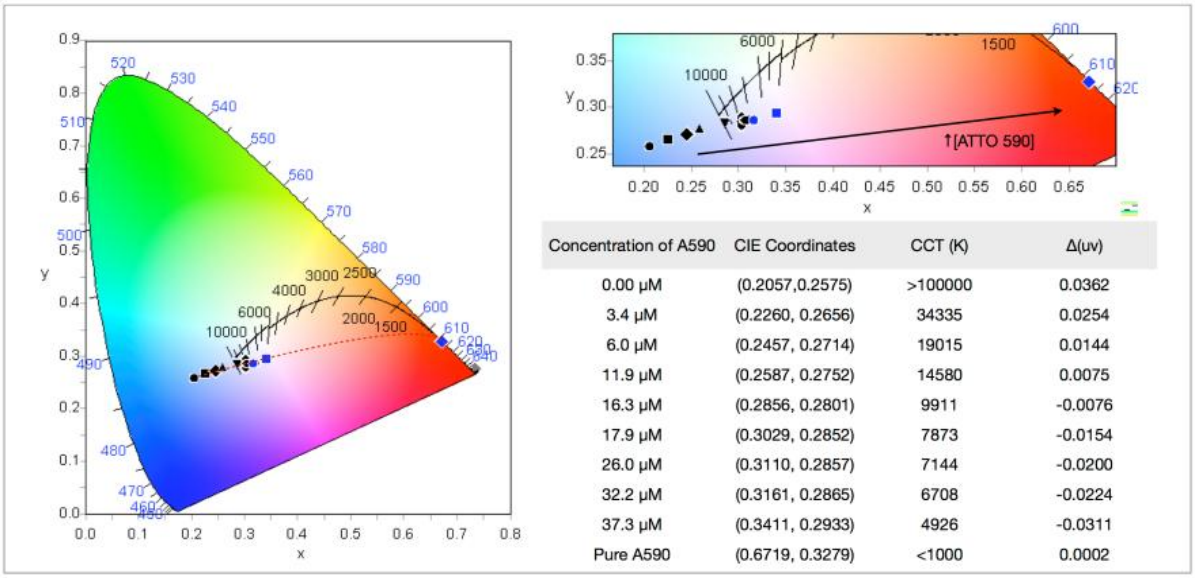

Concentration of A590	CIE Coordinates	CCT (K)	Δ(uv)
0.00 μM	(0.2057,0.2575)	>100000	0.0362
3.4 μM	(0.2260, 0.2656)	34335	0.0254
6.0 μM	(0.2457, 0.2714)	19015	0.0144
11.9 μM	(0.2587, 0.2752)	14580	0.0075
16.3 μM	(0.2856, 0.2801)	9911	-0.0076
17.9 μM	(0.3029, 0.2852)	7873	-0.0154
26.0 μM	(0.3110, 0.2857)	7144	-0.0200
32.2 μM	(0.3161, 0.2865)	6708	-0.0224
37.3 μM	(0.3411, 0.2933)	4926	-0.0311
Pure A590	(0.6719, 0.3279)	<1000	0.0002

Figure 4.7. The CIE chromaticity diagram of the γ–Ga_2O_3 with R_c = 1.8 nm – A590 nanostructure with the corresponding concentration of A565 arrayed around the surface of the nanocrystals.

4.1.2 Characterization of the White-Light-Emitting γ-Ga_2O_3 – Fluorescent Dyes Nanostructures

The assembly of RBL or A565 fluorescent dye molecules on the surface of the γ–Ga_2O_3 nanocrystals with the appropriate ratio of donor to acceptor resulted in the white-light-emitting nanomaterials (Figure 4.8(a), Figure 4.8(b) respectively). The CIE coordinates and CCT values for these white-light-emitting RBL and A565 assembled systems are (0.3328, 0.3380) at 5483 K and (0.3262, 0.3325) at 5795 K, respectively.

Due to the relatively red-shifted emission of A590 fluorescent dye molecules, the conjugation on the surface of γ–Ga_2O_3 nanocrystals resulted in a violet light emission due to the lack of the green aspect as one of the primary colours in the visible region (Figure 4.8(c) inset). The CIE coordinates and CCT value for the γ–Ga_2O_3 – A590 is (0.3161, 0.2865) at 6708 K. As a comparison, the incandescent bulbs have CCT of 2800 K, cool white fluorescent bulbs have a CCT of 6000 K, and daylight have a CCT of 4500 K. The high CCT of A590 depicted this hybrid system unsuitable as lighting source.

The chromaticity of the hybrid nanostructures can be tuned by the relative emission intensity of the blue-emitting versus orange-emitting components as the blue DAP emission of the γ–Ga_2O_3 nanocrystals quenches and increases in the sensitized emission of the secondary fluorescent dye chromophore. This

phenomenon demonstrates the behavior of Förster resonance energy transfer and dictates the tunability of the emission chromaticity of the hybrid system. The emission of these hybrid nanostructures can be adjusted by changing the electronic structure of the secondary chromophore, the size of the nanocrystals and the acceptor valency on the surface of the nanocrystals. By this approach, it is demonstrated that the quantitative pure white-light emission can be achieved based on the international chromaticity diagram. This acts as a reference point to demonstrate the manipulation of the electronic structures and the simultaneous emission as a single hybrid chomophore.

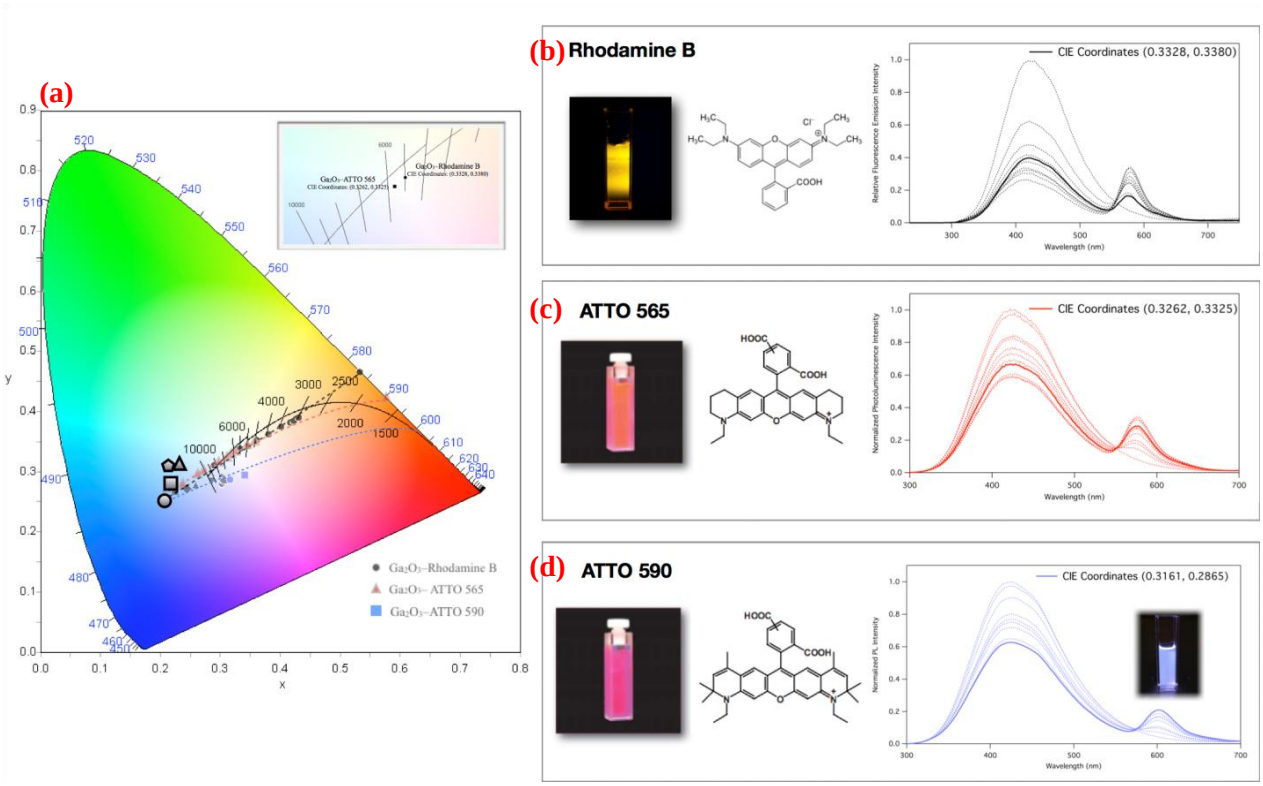

Figure 4.8. (a) The CIE chromaticity diagram for the hybrid nanostructures of γ–Ga_2O_3 nanocrystals (R_c = 1.8 nm) with RBL, A565 or A590. Steady-state PL spectra for **(b)** white-light-emitting γ–Ga_2O_3 – RBL nanostructure **(c)** white-light-emitting γ–Ga_2O_3 – A565 nanostructure; **(d)** violet-light-emitting γ–Ga_2O_3 – A590 nanostructure. The γ–Ga_2O_3 nanocrystals involved has R_c = 1.8 nm.

4.2 Single-Phased White-Light-Emitting Hybrid Nanostructures Based LEDs

The hybrid nanomaterial composed of RBL molecules arrayed around the surface of the γ–Ga_2O_3 nanocrystals acts as a single illumination entity. The nanomaterial provides a homogeneous and uniform

white-light emission, rather than a mixture or employing the layer-by-layer configuration to generate an illusion or approximation of white-light. Due to its versatility and chemical compatibility of the system, high-throughput manufacturing and processing of different devices (ranging from LEDs to luminescent liquids and polymer/plastic panels) are possible.

A prototype of the WLED have been developed by coating commercially available UV-emitting diode chip (λ_{em} = 255 nm) with the γ–Ga_2O_3 nanocrystals – RBL to efficiently convert the narrow LED emission into white-light. To increase the viscosity of the deposited solution, additional TOPO treatment was conducted on the γ–Ga_2O_3 nanocrystals prior to the conjugation of the fluorescent dyes. The concentrated suspension of the nanomaterial in hexane was deposited on the flat-window of the LED followed by air drying between the deposition steps. The electroluminescence device for the LED operated from a 9V battery with three LEDs wired in parallel. The typical spectral characteristics and performance of the commercially available LED is illustrated in Figure 4.9 (b).

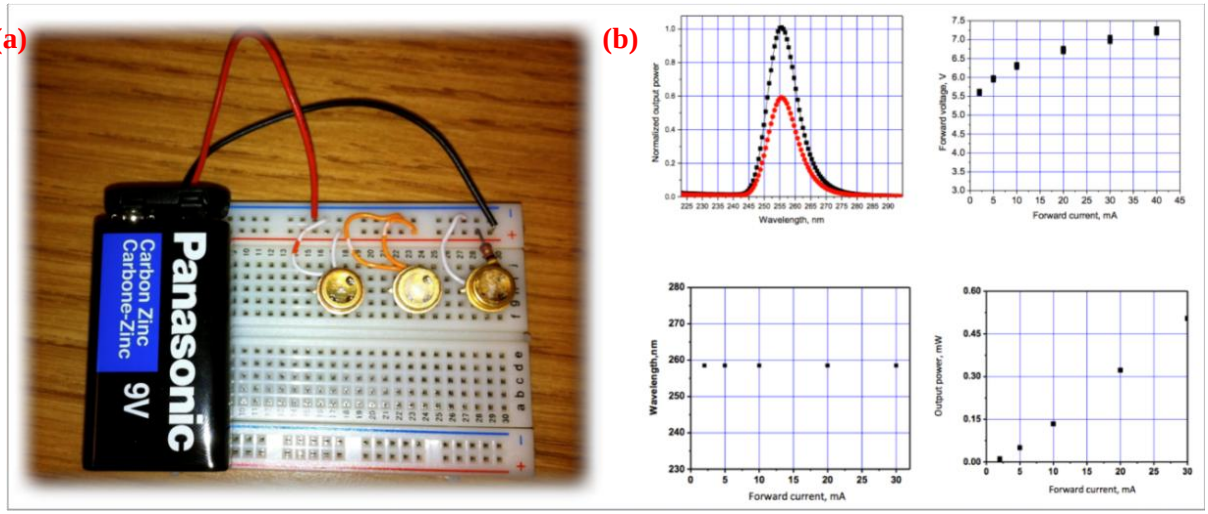

Figure 4.9. (a) Electroluminescence device with LED circuit design operate from a 9V battery; **(b)** Typical spectral characteristics and performance of the LED.

The emission of the commercially available LED is demonstrated to have an steady emission centered at 255 nm that is independent of the forward current applied, has a relatively steady current-voltage characteristics, and an increasing output power as more current is applied. This illustrates that the commercially available LED is acts solely as an excitation source, and the hybrid phosphors developed

have been shown to be an effective convertors of the UV emission from the LED excitation to the desired white-light-emission as a reference point.

The illumination of the γ–Ga_2O_3 nanocrystals, Rh-B in water and the hybrid γ–Ga_2O_3 nanocrystals-RBL nanostructures in solid and colloidal dispersion in their corresponding solvents are illustrated in Figure 4.10 (a), (b) and (c), respectively. The figures in the top right corner of each subfigure are the three emissions of the three systems dispersed in solvents, under the irradiation of UV at 254 nm. The commercially available LED coated with the corresponding deposition materials with and without irradiation is shown as the top left and bottom subfigures of Figure 4.10.

As shown in Figure 4.10, the DAP emission between the charge defect sites of the γ–Ga_2O_3 nanocrystals can be observed in both colloidal form and powder form when excited with the commercially available LED at 255 nm. On the basis of the CIE and CCT, the γ–Ga_2O_3 nanocrystals-RBL sample produces the highest quality white-light out of the three chromophore systems presented and may represent an optimal single-component phosphor for lighting applications using the 255 nm commercial UV-LED.

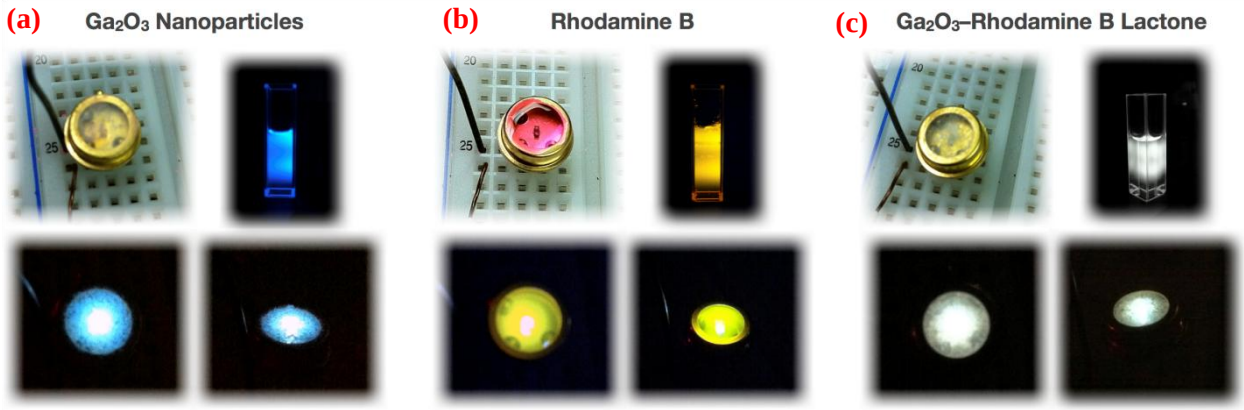

Figure 4.10. Images of phosphor in colloidal form (top right of each subfigure) and the LED phosphor assembled from the deposition of **(a)** γ–Ga_2O_3 nanocrystals; **(b)** RhB in water; **(c)** γ–Ga_2O_3 nanocrystals – RBL hybrid nanomaterials onto a 255 nm LED operating at 3.0 V (bottom of each subfigure).

4.3 Conclusion

The studies conducted throughout this thesis elaborate on the manipulation of the electronic structures of γ–Ga_2O_3 nanocrystals, the fluorescent dyes and the interactions between the two components

for the conjugated hybrid nanocomposite. A simple procedure which allows for fluorescent dyes to bind *via* carboxylic group(s) to the nanocrystals surface sites has been developed. This procedure relies on the transport of the fluorescent dyes dissolved in polar solvents to nanocrystals suspended in non-polar solvents, where the immiscibility of the two solvents forms a bilayer solution. This methodology allows for the white-light emission to be finely tuned based on the acceptor valence on the surface of the nanocrystals.

The tunability of chromaticity has been demonstrated for the hybrid nanocomposite by expanding the range of the DAP emission of the nanocrystals *via* FRET, thereby creating an efficient white-light-emitting phosphor. Quantitative analyses on the energy transfer process have been conducted using absorption, steady-state and time-resolved photoluminescence spectroscopies. Extensive analyses have been performed on the γ–Ga_2O_3 nanocrystals-RBL nanocomposites due to the dependency of the optical properties of Rh-B on its surrounding environmental factors. The interruption of the π-electron system of RBL renders this molecule non-fluorescent, suggesting the illumination beyond 550 nm is due to its interaction with the nanocrystals.

The hypothesized mechanism for the hybrid γ–Ga_2O_3 nanocrystals – fluorescent dyes nanomaterials has been rationalized based on the relative electronic energy differences. Derived from the theoretical approach, the luminance of the nanomaterials comprised of RBL is dominantly mediated by FRET, whereas the mechanism of the ATTO series hybrid systems remains unclear. The FRET-based sensitized excitation of the dyes has demonstrated lifetimes with an increase by three orders of magnitude in comparison with direct excitation of the dyes.

The broad emission spectrum of the γ–Ga_2O_3 nanocrystals has a strong overlap with the absorption spectrum of RBL, thereby allowing sufficient energy transfer efficiency (31.51% ± 0.04) and white-light conversion with CIE coordinates of (0.3328, 0.3380) at 5483 K. The versatility of the hybrid nanocomposites in lighting application had been demonstrated through the production of the prototype WLED.

4.4 Future Work

The hypothesized mechanism that governs the interactions within the hybrid nanostructures has been proposed, however, the underlying mechanism supported by experimental observations has not been obtained. The excited states of donor γ–Ga_2O_3 nanocrystals may undergo the process of charge transfer,

energy transfer (Förster or Dexter) or a combination of these competing processes, where the donor-acceptor separation distance is minimal. Transient absorption can be used to characterize the singlet and triplet excited states, excited state charge transfer, inter- and intramolecular electron transfer processes, and charge transfer complexation for understanding the underlying mechanism for these hybrid nanostructures.

By thoroughly understanding the driving force behind the formation of white-light emission in the TCO nanocrystals-organic molecules hybrid systems and its relation with the electronic structure of the individual components, the efficiency of these systems can be improved. The prevention of the excited triplet state in fluorescent dye can allow for high efficiency in white-light conversion. The optimal energy transfer scenario involves the transition from triplet state of the donor to the singlet state of the acceptor. For phosphor-sensitized fluorescence, triplet-singlet hopping transfer is disallowed. In the case where triplet relaxation on the donor is allowed, the triplet-singlet Förster transfer is permitted. The diffusion lengths for triplet excitons is considerably longer than their singlet counterparts, allowing higher energy transfer efficiency and more controllable than singlet diffusion.

WLEDs as solid-state lighting source have attracted considerable interest due to their long lifetimes, high efficiency and low power consumption; however, researchers have encountered difficulties in obtaining an optimal balance for high luminous efficacy, good stability, high CRI and ease in the processing of the devices. In addition to these aspects, the current-luminace-voltage characterizations, which include the luminous intensity (candela per m^2) and power efficiency (lumens per Watt) of the developed prototype, require further analyses and are considered important features of the LEDs in the optimization process.

In spite of the lower cost of the materials and processing technology, the mechanism of the white-light emission can be utilized for further cost reduction and efficiency optimization. The illumination of many TCO materials originates from the native defects, which allow this technology to be applicable in countless combination of materials acting as building blocks.

Zinc is the 24^{th} most abundant element on Earth and can be utilized as an ideal base for low-cost generation of hybrid nanostructures. The ZnO nanocrystals can be easily prepared by the hydrolysis method and exhibit a broad emission from *ca.* 410 to 550 nm upon near-UV irradiation (Figure 4.11) and their CIE coordinates are shown in Figure 4.12. The proposed mechanism for the origin of the PL of ZnO

nanocrystals engages the transfer of a photogenerated hole in the VB to a deep hole trap within the nanocrystal bandgap, which is suggested to be an oxygen vacancy with a single position charge (V_o*).

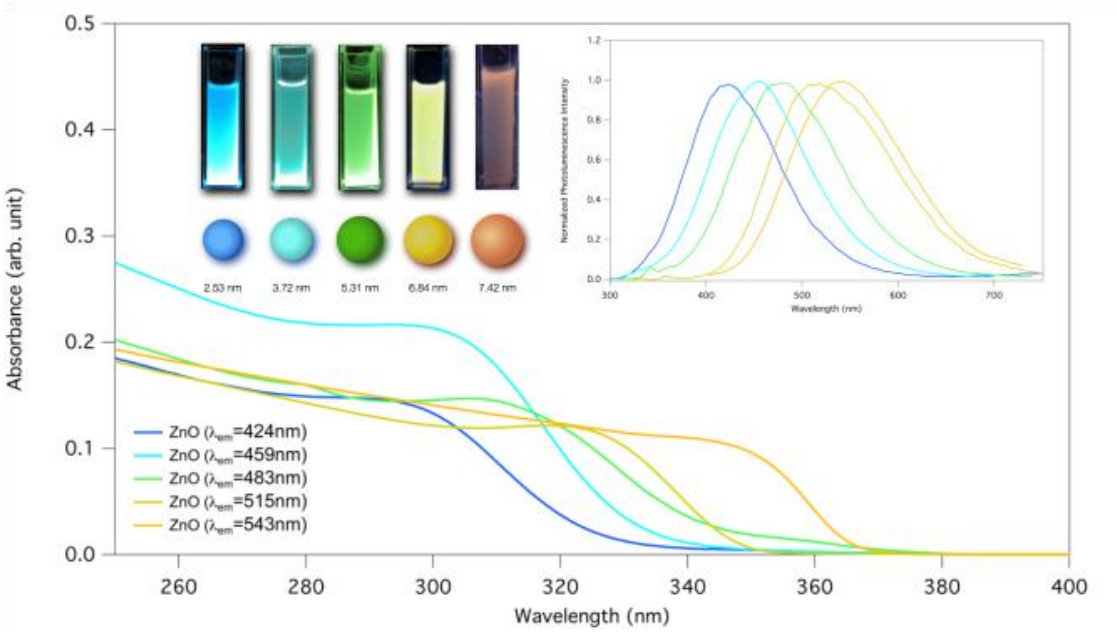

Figure 4.11. Absorption and steady-state PL emission (inset) spectra for a series of ZnO nanocrystals. The average nanocrystal sizes and images of the illumination of colloidal ZnO nanocrystals are shown in the figure.

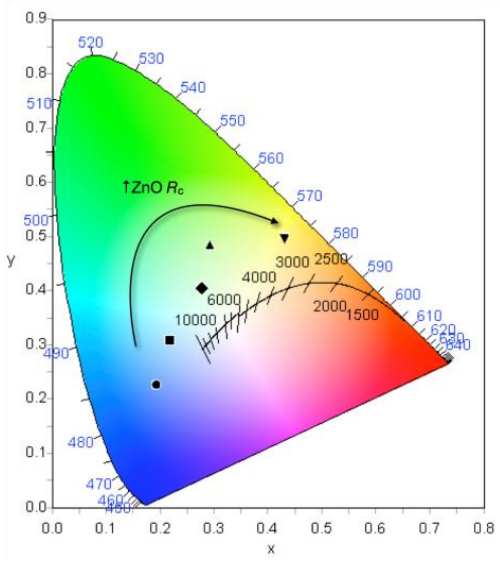

Figure 4.12. The CIE chromaticity diagram for different sizes of ZnO nanocrystals.

Typically, LEDs that have been demonstrated are based on colloidal nanocrystals by phase deposition. The advantages of the chemical compatibility and versatility of ZnO – Rh-B hybrid nanocrystals can be used to simplify the homogeneous deposition of the nanomaterials (Figure 4.13). The ability to tune the bandgap energy of ZnO nanocrystals by altering the nanocrystals size will allow for the optimization of the electronic structure and energy levels for an efficient electron/hole injection.

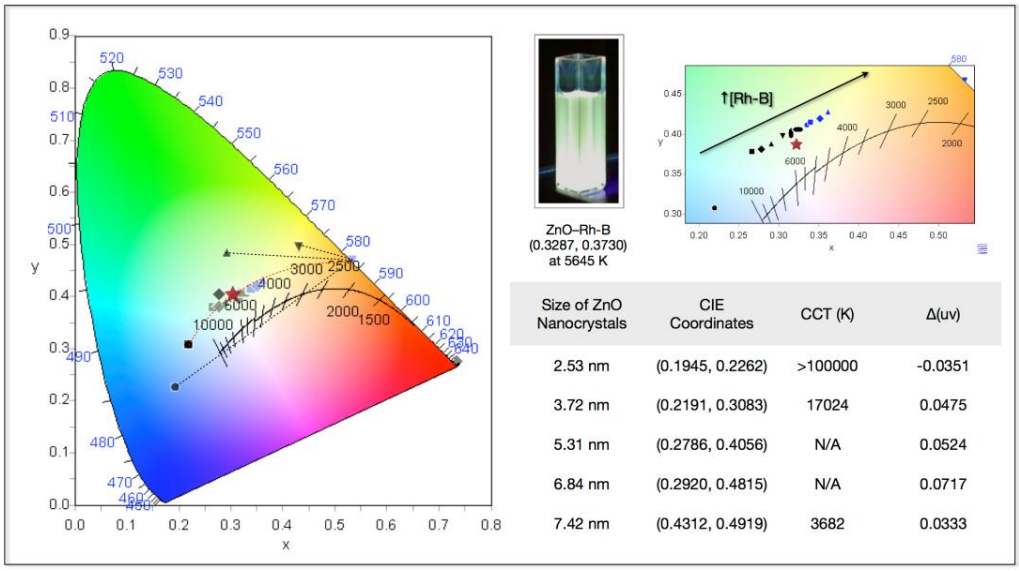

Size of ZnO Nanocrystals	CIE Coordinates	CCT (K)	Δ(uv)
2.53 nm	(0.1945, 0.2262)	>100000	-0.0351
3.72 nm	(0.2191, 0.3083)	17024	0.0475
5.31 nm	(0.2786, 0.4056)	N/A	0.0524
6.84 nm	(0.2920, 0.4815)	N/A	0.0717
7.42 nm	(0.4312, 0.4919)	3682	0.0333

Figure 4.13. The CIE chromaticity diagram of the ZnO – Rh-B nanostructure with the corresponding concentration of Rh-B arrayed around the surface of nanocrystals (R_c = 1.86 nm). The image of the illumination of ZnO – Rh-B in colloidal form with CIE coordinates of (0.3287, 0.3730) at 5645 K (shown as the red star in the CIE chromaticity diagram).

For a more practical methodology in developing *de novo* building of a WLED, a solution-processed multilayer configuration is considered as the preliminary approach. The multilayer electroluminescence architecture consists of sandwiching a thin film of multiple light-emitting materials between two electrodes, one of which must be transparent to light. Additional layers (such as electron transporting layer, hole blocking layer, hole injecting layer and hole transporting layer) assist in the charge injection and transport from the electrodes to the light-emitting film.

As the bias voltage is applied to the electrodes, the charges are injected into the multilayer system and migrate through the respective charge transporting layers, followed by the recombination in the

emitting molecules. The relaxation of the resulting excitons can lead to the formation of white-light emission.

In Figure 4.14 (a), the preliminary design for the multilayer architecture is: indium tin oxide (ITO) / poly(ethylenedioxythiophene:polystyrene sulphonate (PEDOT:PSS) / poly(*N*,*N*'-bis(4-butylphenyl)-*N*,*N*'-bis(phenyl)benzidine) (poly-TPD) / ZnO – Rh-B hybrid nanomaterial / ZnO nanocrystals / Al. The multilayer design can be achieved by spin coating the nanocrystals followed by annealing.

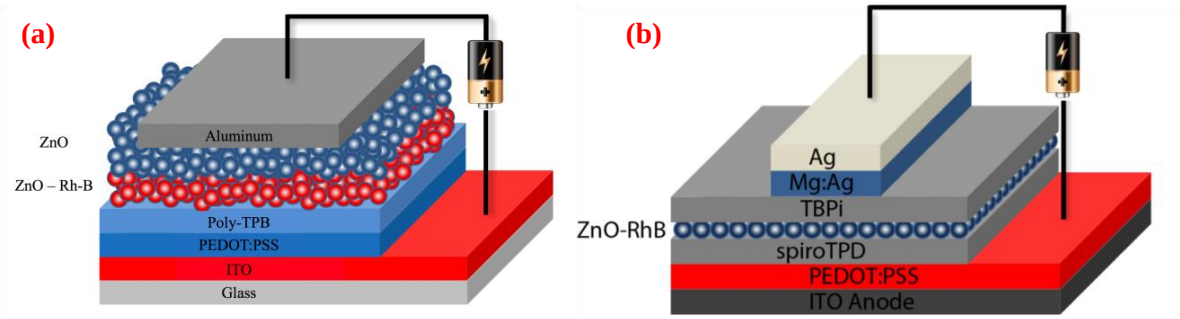

Figure 4.14. Schematic illustration of electroluminescence configuration based on ZnO – Rh-B hybrid nanomaterial. **(a)** Layer-by-layer configuration of ZnO – Rh-B based WLED; **(b)** single-phase design of ZnO – Rh-B based WLED.

An alternative configuration is illustrated in Figure 4.14 (b), where the emitting material consist of a single-phase phosphor: ITO / PEDOT:PSS / *N*,*N*'-bis(3-methylphenyl)-*N*,*N*'-diphenyl-9,9-spirobifluorene-2,7-diamine (spiro-TPD) / ZnO – Rh-B hybrid nanomaterial / 1,3,5-tris(*N*-phenylbenzimidizol-2-yl)benzene (TBPi) / Mg:Ag / Ag. The optimization of the electroluminescence devices include the tuning of the thickness of individual layers, annealing temperature and duration and the electronic structures of the electron transport layer and the hole transport layer.

The electronic structures of the materials utilized in the design of *de novo* building of a WLED play a critical role in the emission properties of the hybrid nanomaterials. The white-light-emitting phosphors are promising for use as a new type of phosphors in WLED.

Appendix

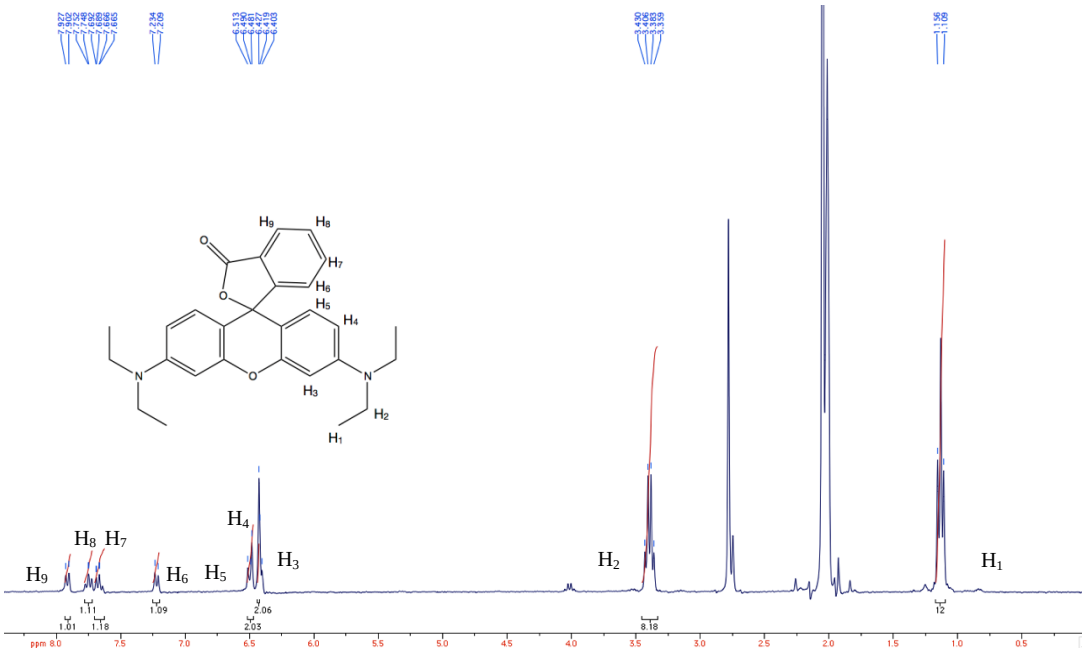

Figure A.1. ^{1}H NMR spectrum of RBL in $(CD_3)_2CO$.

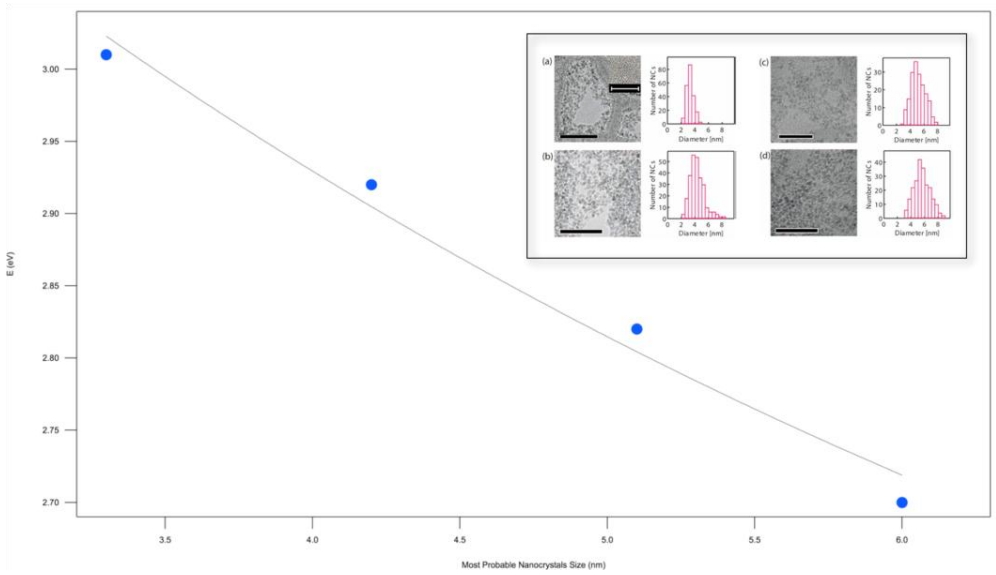

Figure A.2. The dependence of the energy of the PL band maximum (DAP emission energy) on the nanocrystals size and was fitted with a double exponential function. Inset: TEM images of γ-Ga_2O_3 nanocrystals and size distribution determined from TEM images of ca. 200 nanocrystals for different sizes: **(a)** R_c = 1.65 nm; **(b)** R_c = 2.1 nm; **(c)** R_c = 2.55 nm; **(d)** R_c = 2.75 nm. Scale bars in TEM images are 50 nm.

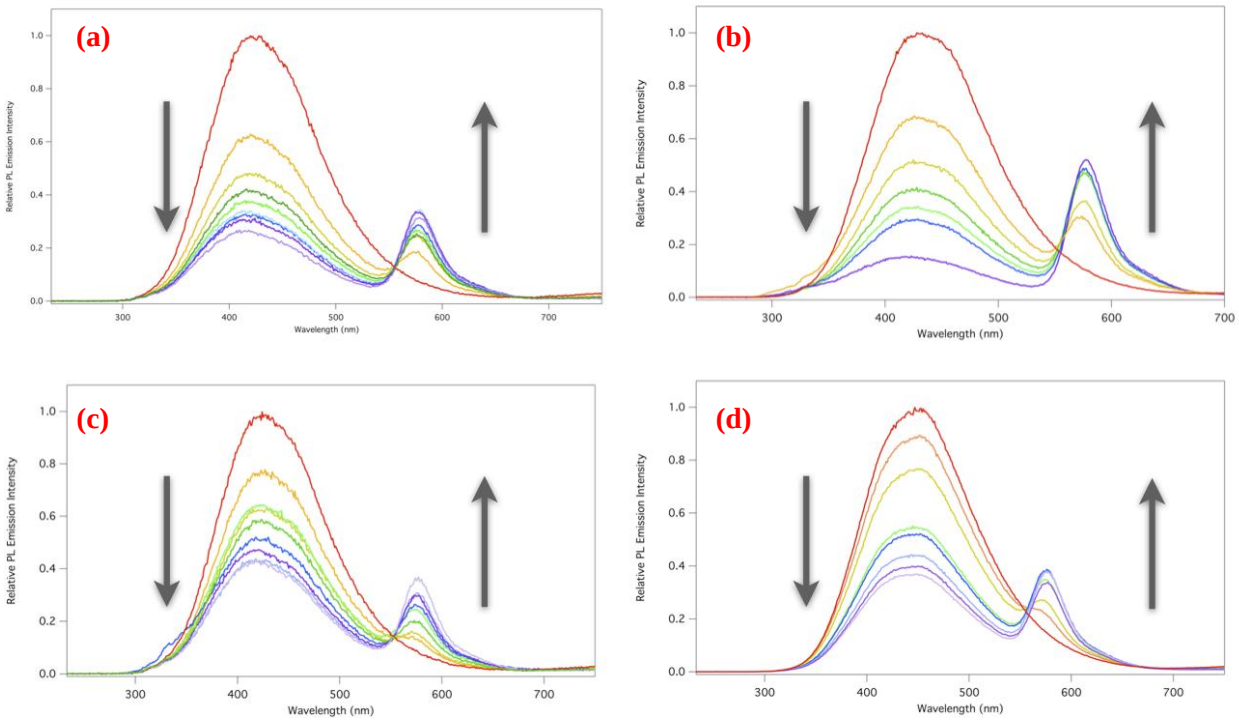

Figure A.3. Steady-state PL spectra for various concentration of RBL with different sizes of γ-Ga_2O_3: **(a)** R_c = 1.8 nm; **(b)** R_c = 2.05 nm; **(c)** R_c = 2.5 nm; **(d)** R_c = 2.65 nm. The arrows demonstrate the response of the PL intensities of the two components as the concentration of RBL increase.

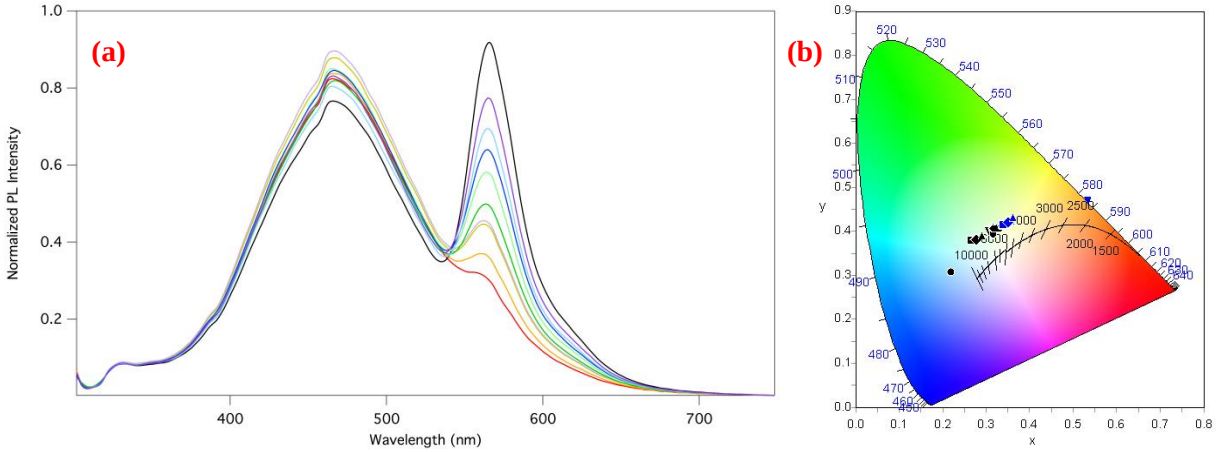

Figure A.4. (a) Steady-state PL spectra for various concentration of Rh-B with ZnO nanocrystals (R_c = 1.86 nm). **(b)** The CIE chromaticity diagram for the hybrid nanostructures of ZnO nanocrystals (R_c = 1.86 nm) with Rh-B.

Bibliography

(1) Hawken, P., A. Lovins and L. H. Lovins. *Natural Capitalism: Creating the Next Industrial Evolution.* 1st ed.; Little, Brown & Co.:Boston, London, 1999.

(2) U.S. Lighting Market Characterization, vol. 1, *National Lighting Inventory and Energy Consumption Estimates*. Washington, D.C.: U.S. Department of Energy, 2002, Naigant Consulting , Inc.

(3) Solid-state Lighting Research and Development Portfolio: Multi-year program plan FY'07-FY'12, Navigant Consulting, Inc., 2006, prepared for Lighting Research and Development Building Technologies Program, Office of Energy Efficiency and Renewable Energy, U.S. Dept. of Energy.

(4) Solid-state Lighting Research and Development Portfolio: Multi-year program plan FY'07-FY'12, Navigant Consulting, Inc., 2008, prepared for Lighting Research and Development Building Technologies Program, Office of Energy Efficiency and Renewable Energy, U.S. Dept. of Energy.

(5) Khan, N.; Abas, N. *Renewable and Sustainable Energy Reviews* **2011**, *15*, 296.

(6) Schubert, E. F. *Light-Emitting Diodes*. Cambridge University Press: Cambridge, UK, 2006.

(7) Energy Information Administration, *Historical Electricity Retail Sales Tables*, U.S. Department of Energy.

(8) Steigerwald, D. A.; Bhat, J. C.; Collins, D.; Fletcher, R. M.; Holcomb, M. O.; Ludowise, M. J.; Martin, P. S.; Rudaz, S. L. *IEEE J. Select. Topics. Quant. Electr.* **2002**, *8*, 310.

(9) Humphreys, C. J. *MRS Bulletin*. **2008**, *33*, 459.

(10) Gardner, N. F.; Müller, G. O.; Shen, Y. C.; Chen, G.; Watanabe, S.; Götz, W.; Krames, M. R. *Appl. Phys. Lett.* **2007**, *91*, 234506.

(11) Monemar, B.; Sernelius, B. E. *Appl. Phys. Lett.* **2007**, *91*, 181103.

(12) Xie, J.; Ni, X.; Fan, Q.; Shimada, R.; Ü. Özgür; H. Morkoç. *Appl. Phys. Lett.* **2008**, *93*, 121107.

(13) Yang, Y. *IEEE Transactions on Electron Devices*. **2008**, *55*, 1771.

(14) Kim, M. H.; Schubert, M. F.; Dai, Q.; Kim, J. K.; Schubert, E. F.; Piprek, J.; Park, Y. *Appl. Phys. Lett.* **2007**, *91*, 183507.

(15) Shur, M. S.; Zukauskas, A. *Proc. IEEE*. **2005**, *93*, 1691.

(16) Lee, I. S. *White-light-emitting Diode.* U.S. Patent 7,759,683, July 20, 2010.

(17) Srivastava, A. M.; Comanzo, H. A. *White-light-emitting Phosphor Blend for LED Devices*. U.S. Patent 6,501,100, December 31, 2002.

(18) Tanabe, S.; Fujita, S.; Yoshihara, S.; Sakamoto, A.; Yamamoto, S. *Proc. of SPIE*. **2005**, *5941*, 594112.

(19) Srivastava, A. M.; Duggal, A. R.; Comanzo, H. A.; Beers, W. W. *Single Phosphor for Creating White-light with High Luminosity and High CRI in a UV LED Device.* U.S. Patent 6,522,065, February 18, 2003.

(20) D'Andrade, B. W.; Holmes, R. J.; Forrest, S. R. *Adv. Mater.* **2004**, *16*, 624.

(21) Lee, M. T.; Tseng, M. R. *White-light Organic Electroluminescent Element*. U.S. Patent 7,772,762, August 10, 2010.

(22) Bachmann, V.; Ronda, C.; Meijerink, A. *Chem. Mater.* **2009**, *21*, 2077.

(23) Pan, Y. X.; Wu, M. M.; Su, Q. *J. Phys. Chem. Solids.* **2004**, *65*, 845.

(24) Wang, W. D.; Tang, J. K.; Sheng, T. H.; Wang, J.; Sullivan, B. P. *Chem. Phys. Lett.* **2008**, *457*, 103.

(25) Commission Internationale de l'Éclairage, *Commission Internationale de l'Éclairage proceedings*, Cambridge Univ. Press, Cambridge, U.K., 1978.

(26) Zhang, Q. Y.; Pita, K.; Ye, W.; Que, W. X. *Chem. Phys. Lett.* **2002**, *163*, 351.

(27) Schanda, J. *Colourimetry: Understanding the CIE System.* John Wiley & Sons: Hoboken, NJ, 2007.

(28) Von Kries, J.; Die Gesichtsempfindungen, in: Nagel's *Handbuch d. Physiol. d. Menschen* **3. Band** Teil VI. Positive and negative Nachbilder. Lokale und Farbumstim-mungen des Sehorgans, pp. 205-220.

(29) Yu, X. M.; Kwok, H. S.; Wong, W. Y.; Zhou, G. J. *Chem. Mater.* **2006**, *18*, 5097.

(30) Alam, M. M.; Jenekhe, S. A. *Macromol. Rapid Commun.* **2006**, *27*, 2053.

(31) Tu, G.; Mei, C.; Zhou, Q.; Cheng, Y.; Geng, Y.; Wang, L.; Ma, D.; Jing, X.; Wang, F. *Adv. Funct. Mater.*, **2006**, *16*, 101.

(32) Brus, L. E. *J. Chem. Phys.* **1983**, *79*, 5566.

(33) Alivisatos, A. P. *Science*. **1996**, *271*, 933.

(34) Murray, C. B.; Norris, D. J.; Bawendi, M. G. *J. Am. Chem. Soc.* **1993**, *115*, 8706.

(35) Ruckenstein, E.; Li, Z. F. *Adv. Colloid Interface Sci.* **2005**, *113*, 43.

(36) Kickelbick, G.; Schubert, U. *Organic Functionalization of Metal Oxide Nanoparticles*. Baraton, MI. **2003**.

(37) Doty, R. C.; Tshikhudo, T. R.; Brust, M.; Fernig, D. G. *Chem. Mater.* **2005**, *17*, 4630.

(38) Moon, J. H.; Shul, Y. G.; Hong, S. Y.; Choi, Y. S.; Kim, H. T. *Inter. J. Adhes. Adhes.* **2005**, *25*, 534.

(39) Schulz-Dobrick, M.; Sarathy, K. V.; Jansen, M. *J. Am. Chem. Soc.* **2005**, *127*, 12816.

(40) Zayats, M.; Katz, E.; Baron, R.; Willner, I. *J. Am. Chem. Soc.* **2005**, *127*, 12400.

(41) Kisailus, D.; Najarian, M.; Weaver, J. C.; Morse, D. E.; *Adv. Mater.* **2005**, *17*, 1234.

(42) Price, R. C.; Whetten, R. L. *J. Am. Chem. Soc.* **2005**, *127*, 13750.

(43) Fan, H.; Chen, Z.; Brinker, C. J.; Clawson, J.; Alam, T. *J. Am. Chem. Soc.* **2005**, *127*, 13746.

(44) Brust, M.; Fink, J.; Bethell, D.; Schiffrin, D. J.; Kiely, C. *Chem. Commun.* **1995**, *18*, 1655.

(45) Jiang, H.; Moon, K. S.; Li, Y.; Wong, C. P. *Chem. Mater.* **2006**, *18*, 2969.

(46) Kolliopoulou, S.; Dimitrakis, P.; Normand, P.; Zhang, H. L.; Cant, N.; Evans, S. D.; Paul, S.; Pearson, C.; Molloy, A.; Petty, M. C.; Tsoukalas, D. *J. Appl. Phys.* **2003**, *94*, 5234.

(47) Lee, M. S.; Hong, S. S.; Mohseni, M. *J. Mol. Catal. A. Chem.* **2005**, *242*, 135.

(48) Sen, S.; Mahanty, S.; Roy, S.; Heintz, O.; Bourgeois, S.; Chaumont, D. *Thin Solid Films.* **2005**, *474*, 245.

(49) Woehrle, G. H.; Hutchison, J. E. *Inorg. Chem.* **2005**, *44*, 6149.

(50) Xiong, Y.; Wiley, B. J.; Xia, Y. *Angew. Chem., Int. Ed.* **2007**, *46*, 7157.

(51) Zhang, H.; Banfield, J. F. *J. Mater. Chem.* **1998**, *8*, 2073.

(52) Zhang, H.; Banfield, J. F. *J. Phys. Chem. B.* **2000**, *104*, 3481.

(53) Gurlo, A.; Kroll, P.; Riedel, R. *Chem. Eur. J.* **2008**, *14*, 3306.

(54) Wang, T.; Farvid, S. S.; Abulikemu, M.; Radovanovic, P. V. *J. Am. Chem. Soc.* **2010**, *132*, 9250.

(55) Wang, T.; Radovanovic, P. V. *J. Phys. Chem. C.* **2011**, *115*, 18473.

(56) Wang, T.; Radovanovic, P. V. *J. Phys. Chem. C.* **2011**, *115*, 406.

(57) Tippins, H. H. *Phys. Rev.*, **1965**, *140*, A316.

(58) Vasil'tsiv, V. I.; Zakharko, Ya. M. *Sov. Phys. Solid Sate*, **1983**, *25*, 72.

(59) Kuznetsov, A. I.; Abramov, V. N.; Uibo, T. V. *Opt. Spectrosc. (USSR)*, **1985**, *58*, 368.

(60) Vasil'tsiv, V. I.; Zakharzo, Ya. M.; Prim, Ya. I., *Ukr. Fiz. Zh.*, **1988**, *33*, 1320.

(61) Thomas, D. G.; Hopfield, J. J.; Augustyniak, W. M. *Phys. Rev.* **1965**, *140*, A202.

(62) Förster, T. *Delocalized Excitation and Excitation Transfer.* In: *Modern Quantum Chemistry; Part III; Action of Light and Organic Molecules.* (Sunanoglu, O., ed.). Vol. 3. Academic, New York, 1965.

(63) Nguyen, T.; Francis, M. B. *Org. Lett.* **2003**, *5*, 3245.

(64) Hegde, M.; Wang, T.; Miskovic, Z. L.; Radovanovic, P. V. *Appl. Phys. Lett.* **2012**, *100*, 141903.

(65) Gill, J. E. *Photochem. Photobiol.* **1969**, *9*, 313.

(66) Clegg, R. M. *Methods. Enzymol.* **1992**, *211*, 353.

(67) Van Der Meer, W. B.; Coker, G., III; Chen, S.-Y. *Resonance Energy Transfer: Theory and Data*. Wiley, New York, 1994.

(68) Majumdar, Z.; Hickerson, R.; Noller, H.; Clegg, R. *J. Mol. Biol.* **2005**, *351*, 1123.

(69) Atkins, P. W.; Friedman, R. S. *Molecular Quantum Mechanics*. Oxfort University Press, Oxford, 1997.

(70) Frisch, M. J. *et al. Gaussian 09*, Revision A.02; Gaussian Inc.: Wallingford, CT, 2009.

(71) Becke A. D. *Phys. Rev. A.* **1988**, *38*, 3098.

(72) Lee, C.; Yang, W.; Parr, R. G. *Phys. Rev. B.* **1988**, *37*, 785.

(73) Miehlich, B.; Savin, A.; Stoll, H.; Preuss, H. *Chem. Phys. Lett.* **1989**, *157*, 200.

(74) Rassolov, V. A.; Pople, J. A.; Ratner, M. A.; Windus, T. L. *J. Chem. Phys.* **1998**, *109*, 1223.

(75) Rassolov, V. A.; Ratner, M. A.; Pople J. A.; Redfern, J. A.; Curtiss, L. A. *J. Comput. Chem.* **2001**, *22*, 976.

(76) Tomasi, J.; Mennucci, B.; Cammi, R. *Chem. Rev.* **2005**, *105*, 2999.

(77) Seeger, R.; Pople, J. A. *J. Chem. Phys.* **1977**, *66*, 3045.

(78) Bauernschmitt, R.; Ahlrichs, R. *J. Chem. Phys.* **1996**, *104*, 9047.

(79) Stratmann, R. E.; Scuseria, G. E.; Frisch, M. J. *J. Chem. Phys.* **1998**, *109*, 8218.

(80) O' Boyle, N. M.; Tenderholt, A. L.; Langner, K. M. *J. Comput. Chem.* **2008**, *29*, 839.

(81) Dennington, R.; Keith, T.; Millam, J. *GaussView*, Version 5; Semichem, Inc.: Shawnee Mission, KS, 2009.

(82) Blöchl, P. E. *Phys. Rev. B.* **1994**, *50*, 17953.

(83) Kresse, G.; Furthmüller, J. *Phys. Rev. B.* **1996**, *54*, 11169.

(84) Torneiro, M.; Still, W. C. *J. Am. Chem. Soc.* **1995**, *117*, 5887.

(85) Schoonen, M. A. A.; Xu, Yong. *Am. Min.* **2000**, *85*, 543.